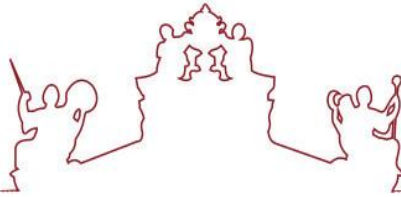




SAPIENZA  
UNIVERSITÀ DI ROMA



ARISTOTLE  
UNIVERSITY OF  
THESSALONIKI



**Universidade de Évora - Instituto de Investigação e Formação Avançada  
Università degli Studi di Roma "La Sapienza" Aristotle University of  
Thessaloniki**

Mestrado em Ciência dos Materiais Arqueológicos (ARCHMAT)

Dissertação

**Characterization of Historic Mortars from the City of Lisbon  
(Portugal)**

Amira Souliman Towfik Mohamed

Orientador(es) | Cristina Galacho  
Patrícia Sofia Moita

Évora 2022

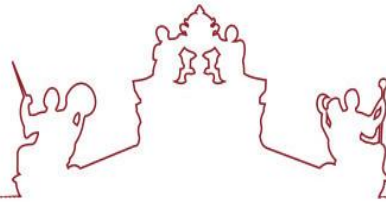




SAPIENZA  
UNIVERSITÀ DI ROMA



ARISTOTLE  
UNIVERSITY OF  
THESSALONIKI



---

**Universidade de Évora - Instituto de Investigação e Formação Avançada  
Università degli Studi di Roma "La Sapienza" Aristotle University of  
Thessaloniki**

Mestrado em Ciência dos Materiais Arqueológicos (ARCHMAT)

Dissertação

**Characterization of Historic Mortars from the City of Lisbon  
(Portugal)**

Amira Souliman Towfik Mohamed

Orientador(es) | Cristina Galacho

Patrícia Sofia Moita

Évora 2022

---

---

---

---

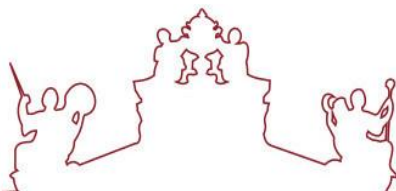
---



SAPIENZA  
UNIVERSITÀ DI ROMA



ARISTOTLE  
UNIVERSITY OF  
THESSALONIKI



A dissertação foi objeto de apreciação e discussão pública pelo seguinte júri nomeado pelo Diretor do Instituto de Investigação e Formação Avançada:

Presidente | Nicola Schiavon (Universidade de Évora)

Vogais | Carlos Alexandre Ribeiro (Universidade de Évora) (Arguente)  
Donatella Magri (Università degli Studi di Roma "La Sapienza")  
Eleni Pavlidou (Aristotle University of Thessaloniki)  
Panagiotis Spathis (Aristotle University of Thessaloniki)  
Patrícia Sofia Moita (Universidade de Évora)  
Cristina Galacho (Universidade de Évora)

Évora 2022



# TABLE OF CONTENTS

---

ACKNOWLEDGMENTS .....	vii
ABSTRACT.....	viii
RESUMO .....	ix
LIST OF TABLES .....	x
LIST OF FIGURES .....	xi
LIST OF APPENDICES .....	xv
<b>1 INTRODUCTION.....</b>	<b>1</b>
1.1 AIMS OF STUDY.....	1
1.2 MORTARS.....	2
1.2.1 Lime mortar .....	3
1.2.2 Aerial lime mortar.....	5
1.2.3 Hydraulic lime mortar.....	5
<b>2 ARCHAEOLOGICAL CONTEXTS .....</b>	<b>6</b>
2.1 HISTORICAL BACKGROUND .....	6
2.1.1 Function of the Cryptoporticus .....	8
2.1.2 Excavation.....	9
2.1.3 Architectural description.....	11
2.2 GEOLOGICAL CONTEXT.....	12
<b>3 SAMPLES AND METHODOLOGY .....</b>	<b>14</b>
3.1 SAMPLES .....	14
3.2 SAMPLE PREPARATION.....	16
3.2.1 Sectioned Samples - Preparation for Optical/Stereo Microscopy.....	17
3.2.2 Powdered Samples - Preparation for XRD and TGA Analysis .....	18
3.2.3 Fragmented samples - Preparation for Acid attack and Granulometric Analysis.	

3.3	ANALYTICAL TECHNIQUES AND METHODS .....	20
3.3.1	Visual inspection.....	21
3.3.2	Optical Microscopy (OM).....	21
3.3.3	Thermogravimetric Analysis (TGA-DTG).....	21
3.3.4	X-Ray Diffraction (XRD) .....	22
3.3.5	Variable pressure scanning electron microscopy coupled with Energy Dispersive X-Ray Spectroscopy VP-SEM-EDS.....	22
3.3.6	Acid attack and Granulometric analysis .....	23
3.4	ANALYSES EQUIPMENTS AND EXPERIMENTAL CONDITIONS .....	23
3.4.1	Stereo microscopy.....	23
3.4.2	Petrographic microscopy .....	24
3.4.3	Thermogravimetric analysis.....	24
3.4.4	X-ray diffraction .....	25
3.4.5	Variable pressure Scanning Electron Microscopy coupled with Energy Dispersive X-ray Spectroscopy.....	25
3.4.6	Acid attack and Granulometric analysis .....	26
4	RESULTS .....	28
4.1	VISUAL INSPECTION .....	28
4.2	OPTICAL MICROSCOPY (OM) .....	30
4.2.1	Stereo microscopy.....	30
4.2.2	Petrography .....	37
4.3	THERMOGRAVIMETRIC ANALYSIS (TGA-DTG) .....	39
4.4	X-RAY DIFFRACTION (XRD).....	46
4.5	VARIABLE PRESSURE SCANNING ELECTRON MICROSCOPY COUPLED WITH ENERGY DISPERSIVE X-RAY SPECTROSCOPY (VP-SEM-EDS) .....	51
4.6	ACID ATTACK AND GRANULOMETRIC ANALYSIS .....	60
5	DISCUSSION .....	69
5.1	RAW MATERIALS .....	69
5.1.1	Binder.....	69
5.1.2	Aggregates .....	71

5.2	PROVENANCE .....	72
5.3	PRODUCTION TECHNOLOGY .....	74
6	CONCLUSION .....	79
	BIBLIOGRAPHY .....	82
	APPENDICES .....	87

## ACKNOWLEDGMENTS

---

بِسْمِ اللَّهِ الرَّحْمَنِ الرَّحِيمِ

وَقُلْ أَعْمَلُوا فَسَيَرَى اللَّهُ عَمَلَكُمْ وَرَسُولُهُ وَالْمُؤْمِنُونَ وَسَتُرَدُّونَ إِلَىٰ عِلْمِ الْغَيْبِ وَالشَّهَادَةِ فَيُنبِّئُكُم بِمَا كُنتُمْ تَعْمَلُونَ

This Master's thesis would not have been realized without the encouragement and unwavering support of people who deserve special thanks for their contribution to this academic work.

I would like to deeply express my sincere gratitude to my supervisors Professor Patrícia Moita and Professor. Cristina Galacho, for the continuous support of my MSc study. Without their trust and precious support, this work would not have been possible. I appreciate their inspiration, valuable guidance and feedback which allowed me to gain a better understanding in the field of archaeometric research.

I would like to thank to the Municipality of Lisbon (Câmara Municipal de Lisboa, CML), in particular to the Archaeologist António Marques, Coordinator of Lisbon Archeology Center (Centro de Arqueologia de Lisboa, CAL), the Archaeologist Cristina Nozes and the Geologist Eva Leitão for giving me access to the archaeological structure and providing the samples, as well as all the information necessary for the contextualization of the sites, without their help and their availability this work would not have been possible.

I would also like to thank Doctor Nick Schiavon and the ARCHMAT EMMC Committee, for giving me the opportunity for participation in this program including all Professors that provided valuable knowledge to develop the necessary skills in the field of heritage science. I am grateful to all the academic staff, researchers, and students of the HERCULES Laboratory. In particular Anna Tsoupra for her technical support and recommendations during my research. I would like to express my special thanks to Ms. Sandra Velez and Ms. Aida Graça for their assistance and expertise during the laboratory works. I would like to thank my professors back to Egypt, in particular Professor Mahmoud Abd El Hafez and Professor Mohsen Saleh.

My forever thanks to my family who was always and generously by my side, to my mother and father, who are credited with everything I have achieved in my life, which is because of them and for them. Thank you for your prayers, trust, constant encouragement and motivation. If not for you, I would not be here. Without you, I would not be me.

Finally, I want to with love and gratitude to thank all my friends back to Egypt for being with me all the time during my journey, my ARCHMAT colleagues who become my second family.

## ABSTRACT

---

Characterization of Historic Mortars from the Roman Cryptoporticus of Lisbon (Portugal)

The Roman Cryptoporticus of Lisbon, also known as the “Roman Galleries of Rua da Prata” (Lisbon, Portugal), dates from the 1<sup>st</sup> century AD. The roman galleries form a chain of vaulted subterranean galleries, with different heights and spans, parallel and perpendicular to each other. The original function of the Cryptoporticus has met multiple interpretations over time. One of the hypotheses that unanimously agreed is that it might have been an architectural solution to support a construction of large buildings (usually public) in an area with a slope and little geological stability.

The main objective of the work is to bring a clear understanding of the roman mortars composition to obtain information about the production technology and the raw materials used and their possible origin. Such characterization is necessary to create compatible repair mortars as part of a sustainable conservation methodology for the future conservation plan.

A total of 24 mortar samples have been collected from different places of the Cryptoporticus with different functions and ages was characterized by a multi-analytical archaeometric approach by means of Optical Microscopy (Stereo zoom and Petrographic microscope), Thermogravimetric analysis (TGA-DTG), X-Ray Diffraction (XRD), Scanning Electron Microscopy – Energy Dispersive X-ray Spectroscopy (SEM-EDS), Acid attack and Granulometric analysis.

The samples were divided into six groups, according to the most abundant type of aggregates and representative characteristics. These groups agree with different spaces/structures, age and functions for the use of mortars (filling, repair, rendering, binding and water storage). The binder is mainly calcitic aerial lime. The presence of dolostone lithics suggests its use only as aggregate and not to produce lime as commonly happened on Roman edifications.

### **Key Words:**

Roman Cryptoporticus, mortars characterization, raw materials, provenance, archaeometry.

## RESUMO

---

### Caracterização de Argamassas Históricas do Criptopórtico Romano de Lisboa (Portugal)

O Criptopórtico Romano de Lisboa, também conhecido como “Galerias Romanas da Rua da Prata” (Lisboa, Portugal), data do século I d.C. As Galerias Romanas formam uma cadeia de galerias subterrâneas abobadadas, com diferentes alturas e vãos, paralelas e perpendiculares entre si. A função original do criptopórtico conheceu, ao longo do tempo, múltiplas interpretações. A hipótese mais unânime é a que poderia ter sido uma solução arquitetónica que visou criar, em zona de declive e pouca estabilidade geológica, uma plataforma horizontal de suporte à construção de edifícios de grande dimensão, geralmente públicos.

O principal objetivo do trabalho apresentado foi a caracterização de argamassas romanas do Criptopórtico de Lisboa, do ponto de vista textural, mineralógico e químico, visando a obtenção de informações sobre a sua composição, a tecnologia de produção, as matérias-primas utilizadas e sua proveniência. Esta caracterização é necessária para a produção de argamassas de restauro compatíveis como parte de uma metodologia de conservação sustentável para um futuro plano de conservação.

Um total de 24 amostras de argamassas, com diferentes funções e idades, foram recolhidas em diferentes locais do Criptopórtico e caracterizadas por uma abordagem arqueométrica multianalítica: Microscopia Ótica (Estereomicroscopia e Petrografia), Análise Termogravimétrica (ATG-DTG), Difração de Raios-X (DRX), Microscopia Eletrónica de Varrimento – Espectroscopia de Energia Dispersiva de Raios-X (MEV-EDS), Ataque Ácido e Análise Granulométrica.

As amostras foram divididas em seis grupos, de acordo com o tipo de agregados mais abundante ou outras características representativas. Estes grupos concordam com os diferentes espaços/estruturas, idades e função das argamassas (enchimento, reboco e reparação). Os resultados indiciam a presença de um ligante aéreo de composição calcítica. A presença de líticos dolomíticos sugere o seu uso apenas como agregado e não como ligante, de acordo com o que era comum em edificações romanas.

**Palavras-chave:** Criptopórtico romano, caracterização de argamassas, matérias-primas, proveniência, arqueometria.

## LIST OF TABLES

---

Table 3.1 General description of the samples.....	15
Table 4.1 Samples grouping based on the preliminary visual inspection.....	28
Table 4.2 Photographic documentation of representative samples before disaggregation.....	29
Table 4.3 Particularities of representative samples observed under stereo microscope.....	31
Table 4.4 Identification and description of the samples by microscopic observations (stereo zoom microscope) of cross sections. ....	32
Table 4.5 Results obtained from the microscopic observations of the cross sections of the samples.....	35
Table 4.6 Types of ceramics fragments found in samples.....	36
Table 4.7 Visual estimated distribution of ceramic fragment types found in samples.....	36
Table 4.8 Petrographic features representative of defined groups. XPL (cross polarized light) and PPL (plane- polarized light).....	38
Table 4.9 Sample mass losses, calcium carbonate contents (%) and binder to aggregate ratio obtained by TGA.....	45
Table 4.10 The mineralogical composition and predominance of the mortars (XRD analysis).....	50
Table 4.11 Results from GRADISTAT based on Udden (1914) and Wentworth's (1922) classifications.....	65
Table 5.1 Subdivision of samples by groups used for discussing the manufacturing techniques.....	75
Table 5.2 Simplified compositions of the mortars (%) using Jedrzejewska method (Jedrzejewska, 1960).....	75

## LIST OF FIGURES

---

Figure 1.1 The lime cycle. A) calcination, B) hydration and C) carbonation.-----	3
Figure 2.1 Location of the Roman Cryptoporticus in Lisbon, Portugal. A) Rua da Prata B) Rua da Conceição C) Rua da São Julião. Base images taken from Google Earth Pro (12/2016). ---	6
Figure 2.2 The Roman Cryptoporticus of Lisbon (Roman galleries of <i>Rua da Prata</i> )-----	7
Figure 2.3 A) Presumptive longitudinal section of the Cryptoporticus with the integration of the hypocaust in the lower galleries. B) Presumed plan of the Cryptoporticus with the linear composition of the thermal spaces. C) preliminary test that it might have laid on the top of the Cryptoporticus, according to the archaeological evidence available up to now (Pedro Vasco Martins – FORMA URBIS Lab/ FAUL). (Form Urbis LAB   CIAUD   FAUL   Pedro Vasco Martins 2019). -----	9
Figure 2.4 Excavation works in the galleries during the archaeological intervention of 2016/17 (CAL). -----	10
Figure 2.5 Drawing of the Cryptoporticus made by Augusto Vieira da Silva in 1934.Provided by CAL.-----	12
Figure 2.6 Extracted from the Geological map of Lisbon sheet number 34-D (Pais <i>et al.</i> , 2006) -----	13
Figure 3.1 Implementation of archaeological surveys 2016/17 with specification of the location of the collected samples from the Roman Cryptoporticus of Lisbon. Base plan provided by CAL.-----	14
Figure 3.2 Sample preparation diagram correlated with the applied techniques. -----	16
Figure 3.3 Thin and Cross section preparation: a) Struers EpoFix resin and hardener, b) Cutting by discoplan T-S, c) Sample in resin solution, d) Grinding by Logitech PM5, e) Gluing the glass slides on cross sections using epoxy resin, f) System Abele press, g) Cutting out the thin sections under vacuum using a Logitech CS10 Thin Section Cut Off Saw, h) Mitutoyo digital micrometer, i) Final polishing by hand on silicon carbide paper, j) Results of thin-sections. 18	18
Figure 3.4 Tools used for the preparation of the powdered samples: a) Disaggregation by mortar and pestle, b) Powdering equipment PM 100 Planetary Ball Mill (Retsch), c) Agate Planetary Mill. -----	19
Figure 3.5 Methodology used and the information gathered for the characterization of the mortars. -----	20

Figure 3.6 Experimentation of the analysis: a) sets of 2 samples, b1,2) HCl aqueous solution and the analyzed sample, c) Heating up the sample in HCl aqueous solution to boiling temperature, d) Filtration under	27
Figure 4.1 Visual estimate percentage (in volume) of the different types of ceramics present in each sample	36
Figure 4.2 . TG/DTG curves of samples from group 1, CR1638-ESC (blue), CR1638-9 (black), CR1638-CLO (red), continuous curves representing TG and dashed curve representing DTG data.	41
Figure 4.3 TG/DTG curves of samples from group 2, CR-1129-A (black), CR-1129-B (red), continuous curves representing TG and dashed curve representing DTG data.	41
Figure 4.4 TG/DTG curves of samples from group 3, CR1706-M6 (blue), CR1706-M4 (black), CR-2204 (red), continuous curves representing TG and dashed curve representing DTG data.	42
Figure 4.5 TG/DTG curves of samples from group 4, CR915-5 (purple), CR1537 (green), CR1131 (red), continuous curves representing TG and dashed curve representing DTG data.	43
Figure 4.6 TG/DTG curves of samples from group 5 (recent samples), CR114 (black), CR139(red), continuous curves representing TG and dashed curve representing DTG data.	43
Figure 4.7 TG/DTG curves of samples from group 6, CR915-5 (purple), CR1537 (green), CR1131 (red) and CR-1706-M2 (black)continuous curves representing TG and dashed curve representing DTG data.	44
Figure 4.8 Calculated percentage of CaCO <sub>3</sub> in the samples from TGA results.	45
Figure 4.9 Representative XRD pattern of GF from group 1samples, (Q: quartz, C: calcite, F: feldspar, I/M: illite or muscovite, k: kaolinite).	46
Figure 4.10 Representative XRD pattern of GF from group 2 samples, (Q: quartz, C: calcite, F: feldspar).	47
Figure 4.11 Representative XRD pattern of GF from group 3 samples, (Q: quartz, C: calcite, F: feldspar, Ilt/M: illite or muscovite, H: hematite A: amphibolite).	47
Figure 4.12 Representative XRD pattern of GF from group 4 samples, (Q: quartz, C: calcite, F: feldspar, Ilt: illite, A: amphibole, D: dolomite).	48
Figure 4.13 Representative XRD pattern of GF from group 5 samples, (Q: quartz, C: calcite, F: feldspar, Ilt/M: illite or muscovite, H: hematite, k: kaolinite, G:geminite).	48
Figure 4.14 Representative XRD pattern of GF from group 6 samples, (Q: quartz, C: calcite, F: feldspar, M: muscovite).	49

Figure 4.15 Elemental maps of sample CR-1638-9; a) BSE image of the general composition, b) EDS spectra of the map c) Si, Ca, K, Mg elemental map, K related to feldspars d) Al elemental map, Al related to micas and feldspars.----- 52

Figure 4.16 a) Point analysis of the binder of CR-1638-9, b) EDS spectrum of the point analysis marked in (a). ----- 52

Figure 4.17 a) BSE image on a preparatory and pigment layer of sample CR-1129B, b) EDS spectra of the map c) Si related to Ca and Mg, d) relation between Ca and Mg, e) Si elemental map. yellow=Si, blue=Ca, green=Mg. ----- 53

Figure 4.18 a) BSE image on the pigment layer of sample CR-1129B, b) EDS spectra of the map c) Si related to Ca and Cu, d) relation between Ca and Mg. yellow=Si, blue=Ca, cyan=Cu. ----- 53

Figure 4.19 a) BSE image on the mortar layer of sample CR-1129B, b) EDS spectra of the map c) point analysis of different aggregates.----- 54

Figure 4.20 a) BSE image on the binder of sample CR-1129B, b) EDS spectra of the binder. ----- 54

Figure 4.21 a) BSE image on the general composition of sample CR-1706M4, b) EDS spectra of the sample, c) Fe related to Ca and Al, d) relation between Ca and Si. yellow=Si, blue=Ca, orange=Al, red=Fe. ----- 55

Figure 4.22 a) BSE image on the binder of sample CR-1706M4, b) EDS spectra of point analysis marked in (a).----- 55

Figure 4.23 a) BSE image on the general composition of sample CR-915-5, b) EDS spectra of the sample, c) relation between Si and Ca, d) Mg related to Ca and Si, e) elemental map of Mg within the composition. yellow=Si, blue=Ca, green=Mg.----- 56

Figure 4.24 a) BSE image on the binder of mortar CR-1131, b) EDS spectra of the sample, c) elemental map of Mg and Ca, d) elemental map of Al. orange=Al, blue=Ca, green=Mg. ---- 57

Figure 4.25 a) BSE image on the general composition of sample CR-139, b) EDS spectra of the sample, c) Al related to Ca and Si, d) K related to Ca and Si. orange=Al, blue=Ca, yellow=Si and magenta=K. ----- 58

Figure 4.26 a) BSE image on the general composition of sample CR-1131, b) are EDS spectra of point analysis marked in (a) ----- 58

Figure 4.27 a) BSE image on the general composition of sample CR-1131, b-e) are EDS spectrum of point analysis marked in (a), c) Ti related to Fe, Ca and Si, d) relation between Ca and Al, e) elemental map of Fe, f) elemental map of Si, g) elemental map of Ti.Green=TI, orange=Al, blue=Ca, yellow=Si and red=Fe. ----- 59

Figure 4.28 a) BSE image on the general composition of sample CR-1628-MP-123, b-d) are EDS spectrum of some point analysis marked in (a). -----	60
Figure 4.29 Mean values obtained from the soluble fractions and insoluble residues after acid attack. -----	62
Figure 4.30 Grain size distribution of mortar samples from group 1.-----	62
Figure 4.31 Grain size distribution of mortar samples from group 2. -----	63
Figure 4.32 Grain size distribution of mortar samples from group 3. -----	63
Figure 4.33 Grain size distribution of mortar samples from group 4. -----	64
Figure 4.34 Grain size distribution of mortar samples from group 5. -----	64
Figure 4.35 Grain size distribution of mortar samples from group 6. -----	65
Figure 4.36 Gravel:mud:sand diagram from GRADISTAT. -----	67
Figure 4.37 Representative grain distribution images sample CR-1628-MP-132 using IMAGEJ software. -----	68
Figure 5.1 Extract from the Geological Chart of the municipality of Lisbon at a scale of 1: 10 000 (MOITINHO DE ALMEIDA, 1986).-----	73
Figure 5.2 CO <sub>2</sub> to structurally bound water ratio in relation to CO <sub>2</sub> %.-----	77

## LIST OF APPENDICES

---

Appendix 1 Tagus River estuary with its fertile islets and the area of <i>Roman Felicitas Iulia Olisipo</i> CML   DMC   DPC   CAL   Mafalda Paiva 2019.....	87
Appendix 2 The Roman Cryptoporticus of Lisbon (Roman galleries of Rua da Prata (taken by the author in sept. 2022).....	88
Appendix 3 The current situation of the Roman Cryptoporticus of Lisbon with applied drainage system (taken by the author in sept. 2022). ....	89
Appendix 4 The current entrance to the galleries, located at the intersection of Rua da Prata and Rua da Conceição, Sept.2022. ....	90
Appendix 5 3D-Model with reconstitution of Cryptoporticus and building that lay above it. CML   DMC   DPC   CAL   Mafalda Paiva 2019.....	91
Appendix 6 Thermograms of the powdered samples from the Roman Cryptoporticus of Lisbon. ....	92
Appendix 7 X-ray diffractogramis of the powdered samples from the Roman Cryptoporticus of Lisbon. ....	95
Appendix 8 Results of the acid attack analysis of the samples from the Roman Cryptoporticus of Lisbon. ....	98
Appendix 9 Results of the granulometric analysis, grain size distribution of the insoluble residue. ....	99
Appendix 10 Insoluble residues obtained after acid attack, observations under Stereozoom microscop.....	100

# 1 INTRODUCTION

---

## 1.1 AIMS OF STUDY

Heritage, whether tangible or intangible, movable or immovable, is invaluable, left by ancestors and passed on to generations through time. Regarding immovable heritage such as buildings and heritage sites, the worldwide has begun to pay more attention, both in terms of restoration and preservation, in order to ensure its sustainability. Sustainability is one of the five pillars of the framework for action on cultural heritage. Through experimental analysis, the thesis will carry out the characterization of mortars from the Roman Cryptoporticus of Lisbon aiming to illustrate how the most suitable intervention can be done in ways that respect the heritage value of the site and to achieve sustainable conservation.

Mortar, as one of the fundamental construction materials throughout the ages, is also one of the thorny issues when talking about the conservation of heritage buildings. Its analysis and understanding have become one of the most intensively studied areas in the world of science and cultural heritage, in order to better understand the past and get a better idea of the materials they used and the techniques they employed and how they applied.

As part of the Erasmus Mundus Archaeological Materials Sciences Joint Master's Degree (ARCHMAT), the work carried out aimed to scientifically study mortars mainly from the Roman Cryptoporticus of Lisbon. This archaeometric study was undertaken at the HERCULES Laboratory of University of Évora, Geosciences and Chemistry & Biochemistry Laboratories of School of Sciences and Technology of University of Évora, Portugal.

The main objective of the study was to characterize the mortars from the Roman Cryptoporticus of Lisbon, Portugal, from a textural, mineralogical and chemical point of view by the means of analytical techniques, in order to obtain information about the production technology and the raw materials used in their manufacture. It also aimed to clarify the possible origins of the raw materials used, taking into account the availability of the resources. It aimed also to increase the knowledge of ancestral construction techniques, in order to help in the future plan of rehabilitation, conservation and restoration of the site.

The analytical techniques for the determination of the characteristics of the samples were performed by means of Optical Microscopy (Stereo zoom and Petrographic microscope), powder X-ray Diffraction (XRD), Thermogravimetric analysis (TGA-DTG), Scanning Electron

Microscopy coupled with Energy Dispersive X-ray Spectroscopy (SEM-EDS), Acid Attack and Granulometric Analysis.

## 1.2 MORTARS

Mortar is an artificial material resulting from the mixture of at least one binder with aggregates and water with some organic or inorganic additives for special constructional needs (Stefanidou *et al.*, 2014), they are widely spread binding materials used in built structures, and their composition varies depending on their specific function and the context of the construction. (Elsen, 2006; Artioli, 2010). The function of mortars may vary from structural supporting, joining, flooring, finishing internally (plastering) or externally (rendering), decorating or waterproofing (Elsen, 2006). The use of lime mortars is dated to the early sixth millennium B.C, and their earliest use as binding material is dated to the third millennium B.C, in Egypt (Delatte, 2001).

Aggregates have a strong influence on the behavior of the mortars, they may vary depending on where they were acquired, their type or the function of the mortar. There are several factors that affect the behavior of the mortar and its workability, such as hardness, grain shape, granulometry, mineralogy and porosity of the additives (Artioli, 2010). The primary function of the aggregates is to restrict the shrinkage of the mortar paste during sitting. Aggregate grains, mainly deriving from quartz sand as sediment from a river or a sand quarry and they consider as the skeleton of the mortar, which gains cohesion to the binder through the binding of its grains (Margalha, 2011). According to previous studies it appears that the mixture of finer and coarser sands contributes to a better arrangement, reducing porosity, allowing an improvement in some parameters (Margalha *et al.*, 2007; Rato, 2006).

Typically, natural sand is the most abundant form of aggregates although, crushed stones, ceramics or shells have been used extensively throughout the ages, especially during the Roman period (Schnabel, 2008). The use of lime-based mortars and plasters was a very widespread during Roman times. The techniques used by architects and artisans to produce binding materials at the time of the Roman Empire were substantially based upon those described by Vitruvius in his handbook *De Architectura* (Vitruvius, 1960; Artioli 2010).

Binders are products used to bind or joint other granular materials, for example sands, i.e., to keep the aggregate grains together. The two main types of mortars are; aerial mortar, which set in contact with air, and hydraulic mortar, which set in contact with water. Most typically, there

are three binders that have been used throughout history until recent times which are mud/clay, gypsum and lime mortars (Elsen, 2006). Air lime has a greater specific surface area than hydraulic binders, which requires a greater amount of mixing water. For this reason, drying is accompanied by a certain shrinkage, greater than that in hydraulic binders, causing greater porosity in the mortar (Rodriguez, 2012).

### 1.2.1 Lime mortar

Lime-based mortar had a wide use and distribution in the construction of ancient buildings, specifically during the Roman times (Adam, 1989). Among the Roman mortars, lime has been considered the most common mortar binder in the historical context (Schnabel, 2008). Although mortars generally maintain their chemical composition, it has been found that, over time, chemical reactions can occur between the silica in the sand and calcium carbonate, when dealing with lime mortars (Rayment, Pettifer 1987). Lime is made from limestone and to convert this raw material into lime it requires three main processes (calcination or burning, hydration or slaking and carbonation or hardening). This is known as the lime cycle (Fig. 1-1). The lime cycle is composed by series of chemical reactions and it is one of best-known examples of chemistry that is naturally occur (ICCROM, 1981).

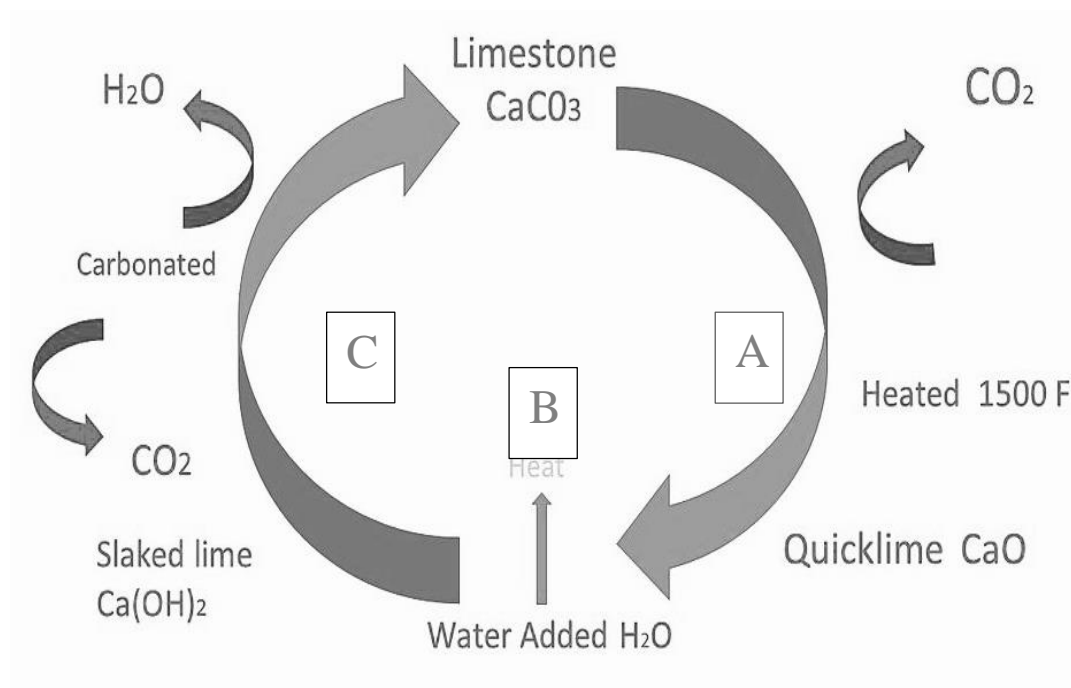


Figure 1.1 The lime cycle. A) calcination, B) hydration and C) carbonation.

The reactions involved in lime manufacture are:

- **Calcination or burning (A)**

Calcination or burning of limestone ( $\text{CaCO}_3$ ) is a highly endothermic reaction. The reaction only begins when the temperature is above the decomposition temperature of the carbonates in the limestone to produce calcium oxide ( $\text{CaO}$ ) also named as quicklime, and carbon dioxide ( $\text{CO}_2$ ) as shown in equation [1]. This burning process typically starts between  $780^\circ\text{C}$  and  $1340^\circ\text{C}$  in a specific kiln (Bogward, 1985).



- **Hydration or slaking (B)**

After calcination, the quicklime ( $\text{CaO}$ ) is unstable, and when water is added it react often very rapidly to form calcium hydroxide ( $\text{Ca(OH)}_2$ ). This is known as hydration or slaking (Lanas, Alvarez, 2004). The reaction is exothermic, which means that energy is released during the process. There are two possible outcomes of the hydration process, either a dry powder or a lime paste is formed. The dry powder is formed when just enough water was involved in the slaking process, it is also called hydrated lime. Whilst the lime paste or lime putty is formed by the addition of excess water, which is also known as slaked lime, as shown in equation [2] (Rodríguez-Navarro, 2012).

In the case of dolomitic lime, the slaking would happen slowly in comparison with calcitic lime (Artioli, 2010).



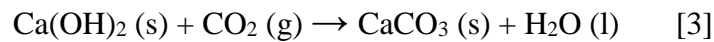
- **Carbonation or hardening (C)**

The re-carbonation process is the opposite of the calcination process. Both quicklime and hydrated lime, when exposed to the air for long periods, react with carbon dioxide from the atmosphere. This process leads to the formation of slaked lime as shown in equation [3]. The lime mortar carbonation is controlled by two mechanisms:

- 1) Carbon dioxide diffusion from the air through the porous system up to the reaction front (drying and wetting process).

2) The reaction of the diffused carbon dioxide with calcium hydroxide  $\text{Ca(OH)}_2$  (Balen, Gemert, 1994).

The limestone used for the burning may contain magnesium carbonate in its composition, this situation affects the temperature of the calcination since they behave slightly different due to their magnesium content.



### 1.2.2 Aerial lime mortar

Air lime mortars were used in construction since ancient times until the 20<sup>th</sup> or 21<sup>st</sup> century. Air lime is obtained from limestone and doesn't set in water, as it has no hydraulic properties, it sets in air by reaction with atmospheric carbon dioxide (IPQ, Margalha, 2011). The behaviour of air lime mortars is determined by both physical factors, porosity of the mortar, nature, shape and dimension of the aggregates and chemical factors, type of lime, degree of carbonation, secondary compounds, dimension and shape of crystals (Stefanidou, Papayianni 2005).

### 1.2.3 Hydraulic lime mortar

The raw material for hydraulic lime is a limestone which contains calcium carbonate together with a proportion of clay. Most limestones for hydraulic lime production contain silica together with alumina. It has the property of setting and hardening when mixed with water or when immersed in water and the reaction with atmospheric carbon dioxide is part of the hardening process. The hydraulic lime is obtained by firing, between 900°C and 1200°C (IPQ, 2011).

The Romans were the first to develop hydraulic mortars, used to mix lime with pozzolana of either volcanic ash or brick dust. The mixture hardens much faster and allows for its use in waterborne structures and heritage structures (Chen, *et al.*, 2018). Roman mortars related to hydraulic structures have a specific characteristic, which is the use of *opus signinum* obtained by mixing lime-based mortars with fine sand and a huge percentage of ceramic fragments or crushed pottery (Borsoi *et al.*, 2019). Crushed ceramics have been used for structures related to water bearing facilities, mainly to protect the walls from the moisture (Elsen, 2006).

## 2 ARCHAEOLOGICAL CONTEXTS

---

### 2.1 HISTORICAL BACKGROUND

The Roman Cryptoporticus of Lisbon (38°42'3".7"N 9°08'1".8"W), or what is also known as the Roman Galleries of *Rua da Prata*, it is a subterranean monument in downtown Lisbon (Fig. 2-1).

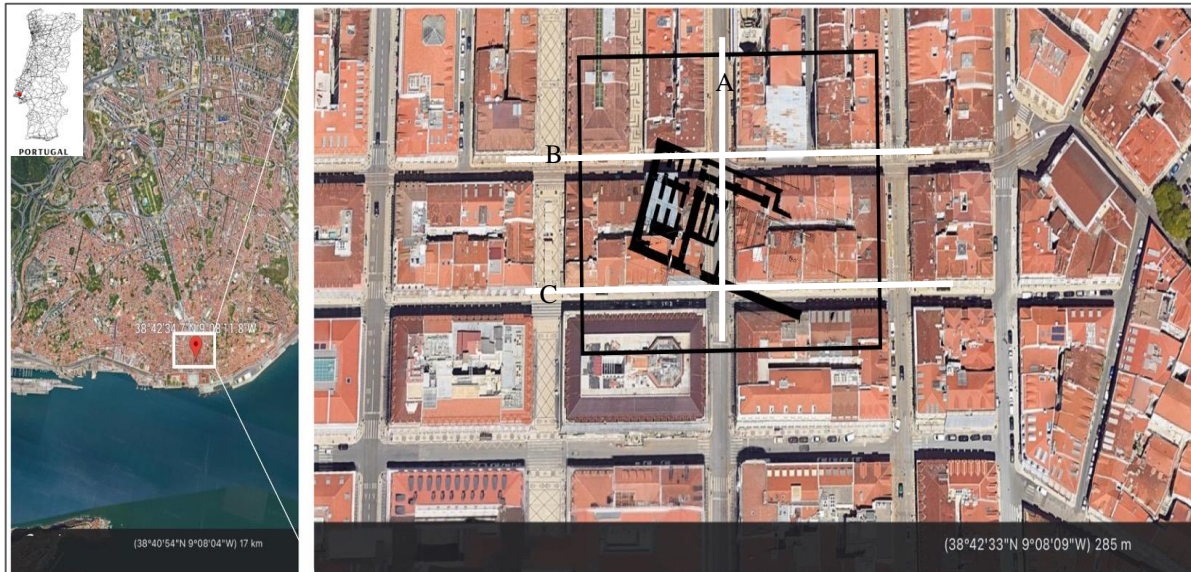


Figure 2.1 Location of the Roman Cryptoporticus in Lisbon, Portugal. A) Rua da Prata B) Rua da Conceição C) Rua da São Julião. Base images taken from Google Earth Pro (12/2016).

The Roman Cryptoporticus of Lisbon was built in the mid-1<sup>st</sup> century AD like others monuments of the Roman Felicitas Iulia Olisipo (Appx. 1) such as the Roman Theatre and the Cassia Baths (Silva,1934). The Roman Galleries of *Rua da Prata* are a chain of vaulted subterranean galleries hidden in the downtown area of *Pombaline* under the blocks outlined by *Rua da Prata*, *Rua da Conceição* and *Rua of São Julião* (Fig. 2-1).

Like other important archaeological monuments in the city of Lisbon, the Roman Cryptoporticus was discovered after the 1755 earthquake, more precisely when the complex now classified as “*Baixa Pombalina*” was built. In 1773, the installation of the collector on *Rua da Prata* intercepted the building, which was immediately recognized as Roman underground monument, constituted by a network of galleries of different dimensions, vaulted, parallel and perpendicular to each other (Moita, 1977) (Appx. 2). The entrance to the galleries, located at the intersection of *Rua da Prata* and *Rua da Conceição* (Moita, 1977). At the time of its discovery, the interior of the monument was already flooded due to the higher water table level

present today compared to the 1<sup>st</sup> century AD, and Pombaline urbanism took advantage of the spring to supply its residents as probably in previous times. Well mouths were opened in the vaults of the Roman structure, and other pre-existing ones were reused, and the galleries started to be used as a cistern known as *Conservas de Água da Rua da Prata*. However, the reconstruction and operation of the sanitation infrastructure of Lisbon after the earthquake (which crossed the Roman monument), ended up causing contamination of the water, and in 1868, an exhibition presented by the municipal services doctor, Augusto José Mesquita, reported on the dangerous consequences for public health due to using the water from the galleries of *Rua da Prata* (Moita, 1977). The Lisbon City Council then carried out repair works on several sections of sanitation infrastructure and coating the interior walls and the floor of the galleries with hydraulic plaster, as well as the interior walls of the wells, in an attempt to prevent contact between the inside of the water tank and the collectors (Moita, 1977; Caessa, Nozes and Mota, 2016). Currently, the galleries are permanently flooded, due to the higher water table level present today compared to the 1<sup>st</sup> century AD (Fig. 2-2) (Appx. 3).

The Cryptoporticus has recently been studied by several scholars from the architectural, archaeological, and historical point of views aiming to identify the historical background, and its function.



Figure 2.2 The Roman Cryptoporticus of Lisbon (Roman galleries of *Rua da Prata*)

### 2.1.1 Function of the Cryptoporticus

Since the discovery of the vaulted complex in 1773 to the present day, there have been several interpretations attributed to the functionality of the Cryptoporticus. The first hypothesis was a spring of water, because it was flooded when it was discovered, and the water seemed to spring naturally from the ground. And nearby there was a pedestal with an inscription dedicated to Aesculapius, the god of medicine (Moita, 1977), that currently integrates the collection of the National Museum of Archeology in Lisbon and classified as a national monument. Then it was used as a cistern during the modern period or earlier the discovery, there were also those who proposed the function as a cistern for the building since its origins.

Throughout time and during the 18<sup>th</sup> and 19<sup>th</sup> centuries, the initial function of the galleries has been identified by Thomaz Caetano as a baths complex (part of thermal baths) (Fig. 2-3), and Friar José de S. Lourenço defined the Roman Galleries as a series of crypts (Fabião, 1994).

One of the hypotheses that unanimously agreed is the hypothesis proposed by Vasco Mantas that it might have been an architectural solution to support a construction of large buildings (usually public) in an area with a slope and little geological stability, as a result of its proximity to the Tagus River (Appx. 4) (Fabião, 1994 Caessa, Nozes and Mota 2016).

Naturally, it had become relatively evident that this vaulted structure would have the objective of leveling an upper level suitable for the installation of buildings, specifically in an unstable area on the river front made up of fluvial beach sands. Studies carried out at the time for other similar constructions, such as the Cryptoporticus of the *Aeminium* forum (Oleiro and Alarcão, 1973), and the *Conimbriga* forum, attributed to this type of structure has a specific architectural function, that is supporting the perimeter area of the temple (Alarcão and Etiénne, 1973).

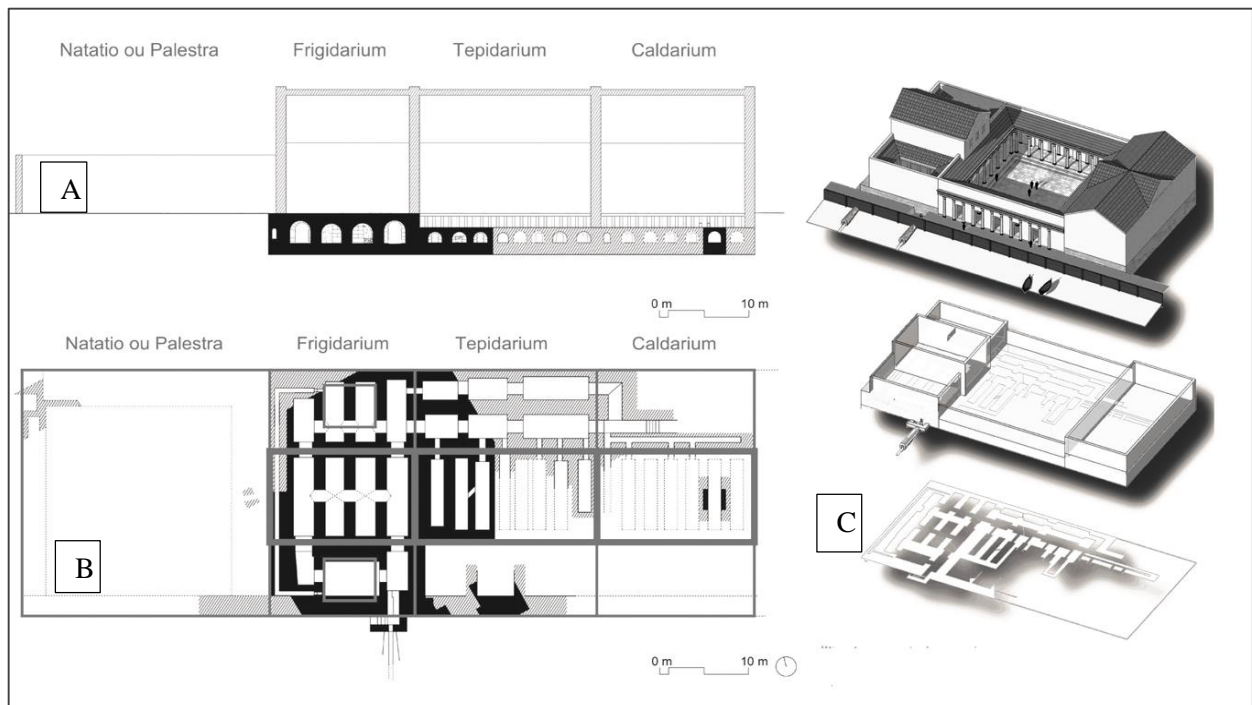


Figure 2.3 A) Presumptive longitudinal section of the Cryptoporticus with the integration of the hypocaust in the lower galleries. B) Presumed plan of the Cryptoporticus with the linear composition of the thermal spaces. C) preliminary test that it might have laid on the top of the Cryptoporticus, according to the archaeological evidence available up to now (Pedro Vasco Martins – FORMA URBIS Lab/ FAUL). (Form Urbis LAB | CIAUD | FAUL | Pedro Vasco Martins 2019).

## 2.1.2 Excavation

The first archaeological intervention carried out in the Roman Cryptoporticus dates from 1859 (Andrade, 1859). The installation of the Cryptoporticus on *Rua da Conceição*, allowed the description and design of the traces found at that time. Francisco de Andrade and Valentim de Freitas, employees of the National Library, an entity at the time responsible for the archaeological heritage, were called to the site and, faced with adverse conditions typical of an archaeological emergency, they carried out highly relevant records about the site and the excavation works that are still available today (Sequeira, 1934).

Throughout the remaining century, the tutelary role that the Lisbon City Council played, through organized visits, publications, monitoring and preventive conservation, would become evident in 1995/96 when the Archeology Service of the City Museum carried out an intervention scientifically conducted archaeological site, specifically inside the galleries that can be visited (Fig. 2-4). On this occasion, a sounding was opened in the floor of one of the larger galleries, two geotechnical holes were made in the base plate, wall engravings and the graphic record of elevations (Caessa, Nozes and Mota, 2016).



Figure 2.4 Excavation works in the galleries during the archaeological intervention of 2016/17 (CAL).

More recently, from 2015 onwards, the Lisbon Archeology Center (CAL) had the opportunity to develop new archaeological interventions in the buildings located at *Rua da Conceição*, 73-77 and *Rua da Prata*, 45-51/ *Rua de São Julião*, 86-106. In the first building, the Lisbon City Council, as co-owner, intervened to diagnose the condition of the Pombaline foundations and the upper part of the Cryptoporticus, through three underground surveys, which in the future will be extended to the entire ground floor (Caessa, Nozes and Mota, 2016).

Inside the basement of the second building (licensed in 1913 by the municipality), located on the same block, and whose construction mutilated part of the monument, a partnership between the CML and the private developer made it possible to carry out a broader archaeological diagnostic intervention, identifying new structures and the unblocking of one of the galleries of the vaulted complex that will enable the creation of a new safe and inclusive access to the interior of the monument's visitable area (Mota, Martins 2018).

### 2.1.3 Architectural description

The total configuration of the orthogonal plan of the roman Cryptoporticus, devoid of a completely understandable proportion and symmetry, bringing the Cryptoporticus closer to a design more adjusted to known forensic architecture and expanding the area available for the installation of a square at the top (Ribeiro, 1994). The street pavement is 5.70m above sea level, the floor of the galleries is located at a variable height between 1.09m and 1.42m above sea level. The galleries, with heights varying from 1.3m to 2.7m, are filled with water up to about 1.2m in height due to the water level difference compared to 1<sup>st</sup> century AD.

The building was rediscovered in 1859, during the repair work on the *Rua da Prata* collector, Figure 2-5 is a plan of the known part of the building, dating from 1934 and has been published by CML. It is assumed that the original construction would have been much larger, occupying the subsoil underlying most of the blocks delimited by *Rua dos Fanqueiros* and *Rua Augusta*, to the east-west, and by *Rua da Conceição* and *Rua de São Julião*, to the north-west. The construction is essentially constituted by a series of vaulted galleries, relatively short, that intercommunicate, connected laterally or at the tops (Andrade, et al., 1859). These galleries formed the water reservoir intended for local baths and would also be used for public supply to the city in periods of drought.

The galleries (walls, vaults, and floors) are made of stone masonry with hard mortar, with the walls covered in some sections by ashlar with padding. The vaults are reinforced, in the areas where the galleries intersect, by stonework arches. The Roman pavement, on which a new pavement was built at the end of the last century, is very thick, from 0.8 to 1.0 m, according to recent archaeological surveys (Caessa, Nozes and Mota, 2016).

The basement inside the building, an authentic total interfacial element, had a ceiling height of 2.80 meters. The obstruction of the gallery was 7.50 meters long, the lower half of which dates from the second half of the 18<sup>th</sup> century and is made up of small to large-caliber stone rubble and shapeless stone blocks. The upper half consisted of an extensive boarding of small to large caliber pebbles, bonded with a grayish white mortar of good strength, sealed on both sides by a plaster with the same characteristics. Although the materials did not make it explicit, this cladding. it was also possible, thanks to a semicircular rupture carried out in the Islamic Medieval Period, perhaps an attempt to open a well, to recognize the thickness of this layer (about 0.5 meters thick) and the filling of compressed limestone gravel. Remaining plasters visible in the galleries that can be visited, were apparently made in the second half of the 19<sup>th</sup>

century by municipal initiative, probably in 1868, due to the contamination of “water preserves” by the sewage collector at *Rua da Prata* (Moita, 1977).

The current access is in the middle of *Rua da Conceição*, close to the tram line nº 28 (with steep and narrow staircase) opened by the CML with the aim of facilitating visits (Appx. 5). Currently, the galleries support two Pombaline buildings, with direct foundations resting on the vaults.

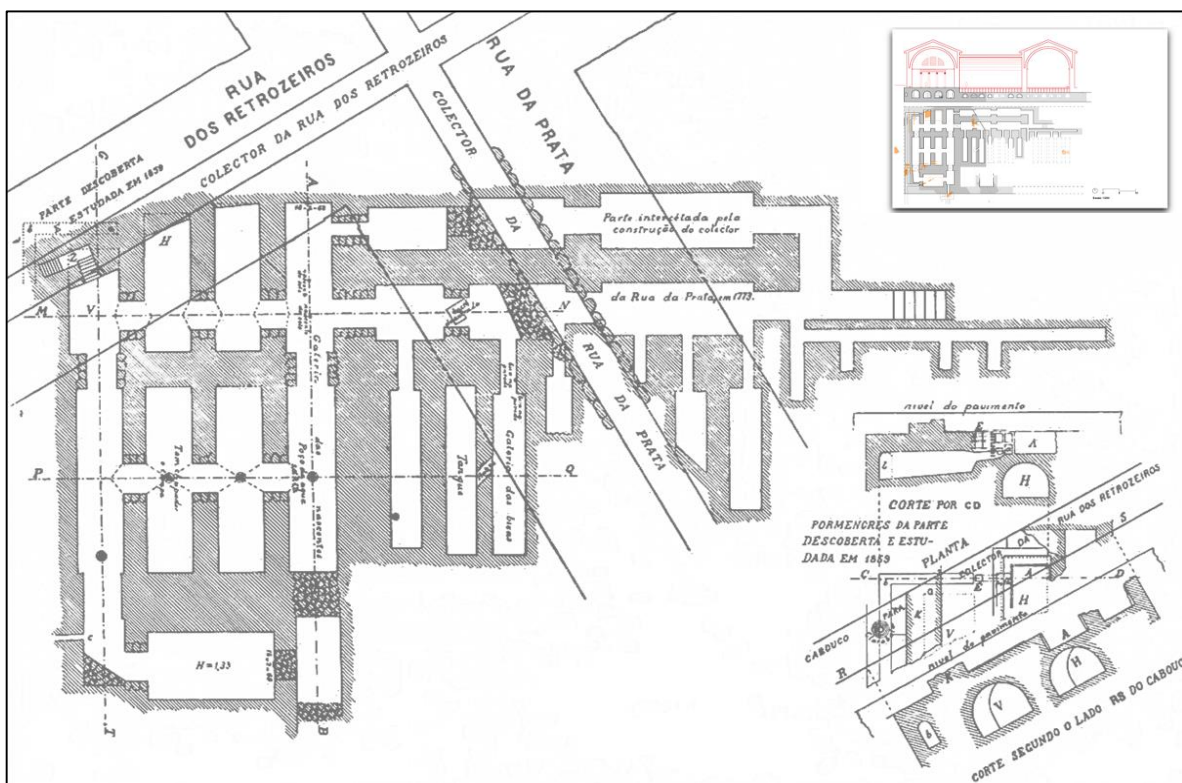


Figure 2.5 Drawing of the Cryptoporticus made by Augusto Vieira da Silva in 1934. Provided by CAL.

## 2.2 GEOLOGICAL CONTEXT

The intervention site, from which the studied samples were collected, is located between the foothills and the southern half slope of the hill of S. Jorge, in the historic center of the city of Lisbon. Geologically, Lisbon is located within the Lusitanian Basin and the Lower Tagus Basin (Lopes 2001), in the center-southwestern coast of Portugal.

The study area is the county of Lisbon which represents an area of about 84 km<sup>2</sup>. The city of Lisbon is rich in different subsurface geological formations that are well documented in various





Table 3.1 General description of the samples.

<i>Groups</i>	<b>Sample</b>	<b>Place</b>	<i>Painting layer</i>	<b>Location</b>	<b>Function</b>	<i>Period</i>	<b>Typology</b>
<b>1</b>	<b>CR-1638 CLO</b>	EU-16	No	Floor	Filling mortar	Roman	—
	<b>CR-1638 ESC</b>	EU-16	No	Floor	Render mortar	Roman	—
	<b>CR-1638-9</b>	EU-16	No	Floor	Render mortar	Roman	—
<b>2</b>	<b>CR-1129A</b>	EU-11	Yes	Wall	Render mortar with painting layer	Roman	—
	<b>CR-1129B</b>	EU-11	Yes	Wall	Render mortar with painting layer	Roman	—
<b>3</b>	<b>CR-1706 M4</b>	EU-17	No	Wall	Render mortar	Roman	Opus Signinum
	<b>CR-1706 M6</b>	EU-17	No	Wall	Render mortar	Roman	Opus Signinum
	<b>CR-2204</b>	EU-22	No	Wall	Render mortar	Roman	Opus Signinum
<b>4</b>	<b>CR-915 G</b>	EU-9	No	Wall	Filling mortar	Roman	Opus Caementicium
	<b>CR-915-5</b>	EU-9	No	Floor	Filling mortar	Roman	Opus Caementicium
	<b>CR-915-6</b>	EU-9	No	Floor	Filling mortar	Roman	Opus Caementicium
	<b>CR-915-8</b>	EU-9	No	Floor	Filling mortar	Roman	Opus Caementicium
	<b>CR-915-10</b>	EU-9	No	Floor	Filling mortar	Roman	Opus Caementicium
	<b>CR-915-18</b>	EU-9	No	Floor	Filling mortar	Roman	Opus Caementicium
	<b>CR-1131</b>	EU-11	No	Floor	Filling mortar	Roman	Opus Caementicium
	<b>CR-1537</b>	EU-15	No	Floor	Filling mortar	Roman	Opus Caementicium
	<b>CR-1539 "Gato"</b>	EU-15	No	Floor	Binding mortar	Roman	Opus Caementicium
<b>5</b>	<b>CR-114</b>	EU-1	No	Wall	Filling mortar	19 <sup>th</sup> century	—
	<b>CR-139</b>	EU-1	No	Wall	Filling mortar	21 <sup>st</sup> century	—
<b>6</b>	<b>CR-1517</b>	EU-15	No	Floor	Filling mortar	Roman	—
	<b>CR-1706, M 2</b>	EU-17	No	Wall	Filling mortar	Roman	Opus Caementicium
	<b>CR3007</b>	EU-30	No	Floor	Filling mortar	Roman	Opus Cementicium
	<b>CR3012'</b>	EU-30	No	Floor	Filling mortar	Roman	—
<b>IND.</b>	<b>CR-1628, MP-132-AMB 3</b>	EU-16	No	Un-known	Decorative?	Roman	—

### 3.2 SAMPLE PREPARATION

Various analytical techniques existing for the characterization of historic mortars, either destructive or invasive. Each technique has a specific sample preparation to implement each analysis. Preparation procedure for the studied samples has been correlated with the desired analytical techniques. According to the methodology, each sample was transformed into fragments, powders, and sections (cross and thin sections) as shown in figure 3-2.

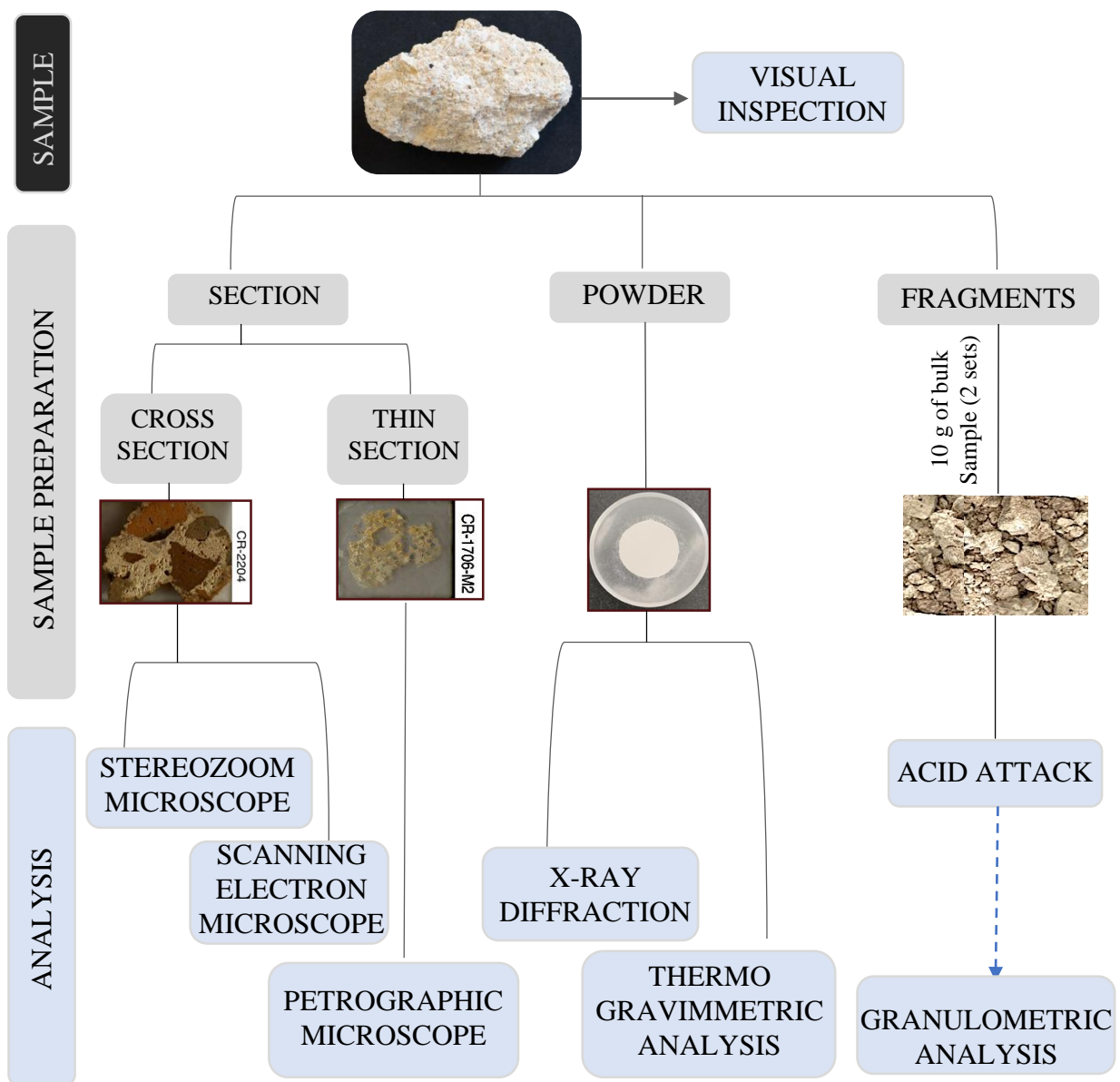


Figure 3.2 Sample preparation diagram correlated with the applied techniques.

Before any preparation, all samples were cleaned with a brush and scalpel to remove any dirt, dust and or any kind of biological colonization. Samples then were left to dry in a ventilated oven overnight at 40°C to guarantee a well-dried. After the cleaning process is completed, all samples were photographed for the macroscopic characteristics.

### **3.2.1 Sectioned Samples - Preparation for Optical/Stereo Microscopy**

Samples were prepared as polished surfaces/cross sections (Fig. 3-3c), for Stereo microscopy and SEM-EDS analysis and thin sections (Fig. 3-3j), for petrographic analysis and SEM-EDS as well. In order to analyze the samples under the petrographic microscope, the samples had to be specially prepared to obtain thin sections that light could penetrate for petrographic study. Thin sections were prepared out of cross sections using TS-Method developed by Struers (Struers, 2014). For the preparation of this thin sections, glass slides were unpolished using the LOGITECH PM-5 equipment with P #1000 silicon carbide powder for 65 minutes and 60 RPM (Round Per Minutes) to achieve a glass thickness between 1.11-1.15mm for better attachment with the sample surface. Thin sections were prepared from cross sections of the samples already prepared to be studied by stereo zoom. First, the samples were placed facing the bottom in a mounting plastic cup and embedded in a mixture of 25 g of EpoFix Resin and 3 g of EpoFix Hardener (Fig. 3-3a), and then left to set overnight at room temperature. After completion of the setting process, the samples were dismantled from the plastic containers and cut in the Discoplan-TS (Fig. 3-3b) and then the surface of the samples was polished using LOGITECH PM-5 equipment with P #1000 silicon carbide powder to expose the surface of the samples for 20 minutes at 60 rpm (Fig. 3-3d). Afterward, the cross sections were polished again by hand in P #1200 SiC Paper to reach a perfectly flat and clear surface that can be studied under the petrographic microscope. Then, glass slides and cross-sections were thoroughly cleaned with acetone and placed into a hot plate at 50°C temperature for 6-10 minutes. The cross sections later glued in the glass slides (Fig. 3-3e), using a mixture of 2 g of EpoThin Resin and 0.9 g of EpoCure Hardener, and left to set overnight in a hot plate under mechanical press used to fix the samples and to apply pressure while the Epoxy resin is setting (Fig. 3-3f). The Discoplan-TS blade was then used to cut the cross sections (the cross sections glued on glass) to start the grinding process (Fig. 3-3g). The grinding of the thin sections was done carefully in 2 runs at 60 rpm for a duration of 20 minutes for each run. The thickness was measured precisely after every run using Mitutoyo digital micrometer (Fig.3-3h) to reach a thickness between 30-40 µm, according to (Middendorf et al, 2005a). Final grinding and polishing were done by hand using

P #1000 and P #2500 silicon carbide sand sheet gently until the samples showed the first order Birefringence color in the Michel-Levy chart under Optical Microscope (Fig. 3-3i), then the samples have been left for 3 minutes to rinse in an Ultrasonic Cleaner USC-T (VWR). None of the samples were coated or treated for any of the analysis.

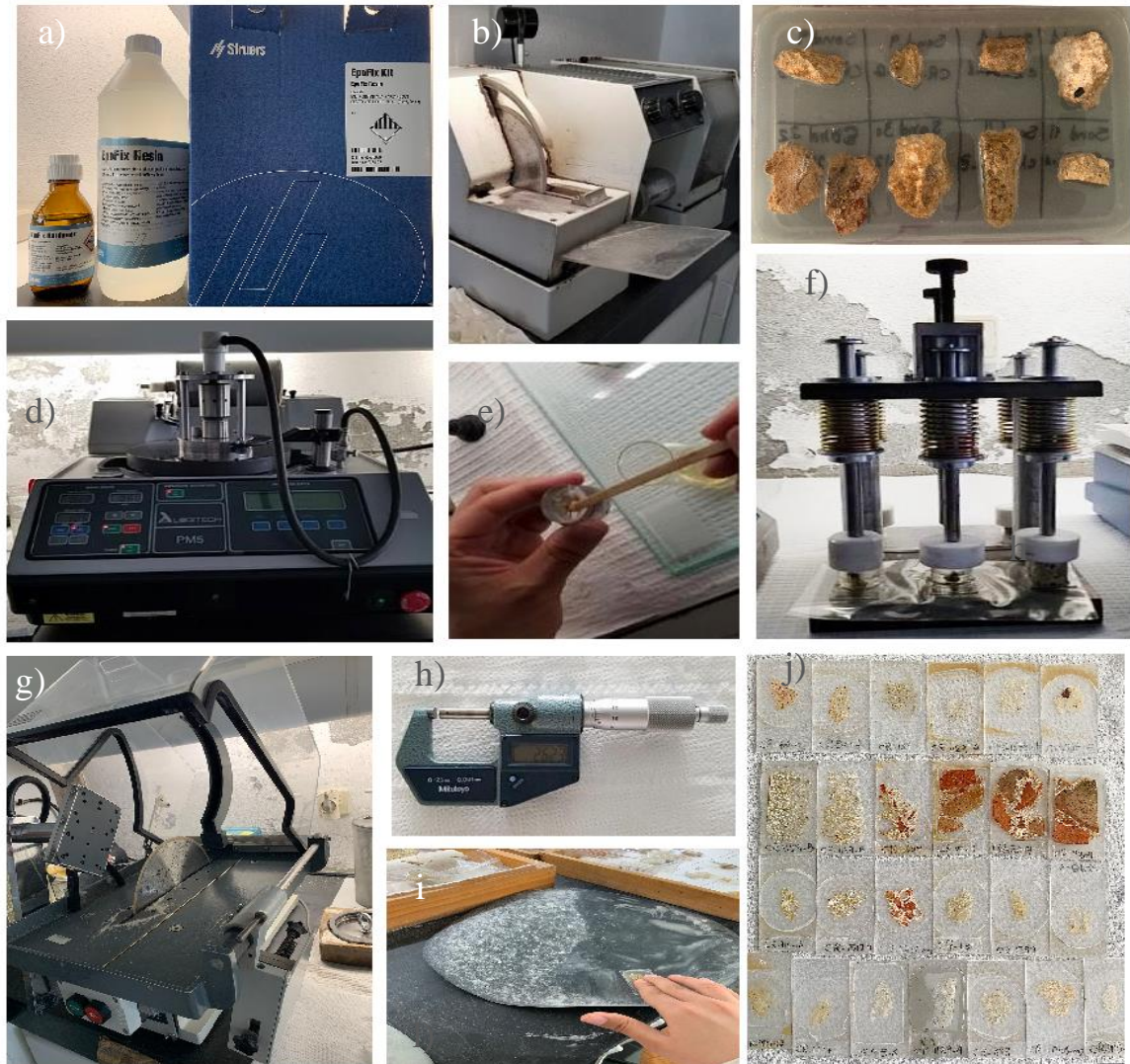


Figure 3.3 Thin and Cross section preparation: a) Struers EpoFix resin and hardener, b) Cutting by discoplan T-S, c) Sample in resin solution, d) Grinding by Logitech PM5, e) Gluing the glass slides on cross sections using epoxy resin, f) System Abele press, g) Cutting out the thin sections under vacuum using a Logitech CS10 Thin Section Cut Off Saw, h) Mitutoyo digital micrometer, i) Final polishing by hand on silicon carbide paper, j) Results of thin-sections.

### 3.2.2 Powdered Samples - Preparation for X-Ray Diffraction and Thermogravimetric Analysis

For X-Ray Diffraction and Thermogravimetric Analysis, it was important to prepare powder samples. For this purpose, around 5-10g of each sample was gently disaggregated using a rubber hammer in order to obtain smaller fragments, and the harder samples were ground by hand in

an agate mortar (Fig. 3-4a). Two samples contained a chromatic layer and a preparation layer, the process for preparing them started first with removing both layers before starting to prepare the powder for those samples. Then, all samples were ground a PM 100 Planetary Ball Mill (Retsch) (Fig. 3-4b) in an agate grinding jar with 3 grinding balls (<1cm Ø) were used (Fig. 3-4c). The dry grinding was done at 500 rpm 10 minutes.

The processes were repeated twice for some samples in order to completely dispose of samples with harder fragments, such as ceramic or quartz grains, to obtain a homogeneous powder.

The global fraction powder was used for the mineralogical characterization by XRD, and to quantify the carbonate compositions within the bulk sample by means of TGA.

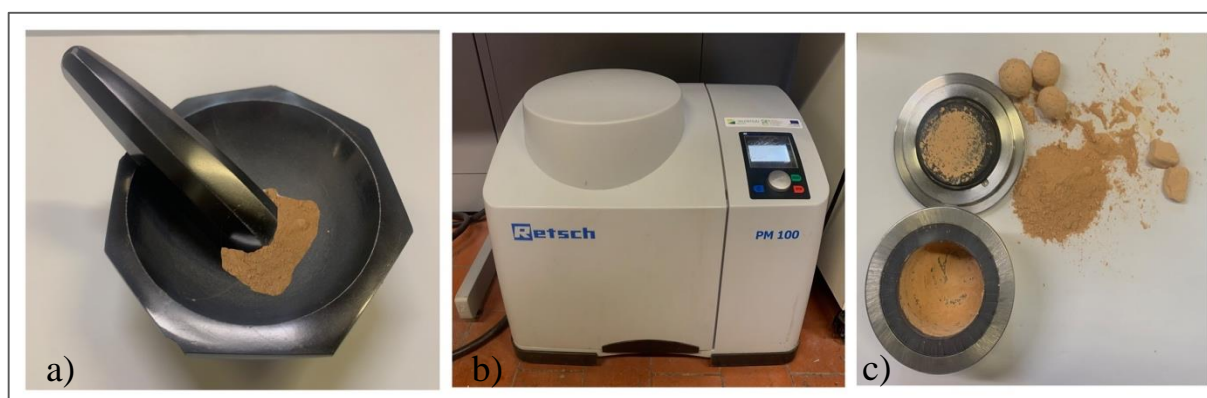


Figure 3.4 Tools used for the preparation of the powdered samples: a) Disaggregation by mortar and pestle, b) Powdering equipment PM 100 Planetary Ball Mill (Retsch), c) Agate Planetary Mill.

### 3.2.3 Fragmented samples - Preparation for Acid attack and Granulometric Analysis.

Fragmented samples were needed for Acid attack and Granulometric analysis, around 20 g of each sample was acquired to perform these techniques. To minimize experimental error two sets of 10g fractions were acquired for the analysis. In some cases, due to the lack of material, 10 g only have been taken and the analyses has been done only on one set (CR-1638CLO and CR-915-10) and for sample (CR- 1628-MP132), no acid attack and granulometric analysis were conducted. The selection of the fragmented portion was chosen carefully in order to have a representative sample for the analysis containing a mixture of all fractions homogenously. Samples with chromatic layer (CR-1129A and CR-1129B), the chromatic layer has been removed first before the disintegration. The initial weights of each set were recorded before the analysis so that they could be compared with the final weights after treating with hydrochloric acid aqueous solution.

Chemical analysis by the mean of acid attack was the last technique to apply on the samples as recommended by Middendorf, to have an idea whether or not the aggregates may dissolve with acid (Middendorf *et al.*, 2005b). The resulting insoluble residue is used to carry out the granulometric analysis.

### 3.3 ANALYTICAL TECHNIQUES AND METHODS

The characterization of the mortars from a textural, mineralogical and chemical point of view was carried out through the application of several complementary analytical techniques. The assessment of their characteristics was first executed by visual examination and microscopic observations through stereoscopic and petrographic microscopes. Thermogravimetric analysis (TGA-DTG) in combination with acid attack and granulometric analysis was used to determine the proportion of carbonates, of soluble fraction and of aggregates of each sample (Jedrzejewska, 2014). Powder X-Ray Diffraction (XRD) was used to gather information about the crystalline phases present in the powdered samples, which complemented the previous microscopic and elemental composition results. Variable Pressure Scanning Electron Microscopy coupled to Energy Dispersive X-ray Spectrometry (VP- SEM-EDS) has been used also to determine the chemical composition of binder and aggregates trough elemental map distribution or punctual analyses (Fig. 3-5).

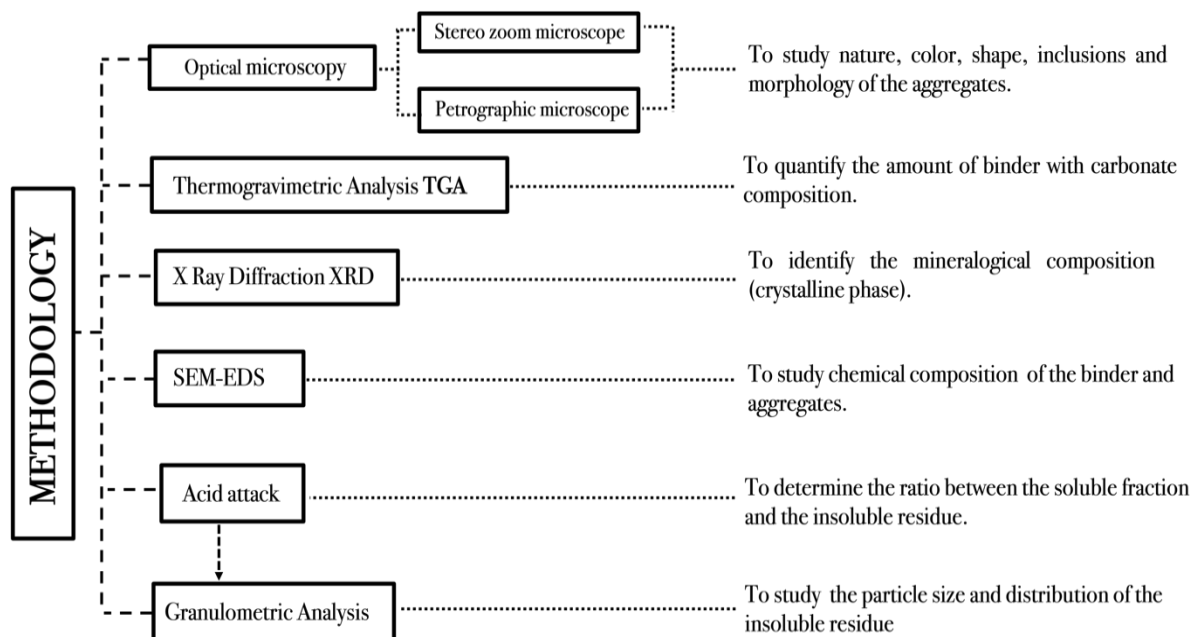


Figure 3.5 Methodology used, and the information gathered for the characterization of the mortars.

### **3.3.1 Visual inspection**

A visual inspection is a vital step in the future rehabilitation process of the structure took place. This procedure allowed characterizing the structural elements and materials and identifying the critical zones of the structure (Artioli, 2010). A visual inspection will normally include a basic description of physical qualities, including whether it is soft/hard or friable, and can allow some assumptions to be made about the strength of the mortar, and it must be the first step to perform the analysis and characterization of historic mortars and also amongst all the other analytical techniques employed (Stuart, 2007).

Inspection in normal conditions allows an assessment of color, types, distribution and sizes of aggregate, the presence of unburned limestone, shell or coal inclusions and additives. For this purpose, macroscopic observations with an unaided eye might be of use to make a broad description of the samples regarding their general features (Groot *et al.*, 1999). The samples could be grouped together based on these initial results from the visual inspection (Artioli, 2010).

### **3.3.2 Optical Microscopy (OM)**

Optical microscopy is a technique that allows the acquisition of information about the morphological traits and structure of a sample by magnifying things from x2 to x2000 times with resolutions up to 0.2-0.5  $\mu\text{m}$  depending on the apparatus (Stuart, 2007).

Two types of optical microscopy, namely, stereo zoom and petrographic were used to obtain an accurate description of the samples in general, and the mineralogical composition and morphology in particular (Karkanis, 2007)

The description considered general aspects, such as the color or consistency of the sample (Raith *et al.*, 2011), the nature of the aggregates, their shape, proportion and color, and particular aspects, such as the presence of distinct layers or additives such as ceramics, lime lumps or shells or any other singular observations (Elsen, 2006; Stuart, 2007).

### **3.3.3 Thermogravimetric Analysis (TGA-DTG)**

When a sample is heated at constant rate and in inert atmosphere, it loses mass whenever dehydration, dihydroxylation or decarbonation reactions take place. In contrast, there is a gain in mass when reactions such as oxidation, carbonation or hydration occur (Dang and Kamali-Bernard, 2013).

The thermogravimetric curve (TG) together with the derivative thermogravimetric curve (DTG) allows to plot the representative mass changes within the sample during the heating process, and the peaks will indicate the maximum mass losses due to the characteristic physical or chemical process of the distinct materials in function of temperature (Stuart, 2007; Földvári, 2011).

The mass change within the sampled material is used to make a relative quantification of the carbonate content of the mortars, expressed in percentage of CaCO<sub>3</sub> (w/w), and to estimate the ratios of their composition (Borsoi *et al.*, 2019).

### **3.3.4 X-Ray Diffraction (XRD)**

X-ray Diffraction (XRD) has been widely used in order to study mortars. It is a powerful laboratory technique often used in conjunction with microscopy and chemical analysis during materials characterization investigations of mortars (Middendorf *et al.*, 2005a, Artioli, 2010). Powder X-ray Diffraction can only contribute to a bulk analysis of the carefully homogenized powders. Mainly used for the determination of the mineralogical composition of the mortar, including its aggregate and binder, e.g., quartz in sand, or calcite in sand or carbonated lime binder, or portlandite in binder (Silva *et al.* 2011). The technique has sensitivity, reliability, simple and fast sample preparation, convenient, fast speed, high resolution, easy interpretation of the information that could be utilized for both qualitative and semi-quantitative aspects of analysis (Goffer, 2007).

X-ray diffraction is often used to semi-quantitatively determine the weight fraction of constituents. By comparing the integrated intensities of the diffraction peaks from each of the known phases, their fraction can be identified (Ouhadi and Yong, 2003).

Every mineral phase has its unique diffraction patterns so materials and compounds can be identified by comparing a database of diffraction patterns (Chauhan *et al.* 2014).

### **3.3.5 Variable Pressure Scanning Electron Microscopy coupled with Energy Dispersive X-Ray Spectroscopy VP-SEM-EDS**

Variable Pressure Scanning Electron Microscopy with Energy Dispersive X-ray spectroscopy (VP-SEM-EDS) is the best known and most widely used of the surface analytical techniques. It produces a visual representation of the sample and provides elemental information about the composition of the structure of the surface of a sample at the same time (Goffer 2007; Stuart 2007; Artioli 2010). Energy Dispersive X-Ray Spectroscopy (EDS or EDX) is a chemical microanalysis technique used in conjunction with scanning electron microscopy (SEM), the

imaging portion of the technique and it can show a higher magnification image up to x100,000 times and it is able to plot three-dimensional images with detailed morphological attributes of the material analyzed (Middendorf *et al.*, 2005a; Stuart, 2007).

SEM-EDS can be utilized in order to analyze the mortars' structure and chemical composition through elemental analysis.

It was used as a complementary technique together with Optical Microscopy and XRD analysis. BSE images are useful to study the textural features of the mortars.

### **3.3.6 Acid attack and Granulometric analysis**

Attack was performed in order to investigate the nature and dimension of aggregate grains and the ratio between soluble fraction and insoluble residue present in the mortars assuming that the soluble fraction representing the binder, will be the one composed by carbonates (calcium carbonates and magnesium carbonates), and the aggregates will remain intact after the chemical process in acid.

The resultant insoluble residues are used further on to obtain the grading curve of the aggregates to determine the predominant grain fraction present on each sample, and this, together with the binder to aggregate ratio, will conform an important step for the characterization and reproduction of the historical mortar (Middendorf *et al.*, 2005b).

The results of the Acid attack were used as complementary with the results obtained by XRD and TGA.

## **3.4 ANALYSES EQUIPMENTS AND EXPERIMENTAL CONDITIONS**

### **3.4.1 Stereo microscopy**

A representative part of each mortar sample was selected and then prepared for being analyzed under stereo zoom to obtain general information about the samples, which is an important step helps grouping the studied samples. The size of each sample was the minimum that could guarantee the success of the analysis and the confirmation for future studies, and they were observed carefully to avoid breaking the existing aggregates.

The observations were made by means of a Leica M205 C Stereoscopic Microscope with Zoom: 20.10.5.1, Zoom Range: 7.8x - 160x, Resolution (max): 1050 lp/mm and Visible Structure

Width: 475 nm and recorded with Leica DFC295 digital camera, under controlled experimental conditions in terms of lighting and resolution.

### **3.4.2 Petrographic microscopy**

The petrographic observation of the thin sections was performed on a Leica DM2500 P Modular Polarization Microscope and recorded with a Leica MC170 HD digital camera to identify type, mineralogy, and morphology of the binder, aggregates and any other additives.

The theory of optical microscopy is that the visible light interacts with the specimen by passing through thin sections (of around 30-40  $\mu\text{m}$  thickness) of the specimens (in transmitted-light or polarized-light modes), resulting in a range of color absorptions and pleochroism of the sample through plane-polarized light (PPL), and showing interference colors and birefringence by using cross-polarizers of light (XPL) (Artioli, 2010).

It is also possible to assess their state of alteration and to recognize the presence of neoformed substances and for the study of the interfacial zone, the bonding and possible reaction rims between aggregates and binder at the same sample, or between the mortar and the other building material (bricks or stones). The observation of the presence or absence of microfractures (often related to the hardening process) and the presence or absence of lime nodules (Elsen *et al.*, 2004) are also possible.

### **3.4.3 Thermogravimetric analysis**

For the thermal analysis, Simultaneous Thermal Analyzer STA 449 F3 Jupiter (NETZSCH) was used with silicon carbide furnace RT-1550°C. The quantitative analysis in the selected temperature ranges was performed by using Proteus software. For the analysis, 25-30 mg of the global fraction powder of the samples were placed in platinum crucible into a furnace under inert atmosphere of Nitrogen (Air Liquide Alphagaz compressed  $\text{N}_2$ ) with a flow rate of 70 mL/min. The heating program was set to start at 40°C and then increase it with a uniform heating rate of 10°C/min from 40° to 1000°C.

Then, the results obtained as thermograms represent the changes in samples mass as function of temperature. The results have been analyzed according to the temperature ranges established as criteria by several authors (Bakolas *et al.*, 1998; Genestar *et al.*, 2006; Ingo *et al.*, 2004; Corti *et al.*, 2013) as following: -

- 1) At the first range, (40-120°C), there is a mass loss due to physically adsorbed and hygroscopic water loss occurs.

- 2) At the second range (120-200°C) there is a mass loss of due to crystallization water associated with hydrated salts.
- 3) At the third range (200-600°C), the mass loss is due to chemical bond water (dihydroxylation) in hydraulic compounds (hydrated aluminosilicates, hydrated calcium silicates, etc.) and clays.
- 4) At the fourth range (> 600°C) there is a loss of mass due to the decomposition of carbonates (calcite and dolomite).

In the case of mortars, it is expected to obtain a main weight loss between the range of temperature between 600 - 900°C confirming the decomposition range of calcium carbonate (CaCO<sub>3</sub>) forming calcium oxide (CaO) and carbon dioxide (CO<sub>2</sub>).

Normally, calcium carbonate decomposes between 750°C and 850°C however, the decomposition temperature of calcium carbonate can be lower sometimes depending on the state of crystallization, the presence of salts or organic additives, the granulometry and the atmosphere used for the analysis (Zamudio *et al.*, 2011). When impurities (e.g., clays) or re-carbonated lime are present, decomposition is below 850°C (Corti *et al.*, 2013).

In case of having dolomite, a double peak is recorded on the DTG curve at temperatures 750°C and 850°C (Moropoulou *et al.*, 1995; Paama *et al.*, 1998).

#### **3.4.4 X-ray Diffraction**

X-ray diffractometer BRUKER Discovery using a CuK $\alpha$  source working at 40 kV and 40 mA was used to analyze the powder of the mortar samples in order to obtain the characteristic diffractograms. The DIFFRAC.SUITE EVA software was used to identify the mineral phases together with the (ICDD PDF)-2 database Powder Diffraction Files of the International Centre for Diffraction Data. Diffractograms were obtained at a 2 $\theta$ , scanning between an angular range from 3° to 75° with a velocity of 0.05° per second measuring time by a LYNXEYE linear detector. The analysis approximately took 25 minutes for each sample. For XRD analysis, 1-2 g of powder sample (depending on the density of the sample) were used. Standard polymer sample holders were used to contain the powdered samples.

#### **3.4.5 Variable pressure Scanning Electron Microscopy coupled with Energy Dispersive X-ray Spectroscopy**

Scanning Electron Microscopy coupled with Energy Dispersive X-ray Spectroscopy (SEM-EDS) was used for image acquisition, elemental analysis and elemental mapping. Analysis of

the samples has been performed using a Hitachi S-3700N (Hitachi High Technologies, Berlin, Germany) Scanning Electron Microscope coupled with a Bruker XFlash 5010 (Bruker Corp, Billerica, Mass. USA) with a Silicon Drift Defector (SDD) Energy Dispersive X-ray Spectrometer. The analysis was performed under variable pressure, operated with an accelerating voltage of 20 kV and chamber pressure of 40 Pa. The spectra operated on an energy scale of 0-20 keV, with a resolution of 129 eV at Mn K $\alpha$ , and it was used to obtain the chemical analysis and the EDS elemental data, acquired by point microanalyses in the form of elemental distribution maps with an (ESPRIT compact) Software. For capturing information about the textural features of the samples, SEM images were captured in backscattering electron (BSE) mode.

### **3.4.6 Acid attack and Granulometric analysis**

In order to perform the experiment, first, about 20 g of each sample (if possible) were prepared and crushed using rubber hammer, then separated in two sets (Fig. 3-6a), to confirm the validity of the results, and whether the samples were homogeneous or not.

For this, an hydrochloric acid aqueous solution with a concentration of 1: 3 (v/v) was prepared. All sets were weighted and recorded to compare the initial and the final weights. Then, an amount of 120 mL of the solution was slowly added into a 250 mL beaker containing approximately 10 g of a fragmented sample then left for approximately 10 minutes for releasing the carbon dioxide. After the release of carbon dioxide, the beaker was placed on a hot plate and heated up to boiling temperature and left after boiling for 10 more minutes while stirring (Fig. 3-6c). After cooling down, the mixture was filtered under vacuum using Büchner funnel (Fig. 3-6d) and ST61A009 qualitative filter paper. During this process, the residues were washed twice using distilled water until the hydrochloric acid was eliminated. After the filtration (Fig. 3-6e), they were dried in an oven at 60°C for 24 hours (Fig. 3-6f). The dry insoluble residues were weighed and recorded to compare the initial and the final values for the proportional determination of the soluble fraction to the insoluble residue. The insoluble residues have been sieved through stainless steel test sieves ASTM E11 with a diameter of 100 mm x 40 mm by RETSCH. The sieves used for the analysis had mesh sizes of 4, 2, 1, 0.50, 0.25, 0.125, and 0.063 mm (Fig. 3-6g).

Finally, the insoluble residue obtained by each sieve was weighed and recorded for the granulometric analysis to determine the particle size distributions.



Figure 3.6 Experimentation of the analysis: a) sets of 2 samples, b1,2) HCl aqueous solution and the analyzed sample, c) Heating up the sample in HCl aqueous solution to boiling temperature, d) Filtration under vacuum using a Büchner funnel, e) Filtered wet sample using filter paper, f) samples in the oven to dry, g) Sieving using ASTM E11 test sieves.

## 4 RESULTS

### 4.1 VISUAL INSPECTION

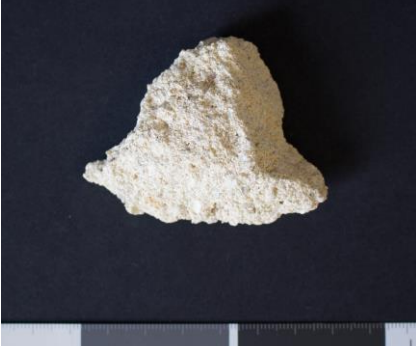
Visual inspection of the samples with an unaided eye, allowed the study of the general features of the selected samples, in order to create an initial assessment of the stratigraphic layers, colors, textures, the existence of lime nodules, cracks, lithic fragments ceramic or any other additives. Evaluation and formulation of preliminary assessments and grouping of samples has been executed based on certain similarities and differences among the samples, considering their macroscopic features allied to their location and function. The studied samples were divided into six groups. (Tab. 4-1). Photographs of representative samples from each group are presented in table 4-2.

Table 4.1 Samples grouping based on the preliminary visual inspection.

<b>Samples Grouping</b>					
<b>Group 1</b>	<b>Group 2</b>	<b>Group 3</b>	<b>Group 4</b>	<b>Group 5</b>	<b>Group 6</b>
Quartz rich samples. Cloaca structure	Chromatic layer.	Ceramic fragments as main aggregates.	Carbonate lithics as main aggregates.	Non-Roman (19 <sup>th</sup> -21 <sup>st</sup> )	Quartz rich with Lime lumps.
CR-1638 - CLO	CR-1129 - A	CR-1706 - M4	CR-915 - G	CR-114 -1	CR-1517- 4
CR-1638 - ESC	CR-1129 - B	CR-1706 - M6	CR-915 - 5	CR-139	CR-1706 - M2
CR-1638 - 9		CR-2204	CR-915 - 6		CR-3007
			CR-915 - 8		CR-3012
			CR-915 - 10		
			CR-915 - 18		
			CR-1131		
			CR-1537		
			CR-1539		
<b>IND<sup>1</sup></b> . CR-1628, MP-132 – AMB 3					

<sup>1</sup>IND. Individual sample

Table 4.2 Photographic documentation of representative samples before disaggregation.

<p>Group 1 CR-1638 ESC</p>	<p>Group 2 CR-1129-B</p>
	
<p>Group 3 CR-2204</p>	<p>Group 4 CR-915G</p>
	
<p>Group 4 CR-1539</p>	<p>Group 5 CR-139</p>
	
<p>Group 6 CR-1517-4</p>	<p>Individual sample CR-1638 ESC</p>
	

## **4.2 OPTICAL MICROSCOPY (OM)**

### **4.2.1 Stereo microscopy**

Preliminary observation of the samples and the examination of the polished surfaces of the cross sections under the stereo microscope provided information regarding the physical characteristics of the binder and aggregates (Tab. 4-4). It showed that the mortars are composed of light and dark colored binders and different types of aggregates, mainly sand, ceramic fragments, lithic fragments and siliceous grains, which vary in size and proportion throughout the samples, table 4-5 shows the results from the visual inspection using the point count of the analyzed area from the sample to obtain a visual based information about the binder to aggregate ratio. Lime lumps with a compact appearance, rounded shape and variable size are also present in the samples.

Samples from group 1 (CR-1638CLO, CR-1638ESC and CR-1638-9), which are floor filler and render mortars were collected from the cloaca structure. From the microscopic observation, it has been confirmed that samples from this group contain almost over 60% of siliceous materials as aggregates in addition to the presence of lithics and shells.

Group 2 (CR-1129A and CR-1129B) includes the samples with a greenish blue chromatic layer on the surface, and a mortar layer of a light whitish color with sub-angular and poorly rounded siliceous aggregates. The samples of this group have preparation layer (from 0.5 to 2 mm), with carbonate aggregates and shells.

Group 3 (CR-2204, CR-1706M4 and CR-1706M6) is characterized by the presence of coarse angular crushed ceramic fragments, with various sizes and different hues of orange, red and brown.

Group 4 (CR-915G, CR-915-5, CR-915-6, CR-915-8, CR-915-10, CR-915-18, CR-1131, CR-1537 and CR-1539) includes samples with aggregates of irregular shape and dimensions, which appear to be lithic fragments with a very small amount of binder. Sample CR-915-5 displays a distinctive binder composition dividing the sample in two parts: the first half is darker whereas the other half of the sample shows the same matrix but lighter in color (Tab. 4-3).

Group 5 samples (CR-139 and CR-114), correspond to mortars that were added to the Cryptoporticus later. They were added to the building later during the interventions in the 19<sup>th</sup> and 21<sup>st</sup> centuries and they are characterized by the presence of lime lumps and coal fragments.

Group 6 (CR-1517-4, CR-1706M2, CR-3007 and CR-3012), characterized by samples with noticeable presence of lime lumps, and high amount of quartz as the main aggregates.

Finally, there is an individual sample (CR-1628-MP132-AMB3), IND, that cannot be included in any of the previous groups. It's a thin layer of a dark mortar applied to a piece of marble and its grains have a metallic luster. Its thickness, shape, regularity and color of the grains suggests its application with a decorative purpose.

The samples are relatively compact and present a medium to high mechanical strength to the action of the rubber hammer during the disaggregation, with the exception of sample CR-1517 and CR-3012. Cracks in the binder and between the ceramic aggregates and the binder had been identified in most of the samples (Tab. 4-3b-b). Lime lumps (Tab. 4-3e), charcoal particles (Tab. 4-3f), shells (Tab. 4-3d), zoning surrounding the stone fragments, zoning surrounding the ceramics (noticeable due to lighter or darker color than the overall composition of the fragment) were spotted in the samples (Tab. 4-3b-c).

Table 4.3 Particularities of representative samples observed under stereo microscope.

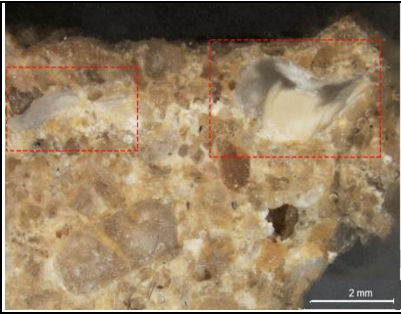
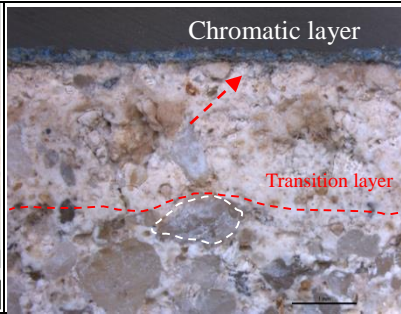
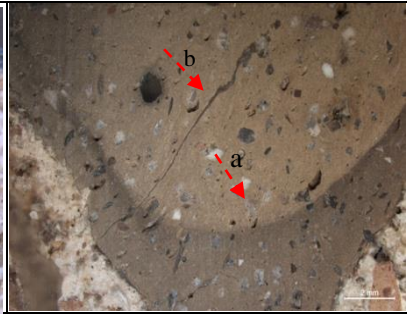
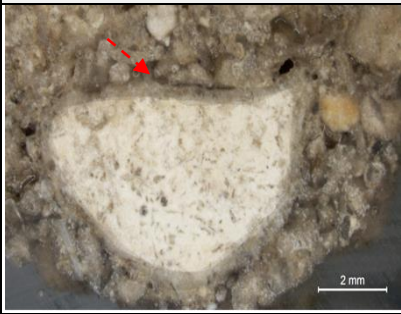
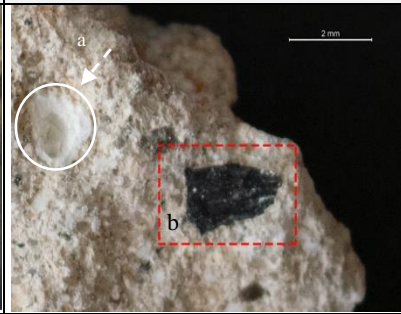
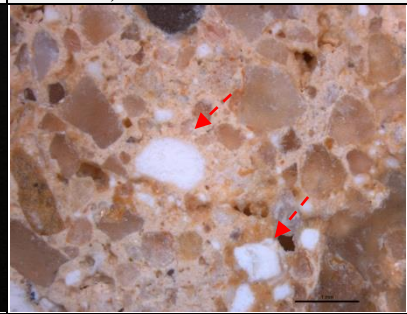
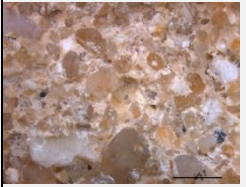
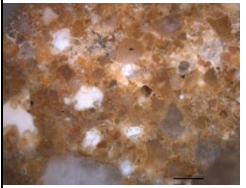
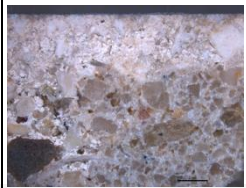
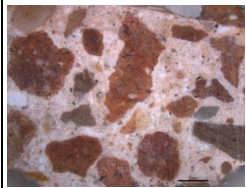
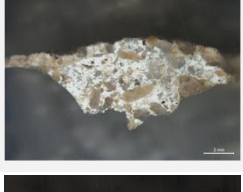
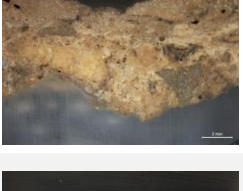
		
<p><b>a) G1- CR-1638-9</b> Shells</p>	<p><b>d) G2-CR-1129B</b> Chromatic layer</p>	<p><b>b) G3-CR-2204</b> a) Zonings in ceramic b) Cracks in ceramic</p>
		
<p><b>c) G4-CR-1131</b> Zoning in lithic aggregates</p>	<p><b>f) G5- CR-139</b> a) Lime lump b) Coal fragment</p>	<p><b>e) G6- CR-1706M4</b> Lime lumps</p>

Table 4.4 Identification and description of the samples by microscopic observations (stereo zoom microscope) of cross sections.

Groups	Sample	Structure	Thickness (cm)	Color	Strength integrity	Description	Cross section
1	CR-1638, CLO	Floor (EU-16)	1-2	Light pink	Fairly rigid	Rounded and sub-rounded sand with shells and visible lime lumps	
	CR-1638, ESC	Floor (EU-16)	2	Light beige	Fairly rigid	Sand with shells and visible lime lumps	
	CR-1638-9	Floor (EU-16)	2	Light beige	Fairly rigid	Aggregates sub-angular and angular, around 1-2 mm. with shells and visible lime lumps and sporadic fragments of stones	
2	CR-1129A	Wall (EU-11)	3	white	Rigid	Sand with varying sizes and sporadic fragments of stones and shells. Has chromatic layer over its surface.	
	CR-1129B	Wall (EU-11)	2	Light beige (Close to white)	Rigid	Aggregates sub-angular and angular, around 1-2 mm. large nodules of lime lump up to 5 mm. Presence of a quartzite fragments. Has chromatic layer over its surface.	
3	CR-1706-M4	Wall (EU-17)	1-2	Light pink	Rigid	Ceramic fragments with sporadic pieces of coal and lime lumps	
	CR-1706-M6	Wall (EU-17)	1-2	Light pink	Rigid	Ceramic fragments, sand and sporadic pieces of lime nodules and coal in the matrix	
	CR-2204	Wall (EU-22)	4	Light pink	Rigid	Various sizes of ceramic fragments with small amount of lime lumps in the matrix	

4	<b>CR-915G</b>	Wall (EU-9)	1-2	Light beige	Fairly rigid	Fragments of huge and flaky stones, (terracotta) with low amount of yellowish binder.	
	<b>CR-915-5</b>	Floor (EU-9)	2	Beige and light beige	Rigid	Fragments of huge, sharp edged and flaky stones, terracotta with very low amount of yellowish binder.	
	<b>CR-915-6</b>	Floor (EU-9)	1.5	Light beige	Fairly rigid	Visible pieces of broken stones, visible lime nodules, shells, with yellowish binder.	
	<b>CR-915-8</b>	Floor (EU-9)	2	Light beige	Rigid	Fragments of huge and flaky stones, poorly rounded sand with a low amount of binder.	
	<b>CR-915-10</b>	Floor (EU-9)	1-2	Light beige (Close to white)	Fairly rigid	Sand with angular and sub-angular fragments of flaky stones in a white binder.	
	<b>CR-915-18</b>	Floor (EU-9)	1-2	Light beige	Fairly rigid	Fragments of huge and flaky stones with sand and visible lime lumps in light binder	
	<b>CR-1131</b>	Floor (EU-11)	1-2	Beige tends to gray	Rigid	Aggregates sub-angular and angular, around 1 mm. Presence of large lithic fragments (15-20 mm). with very low amount of binder	
	<b>CR-1537</b>	Floor (EU-15)	1-2	Light yellow	rigid	Aggregates sub-angular and angular, around 1 mm. Presence of large lithic fragments (15-20 mm). with very low amount of binder	
	<b>CR-1539 "Gato"</b>	Floor (EU-15)	1-2	Beige	Fairly rigid	Fragments of huge angular aggregates of lithic fragments with low amount of binder	

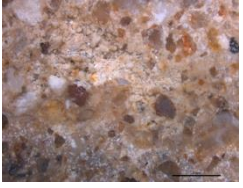
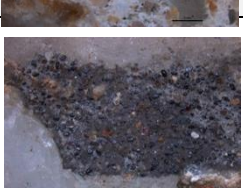
	<b>CR-114</b>	Wall (EU-1)	1-2	Light pink	Fairly rigid	Aggregates of sub-angular and angular, homogeneous with visible inclusions of lime lumps and sporadic fragments of stone, ceramics and charcoal pieces.	
	<b>CR-139</b>	Wall (EU-1)	2	Very light beige (Close to white)	Fairly rigid	Sand of varying particle sizes, with visible lime lumps, Charcoal fragments with huge fragments of stones.	
<b>6</b>	<b>CR-1517-4</b>	Floor (EU-15)	3	Light pink	Crumbly	Aggregates sub-angular and angular (some around 2 mm). Has a light binder color. Nodules of lime lumps around 1 mm in diameter.	
	<b>CR-1706-M2</b>	Wall (EU-17)	3	Light pink	Rigid	Aggregates sub-angular and rounded, around 1-2 mm. and quartz with visible pieces of lime nodules in the matrix	
	<b>CR-3007</b>	Floor (EU-30)	2	Light brown	Rigid	Aggregates sub-angular and angular, around 1-2 mm., fragments of stone with visible lime lumps	
	<b>CR-3012'</b>	Floor (EU-30)	2	Light yellow (Close to white)	Crumbly	Aggregates sub-angular and angular, around 1-2 mm. with sporadic pieces of coal, larger pebbles and visible lime lumps	
<b>IND.</b>	<b>CR-1628, MP132-AMB 3</b>	Unknown (EU-16)	< 3	Dark grey	Rigid	Well-rounded particles of quartz and heavy dark minerals	

Table 4.5 Results obtained from the microscopic observations of the cross sections of the samples.

Groups	Sample	Binder		Aggregates							
		Type	Color	Quartz			Lithics		Ceramic		Shells
				Size (mm)	Area (%)	Roundness	Size mm	Area (%)	Size (mm)	Area (%)	
1	CR-1638, CLO	lime	Whitish	0.5-3	60	Subangular-poorly rounded	0.5-2	5	-	-	√
	CR-1638, ESC	lime	Whitish	0.5-3	60	Subangular-poorly rounded	1-3	10	-	-	√
	CR-1638-9	lime	Whitish	0.5-3	60	Subangular-poorly rounded	1-3	10	-	-	√
2	CR-1129A	lime	Whitish	0.5-2	60	Poorly rounded	0.5-2	5	-	-	√
	CR-1129B	lime	Whitish	0.5-2	60	Poorly rounded	0.5-2	5	-	-	√
3	CR-1706-4	lime	Pinkish	0.5-1	10	Subangular-poorly rounded	-	-	1-10	50	-
	CR-1706-6	lime	Pinkish	0.5-1	10	Poorly rounded	-	-	0.5-8	50	-
	CR-2204	lime	Pinkish	0.5-1	10	Poorly rounded	-	-	2-20	60	-
4	CR-915G	lime	Greyish	0.5-2	10	Subangular-poorly rounded	1-6	70	-	-	√
	CR-915-5	lime	Greyish	0.5-1	15	Subangular-poorly rounded	1-5	60	-	-	√
	CR-915-6	lime	Greyish	0.5-3	10	Subangular-poorly rounded	1-5	65	-	-	√
	CR-915-8	lime	Greyish	0.5-2	10	Subangular-poorly rounded	1-5	60	-	-	√
	CR-915-10	lime	Greyish	0.5-2	20	Subangular-poorly rounded	1-5	50	-	-	√
	CR-915-18	lime	Greyish	0.5-2	10	Subangular-poorly rounded	1-5	50	-	-	√
	CR-1537	lime	whitish	0.5-1	15	Subangular-poorly rounded	1-6	50	-	-	√
	CR-1539 "Gato"	lime	whitish	0.5-1	10	Subangular-poorly rounded	1-6	60	-	-	√
	CR-1131	lime	Greyish	0.5-1	10	Subangular-poorly rounded	1-6	50	-	-	√
5	CR-114	lime	Pinkish	0.5-1	60	Subangular-poorly rounded	1-2	5	0.5-1	5	-
	CR-139	lime	Whitish	0.5-1	55	Subangular-poorly rounded	1-3	10	-	-	-
6	CR-1517-4	lime	Pinkish	0.5-3	60	Poorly rounded	-	-	-	-	-
	CR-1517-4	lime	Pinkish	0.5-3	60	Poorly rounded	-	-	-	-	-
	CR-3007	lime	Brownish	0.5-2	40	Subangular-poorly rounded	0.5-1	10	0.5-1	3	-
	CR-3012'	lime	Whitish	0.5-3	50	Poorly rounded	0.5-2	5	-	-	-

The samples that contain ceramic fragments as the main aggregates are all functioning as render mortars. Group 3, additionally to samples CR-114-1 (Group 5) and CR-3007 (Group 6), are the only samples contain ceramics among the 24 samples. Three types of ceramics brown (B), Orange (C), and reddish brown (D), were distinguished and classified by their composition, color, size, porosity and inclusions (Tab. 4-6). The frequency of the different types of ceramic fragments within the mortar was recorded (Tab. 4-7), and it was possible to determine that type C is present in higher amount. Types B, C and D in sample CR-2204 are encountered mainly as big fragments, with a size range vary from 10 to 30 mm, while all types of ceramic aggregates in the rest of the samples were found as small fragments < 10 mm. In sample CR-3007 and CR-114, the ceramic fragments were not the main aggregates unlike samples from group 3, and they have mainly ceramic fragments type C but in small proportions (Fig. 4-1).

Table 4.6 Types of ceramics fragments found in samples.

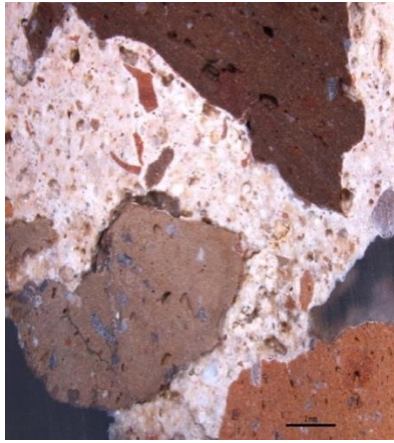
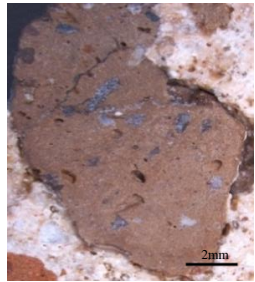
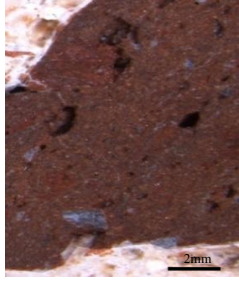
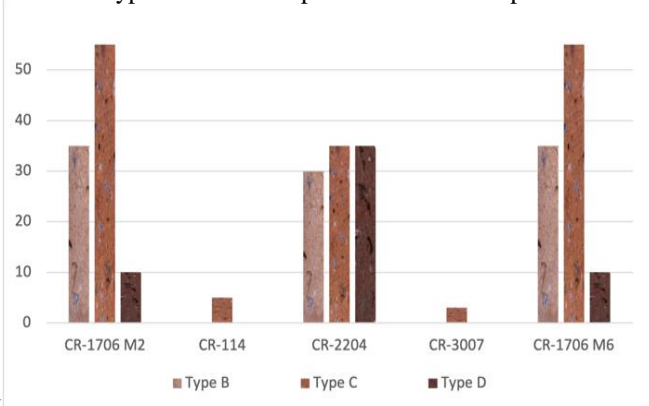
	Type B Brown	Type C Orange	Type D Reddish brown
			
	High percentage of big and small siliceous inclusions with random grains, poorly sorted. Light color. Compact.	Compact composition, random siliceous inclusions in a fine clay matrix. Light color, well sorted.	Compact composition, small ratio of siliceous inclusions in a fine clay matrix. Deep color, poorly sorted.

Table 4.7 Visual estimated distribution of ceramic fragment types found in samples

Sample	Type B Brown	Type C Orange	Type D Reddish brown
CR-1706 M2	++	++++	+
CR-114	-	+	-
CR-2204	++	+++	+++
CR-3007	-	+	-
CR-1706 M6	++	+++	+

Most frequent    ++++    +++    ++    +    Least frequent

Figure 4.1 Visual estimate percentage (in volume) of the different types of ceramics present in each sample



### 4.2.2 Petrographic analysis

By means of petrography, aggregates can be recognized and identified (Barker, 2014). It has been used to understand the spatial distribution of components including the structure and texture of mortars by means of thin sections and to understand the bonding, the kind of binder, and as well as the use of additives and admixtures within the mortar (Middendorf *et al.* 2005a). The petrographic analysis allowed confirming the previously performed grouping.

All samples have been analyzed by means of petrographic microscopy (Tab. 4-8, 4-9). Samples from group 1 are characterized by the presence of quartz and feldspar, in addition to a noticeable presence of shells only in sample CR-1368-9.

As for the samples from group 2 with chromatic layer, it is easy to distinguish between the greenish blue chromatic layer and the preparation layer, which is characterized by the presence of carbonated lithics and some shells, and the mortar layer, with mainly quartz aggregate with a high degree of cohesion and homogeneity.

Samples of group 3 characterized by the presence of ceramic fragments with inclusions of micas, feldspars and amphiboles, that can also be seen within the binder. Ceramic aggregates appear under the microscope as irregularly shaped pieces of various sizes sometimes exhibiting color zoning on the rims.

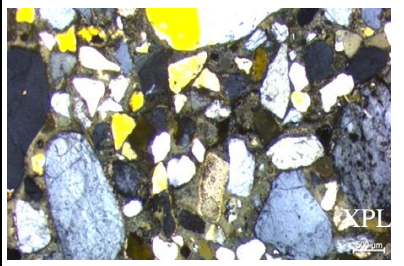
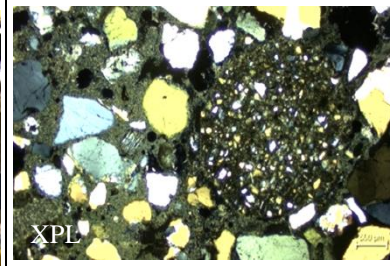
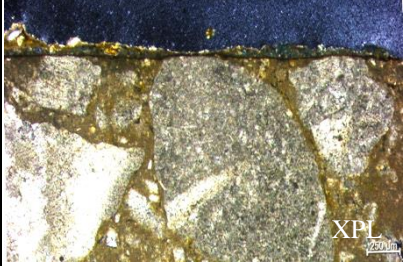
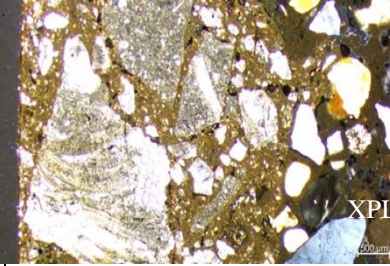
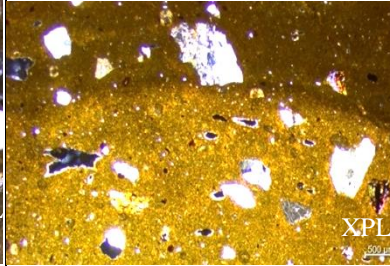
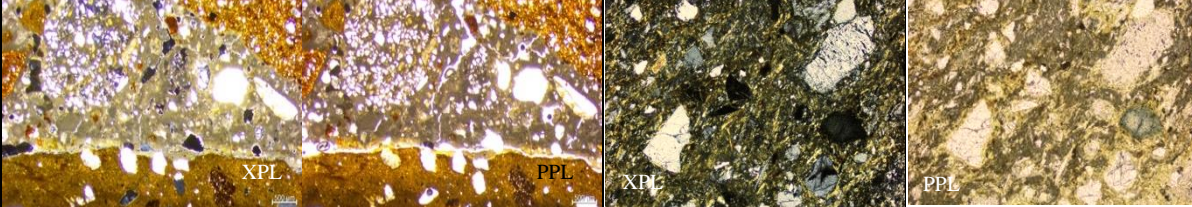
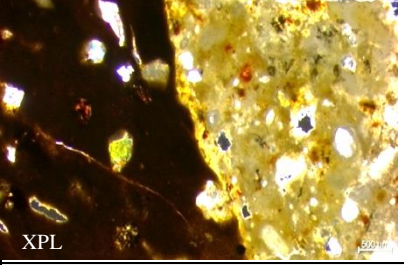
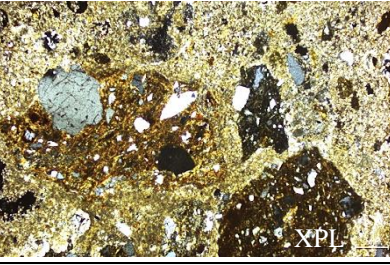
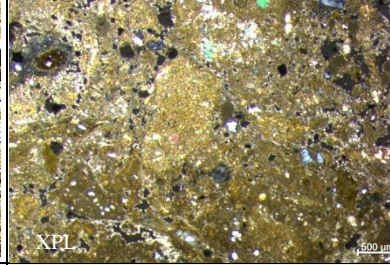
Going to group 4, samples are characterized by the presence of angular, sub-angular and limestone and sandstone fragments. The optical similarity between limestone and binder made it difficult to distinguish between the binder and carbonated aggregates.

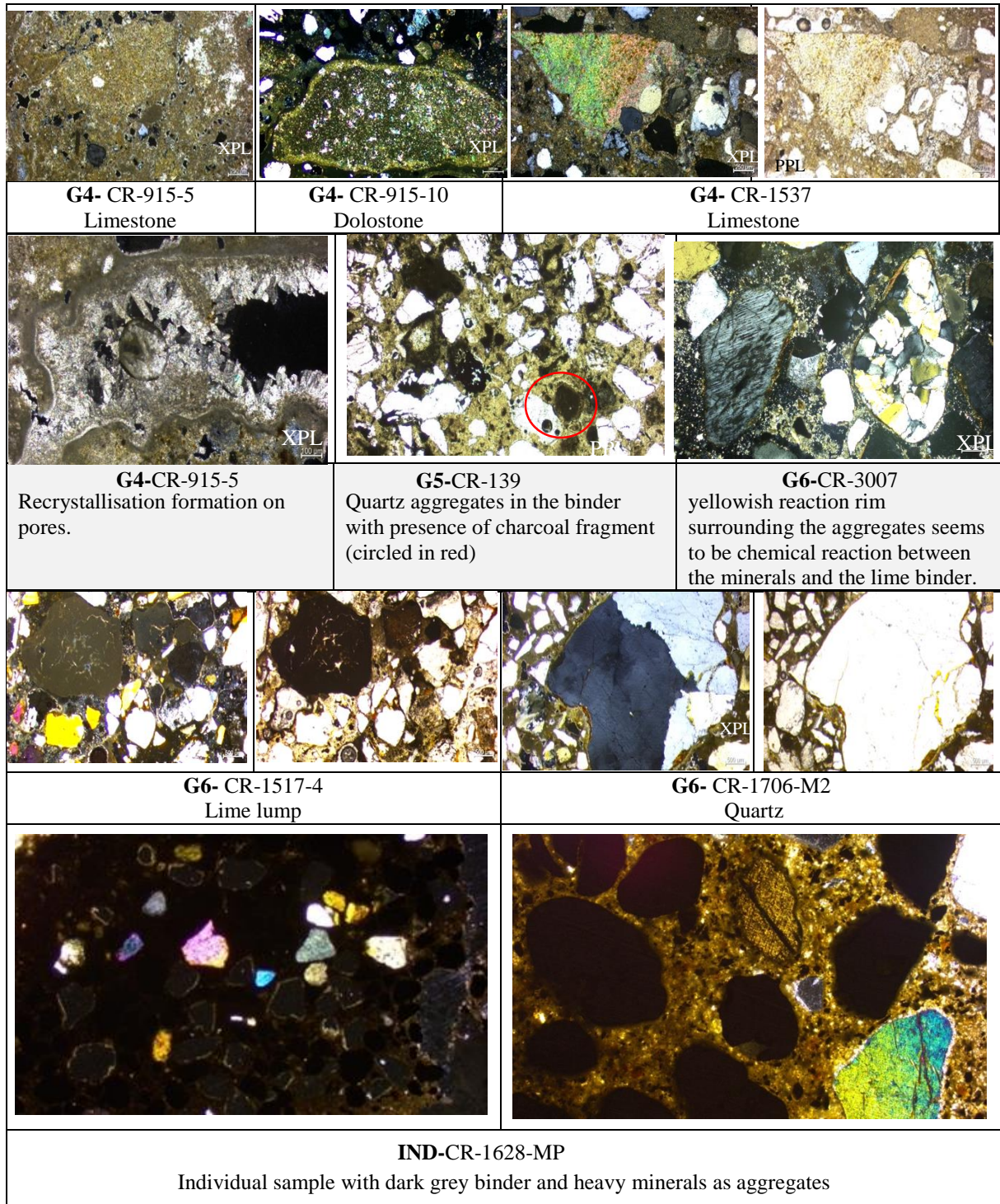
Samples from group 5, added during 19<sup>th</sup> and 21<sup>st</sup> century, are somewhat similar in composition to the Roman samples from group 1, with notable presence of lime lumps and charcoal fragments as well as a small proportion of ceramic fragments.

The group 6 samples, they are characterized by the high presence of large lime lumps compared to the rest of the samples.

Finally, the individual sample appears to have colored heavy minerals as aggregates with luster, homogeneity and roundness, and the binder is darker (dark grey) compared with the rest of the samples.

Table 4.8 Petrographic features representative of defined groups. XPL (cross polarized light) and PPL (plane-polarized light).

		
<p><b>G1- CR-1638-9</b> General distribution, angular and sub-angular quartz aggregates. Predominance of quartz. Some feldspars, shells and lithics (quartzite).</p>	<p><b>G1- CR-1638-9</b> Quartz rich sample with feldspar and noticeable presence of shells.</p>	<p><b>G1-CR-1639-CLO</b> Lime rich binder, Predominance of quartz, sandstone, and quartzite with presence of feldspars. Small angular and sub-angular shape.</p>
		
<p><b>G2-CR-1129-A</b> Painting layer (top), preparation layer mainly from limestones, shell fragments and lime lumps in lime binder (bottom).</p>	<p><b>G2-CR-1129-A</b> Painting layer (left), preparation layer (middle) and the mortar layer (left).</p>	<p><b>G3-CR-2204</b> Zoning in ceramic most probably related to difference in firing temperature. The outer part was in contact with higher temperature.</p>
		
<p><b>G3- CR-1706-M6</b> Ceramic fragment</p>		
		
<p><b>G3-CR-1706-M4</b> Transition between layers (with reaction rim). The binder (right) and ceramics (left). Amphiboles, micas and plagioclases present.</p>	<p><b>G3-CR-1706-M6</b> General distribution. Quartz and ceramic aggregates. Presence of some amphiboles, micas and feldspars.</p>	<p><b>G4-CR-915-8</b> General distribution of lithic fragments (limestone and sandstones) in lime binder with Presence of quartz, micas and feldspars.</p>



### 4.3 THERMOGRAVIMETRIC ANALYSIS (TGA-DTG)

Thermogravimetric analysis was carried out on the global fraction (GF) powders of the samples to identify and determine the binder amount by measuring the percentage of the mass changes throughout the heating process in an inert atmosphere. The temperature ranges were set as 40-120°C, 120-200°C, 200-600°C and 600-900°C, where weight loss occurred. The mass losses at

each temperature range were calculated from the thermogravimetric curve (TG) and are shown in table 4-10.

The mass losses that occur at low temperatures (<120°C) are due to the physically absorbed water (Moropoulou *et al.*, 1995a, b; Bakolas *et al.*, 1998; Elsen *et al.* 2010; Silva *et al.*, 2011), and in the studied samples it varied between 0.02% (CR-1368ESC) and 0.71% (CR-1539).

The mass loss at 120-200°C is attributed to the loss of the crystallized water of hydrated salts. The mass losses in this second range differed between 0.01% (CR-1706M6 and CR-139) and 1.36% (CR-1539),

The mass loss at 200-600°C can be related to chemically bonded water (dihydroxylation) of clay minerals and hydraulic compounds (Elsen *et al.* 2010, Borsoi *et al.* 2019). In this third range the mass losses differed between 0.5% (CR-915G) and 4.2% (CR-1539 and CR-1638CLO).

The most significant mass variation occurs in the temperature range of 600-900°C and corresponds to the loss of carbon dioxide (CO<sub>2</sub>) as consequence of the decomposition of calcium carbonate (CaCO<sub>3</sub>) into calcium oxide (CaO) and carbon dioxide (CO<sub>2</sub>) [Eq. 4] and thus enables the determination of the CaCO<sub>3</sub> content within the sample [Eq. 5] (b; Bakolas *et al.*, 1998; Elsen *et al.*, 2010; Silva *et al.*, 2011, Borsoi *et al.* 2019). In this range the mass losses varying between 2.8% (CR-114) and 38.4 % (CR-1539)



$$\text{CaCO}_3 (\%) = \text{P}(\text{CO}_2) \cdot \text{M}(\text{CaCO}_3) / \text{M} (\text{CO}_2) \quad [5]$$

in which:

P (CO<sub>2</sub>) represents the mass loss (%) in the temperature range 600-900°C.

M(CaCO<sub>3</sub>) is the molar mass of calcium carbonate (100.082 gmol<sup>-1</sup>).

M (CO<sub>2</sub>) the molar mass of carbon dioxide (44.02 gmol<sup>-1</sup>).

The TGA/DTG curves for the samples of group 1, which were acquired from the cloaca structure are shown in Fig. 4-2. In the temperature range 600-900°C the mortars from this group (CR-1638CLO, CE-1638-9 and CR-1938ESC) lost 15.0%, 10.3% and 9.10%, respectively. The comparison of the TG/DTG curves of the mortar samples among each other allowed to detect

their compositional similarities. The thermograms of the samples from group 1 showed a clear similarity by having very low carbonate composition comparing with most of the rest roman samples (except for samples from group 6).

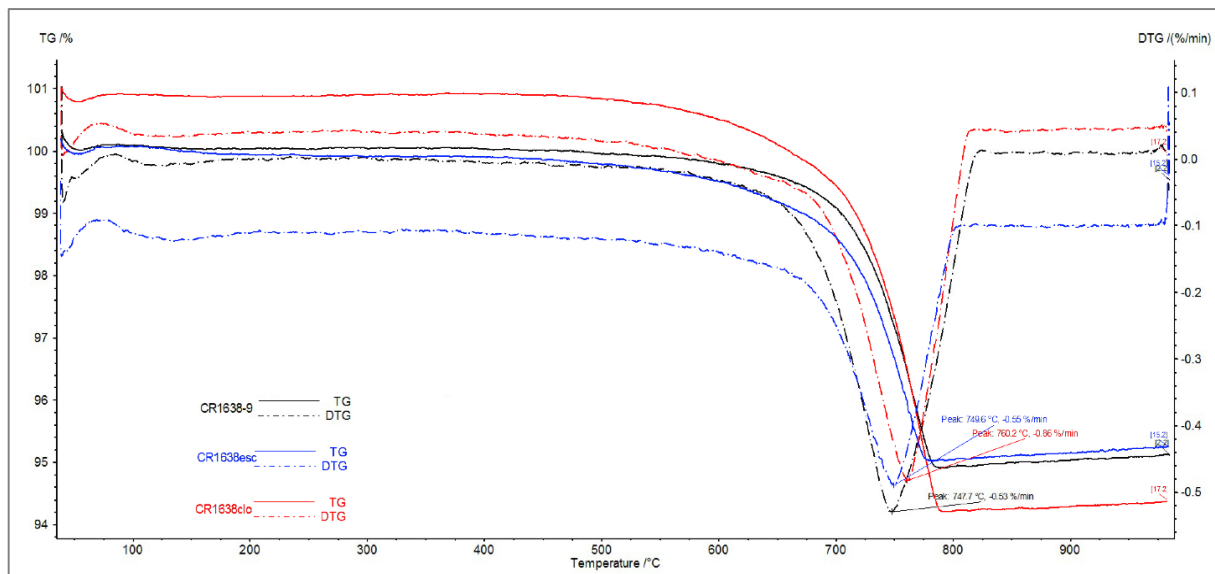


Figure 4.2 . TG/DTG curves of samples from group 1, CR1638-ESC (blue), CR1638-9 (black), CR1638-CLO (red), continuous curves representing TG and dashed curve representing DTG data.

The TG/DTG curves of samples from group 2 (CR-1129-A and CR-1129-B) are shown in Fig. 4-3. Both samples had their significant mass losses within the range 600-900°C due to the decomposition of calcium carbonate ( $\text{CaCO}_3$ ). The samples present a calcium carbonate content of 25.9% and 23.6%, respectively.

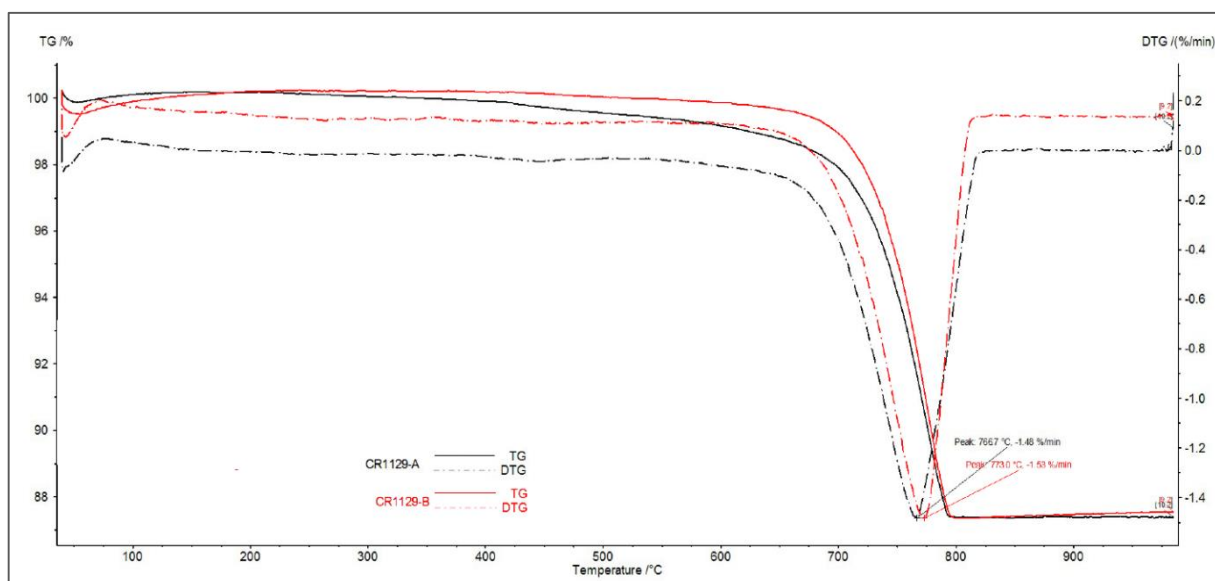


Figure 4.3 TG/DTG curves of samples from group 2, CR-1129-A (black), CR-1129-B (red), continuous curves representing TG and dashed curve representing DTG data.

The TG/DTG curves for samples of group 3 (CR-1706-M4, CR-1706-M6 and CR-2204)) are shown in Fig. 4-4. The curves obtained have a typical trend for the hydraulic mortars (according to Branda *et al.* 2001). The curves show an initial loss of weight due to hygroscopic water below 200 °C, where a net jump at 120–200 °C due to crystallized water loss of this phase is present in TGA curves of these samples. The samples had their significant mass losses within the range 600-900°C due to the decomposition of the carbonated components (Fig. 4-4). The samples present a calcium carbonate content of 35.0%, 25.4% and 30.5%, respectively.

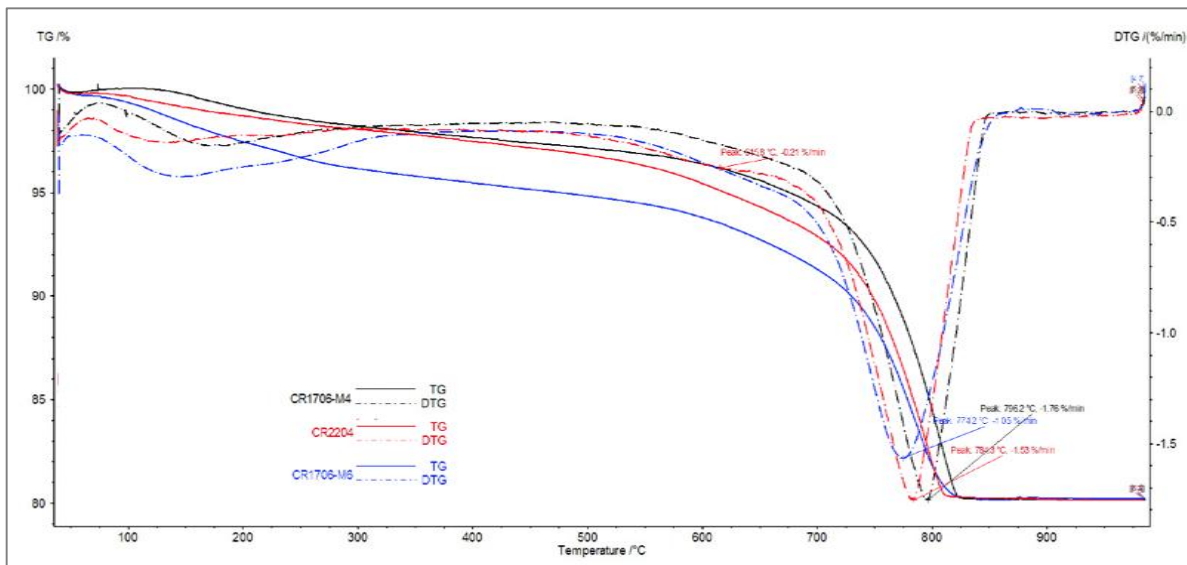
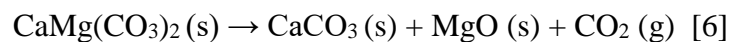


Figure 4.4 TG/DTG curves of samples from group 3, CR1706-M6 (blue), CR1706-M4 (black), CR-2204 (red), continuous curves representing TG and dashed curve representing DTG data.

The TG/DTG curves for samples of group 4 are shown in Fig. 4-5. All mortar samples of this group presented mass losses only in the range at 600-900°C, which is attributed to the decomposition of calcium carbonate. The calcium carbonate content ranges from 25.6 % (CR-915-10) to 81.9 (CR-915-15). The DTG curves exhibits a shoulder at 750°C, a temperature values indicative of the presence of dolomite. The dolomite decomposition occurs according to equation [6] and is followed by equation [4]. Whilst equation [4] represents the decomposition of calcium carbonate (CaCO<sub>3</sub>) and occurs at the last measured temperature range that is set at 650-900°C.



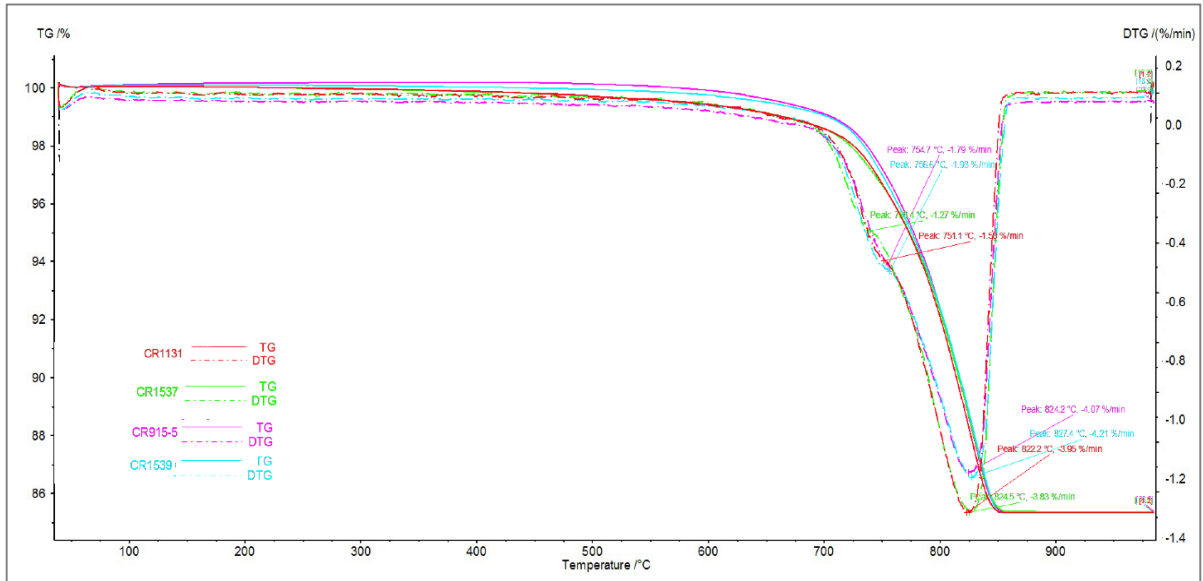


Figure 4.5 TG/DTG curves of samples from group 4, CR915-5 (purple), CR1537 (green), CR1131 (red), continuous curves representing TG and dashed curve representing DTG data.

The TG/DTG curves for samples of group 5 are shown in figure 4-6. The two samples (CR-114 and CR-139), represent two samples of modern mortar that were added to the building in the 19<sup>th</sup> and 21<sup>st</sup> century. These two samples are characterized by the loss of water between 40-200°C, in addition to the decomposition the carbonates, which showed a lower temperature (around 550 °C) compared to the rest of the roman samples. CR-139 and CR-114 samples present a calcium carbonate content of 12.4% and 6.4%, respectively.

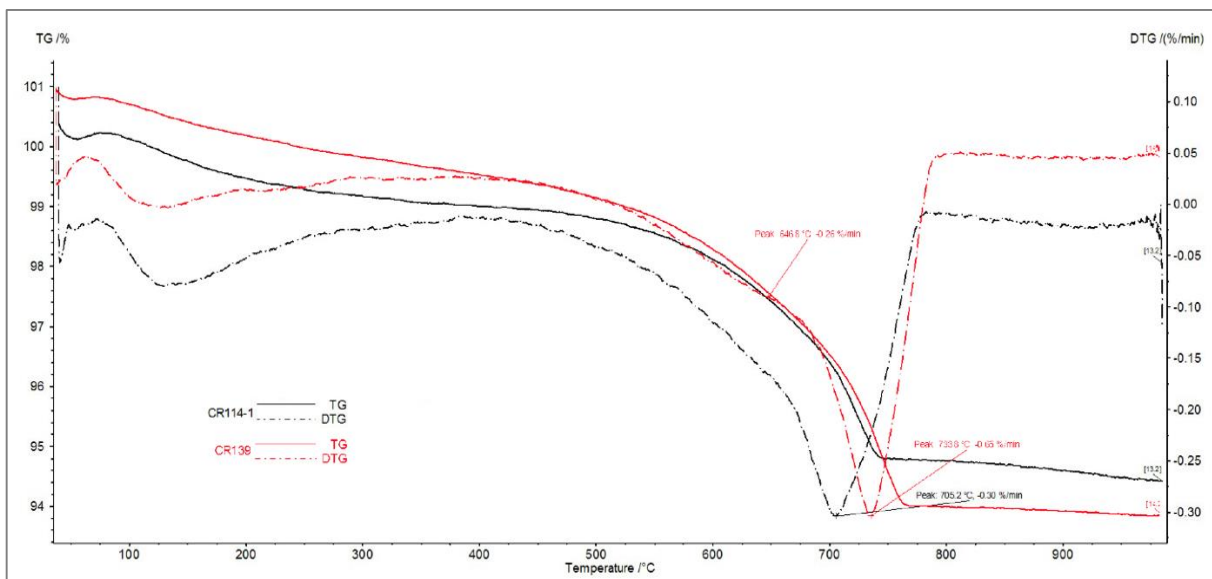


Figure 4.6 TG/DTG curves of samples from group 5 (recent samples), CR114 (black), CR139 (red), continuous curves representing TG and dashed curve representing DTG data.

The TG/DTG curves for samples of Group 6 are shown in figure 4-7. The curves show an initial loss of weight due to hygroscopic and crystallization water below 200 °C. The samples had significant mass losses within the range 600-900C due to the decomposition of the carbonated components (Fig. 4-7). Samples CR-1517-4, CR-1706-M2, CR-3007 and CR-3012 present a calcium carbonate content of 13.9, 14.6, 7.1 and 26.7% respectively.

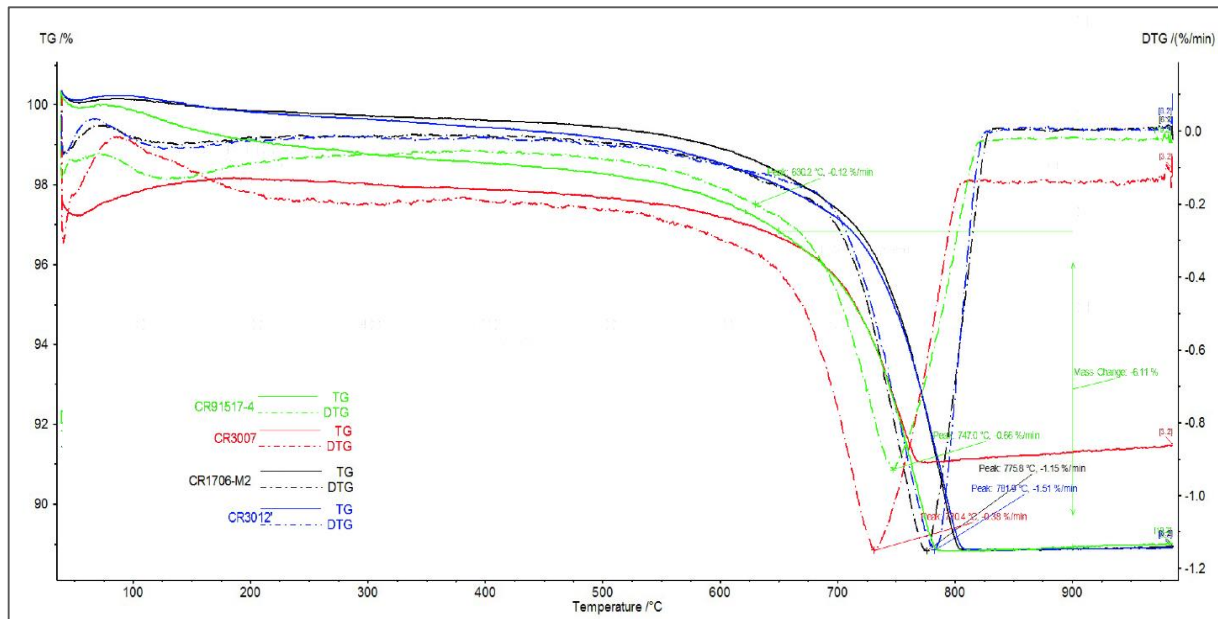


Figure 4.7 TG/DTG curves of samples from group 6, CR915-5 (purple), CR1537 (green), CR1131 (red) and CR-1706-M2 (black) continuous curves representing TG and dashed curve representing DTG data.

The similarities between the thermograms of samples within the same group are evident and related to the fact that these samples were collected from the same architectural unit from different structures and have similar mineralogical composition, as already proposed from the petrographic analysis.

The calculated percentage of the mass loss due to the decomposition of calcium carbonate recorded by thermograms in the temperature range between 600-900°C (Appx. 6), with maximum percentage of 81.9% (CR-915G) from Group 4, and a minimum of 6.4% (CR-114) from group 5 (Tab. 4-9) (Fig.4-8).

Table 4.9 Sample mass losses, calcium carbonate contents (%) and binder to aggregate ratio obtained by TGA.

Groups	Sample	Mass losses (%)		CaCO <sub>3</sub> %	Binder: Aggregate
		200-600°C	600-900°C		
1	CR-1638-9	2.2	4.6	10.3	-
	CR-1638-ESC	2.4	4.0	9.1	1:9
	CR-1638-CLO	4.2	6.6	15.0	1:6
2	CR-1129-A	1.8	11.4	25.9	1:3
	CR-1129-B	0.6	10.4	23.6	1:3
3	CR-1706-M4	2.4	15.4	35.0	1:2
	CR-1706-M6	1.6	11.2	25.4	1:3
	CR-2204	3.5	13.4	30.5	1:2
4	CR-915-G	0.5	27.5	62.4	-
	CR-915-5	1.4	36.0	81.9	-
	CR-915-6	2.2	32.5	73.9	-
	CR-915-8	2.2	18.1	41.2	-
	CR-915-10	1.6	11.3	25.6	-
	CR-915-18	0.9	17.1	28.8	-
	CR-1131	0.8	33.7	76.7	-
	CR-1537	2.1	34.3	78.0	-
5	CR-114	0.9	2.8	6.4	1:14
	CR-139	1.6	5.5	12.4	-
6	CR-1517-4	4.1	6.1	13.9	-
	CR-1706-M2	2.3	6.4	14.6	-
	CR-3007	1.4	3.1	7.1	-
	CR-3012	1.6	11.8	26.7	-

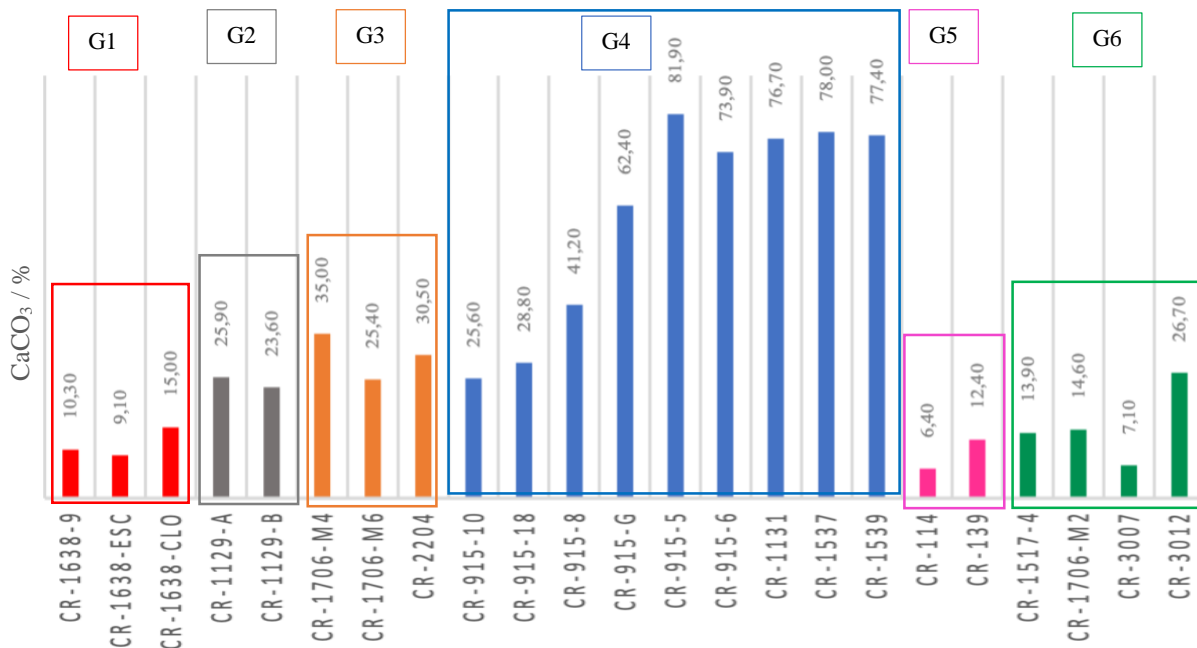


Figure 4.8 Calculated percentage of CaCO<sub>3</sub> in the samples from TGA results.

#### 4.4 X-RAY DIFFRACTION (XRD)

X-ray diffraction (XRD) analysis was carried out on the global fraction (GF) powders of the mortar samples to identify their mineralogical composition (Appx. 7). The XRD patterns of the different sample groups are present in Fig. 4-9 to 4-14. In Tab. 4-10 are presented the qualitative and semi quantitative mineralogical composition of the mortars. The XRD results show that the predominant mineral phase is quartz, which is present in all samples. Along with the quartz, all samples show an abundance in K-feldspar (orthoclase and microcline). Plagioclase feldspars and micas were also obtained from powder XRD analysis in the global fraction of the sample, although in relatively lower amounts. Calcite was identified with other minor or trace minerals phases encountered in the samples like hematite (CR-915-8, CR-1704-M4 and CR-1706-M6) and kaolinite in samples (CR-915G and CR-1537).

The results obtained from XRD analysis are in accordance with the results from petrographic analysis and stereo-zoom observation, indicating the division of the samples into six main groups according to the crystalline phases present. Calcite was identified as the predominant component in samples from Group 4 (CR-915-5, CR-915-6, CR-1131, CR-1537, CR-1539).

The analysis of the global fractions of the group 1 samples demonstrated high presence of quartz and the presence of illite and/or muscovite, kaolinite as trace minerals have been detected within the samples from this group (Fig. 4-9).

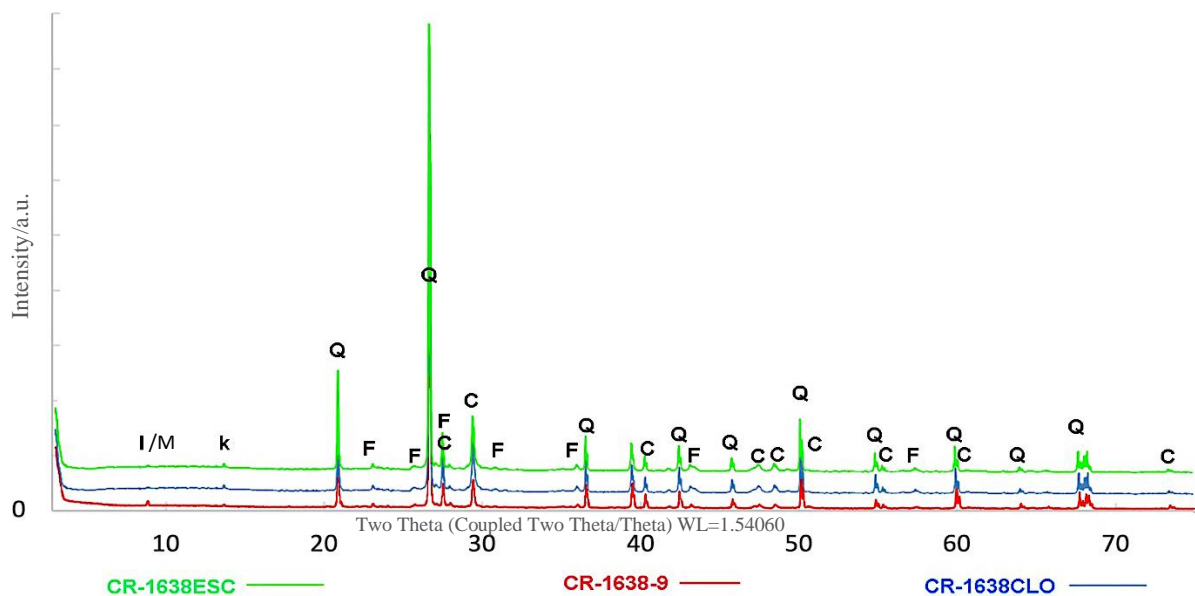


Figure 4.9 Representative XRD pattern of GF from group 1 samples, (Q: quartz, C: calcite, F: feldspar, I/M: illite or muscovite, k: kaolinite).

Samples of group 2 demonstrated high proportions of quartz compared with the other minerals, confirming the results from the petrography that showed high presence of well sorted, sub rounded quartz aggregate (Fig. 4-10).

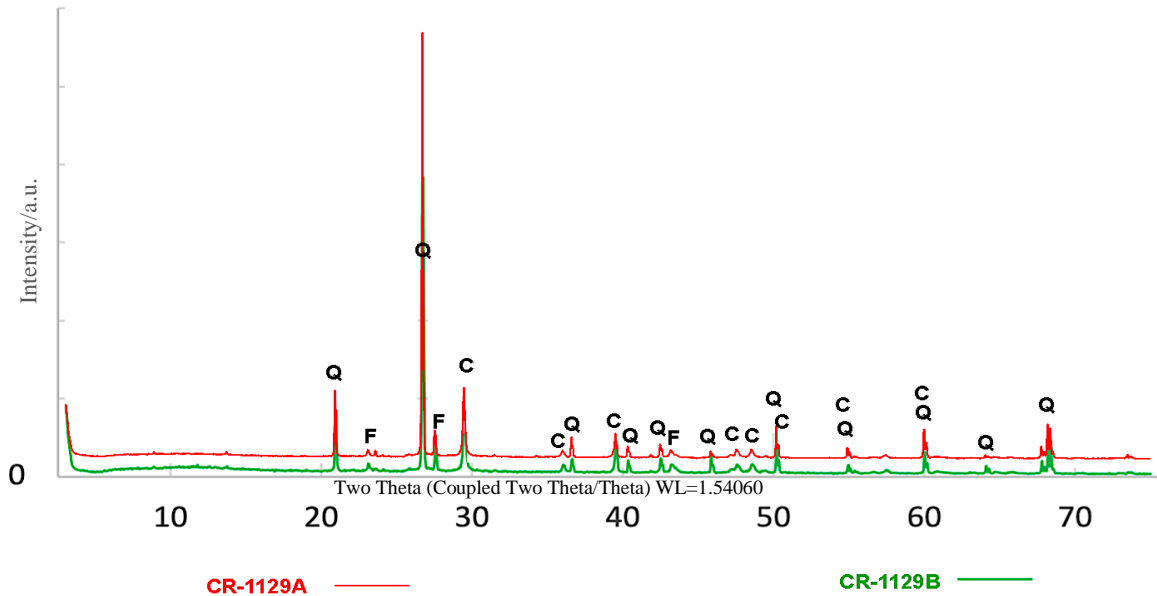


Figure 4.10 Representative XRD pattern of GF from group 2 samples, (Q: quartz, C: calcite, F: feldspar).

The results from XRD for group 3, the ceramic-rich samples (CR-1706M4, CR-1706M6 and CR-2204) demonstrate predominance of quartz and calcite. Additionally, the presence of illite and/or mica (muscovite and/or biotite), amphibole and hematite both as trace minerals (Fig. 4-11).

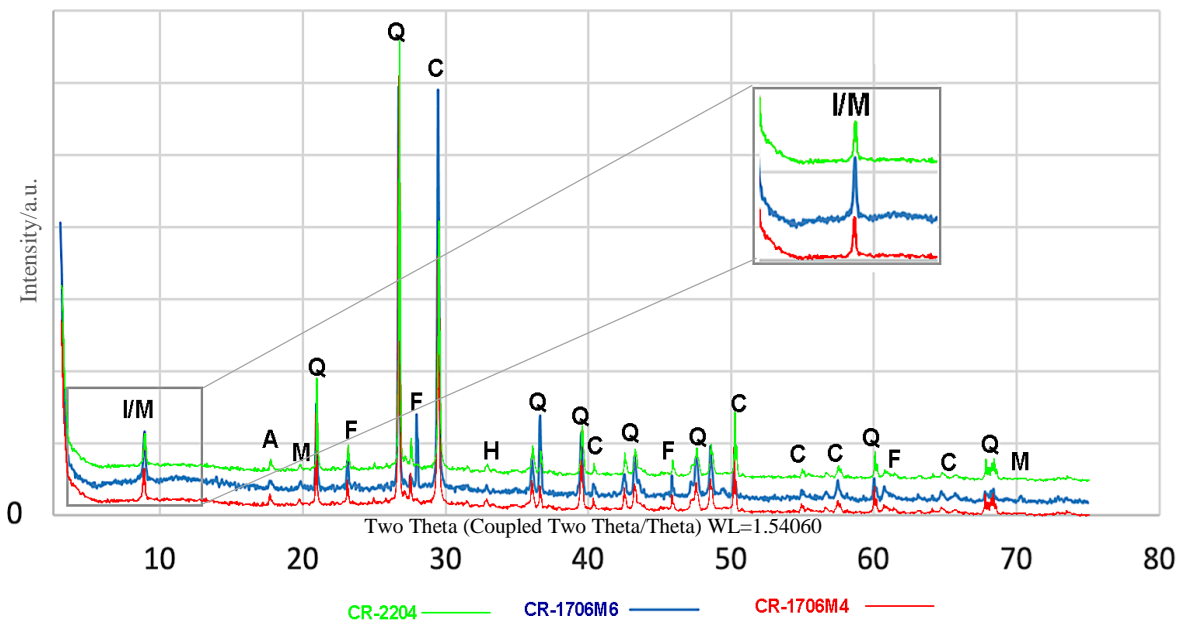


Figure 4.11 Representative XRD pattern of GF from group 3 samples, (Q: quartz, C: calcite, F: feldspar, Ilt/M: illite or muscovite, H: hematite A: amphibolite).

For group 4, dolomite is presented in all samples of group 4, samples (CR-915G, CR-915-5, CR-916-6, CR-1131, CR-1537, CR-1539) contain dolomite in high proportions; whilst samples (CR-915-8, CR-916-10 and CR-915-18) contain low amount of dolomite, confirming the results from TGA). Amphibole and illite/muscovite also presented as trace minerals (Fig. 4-12).

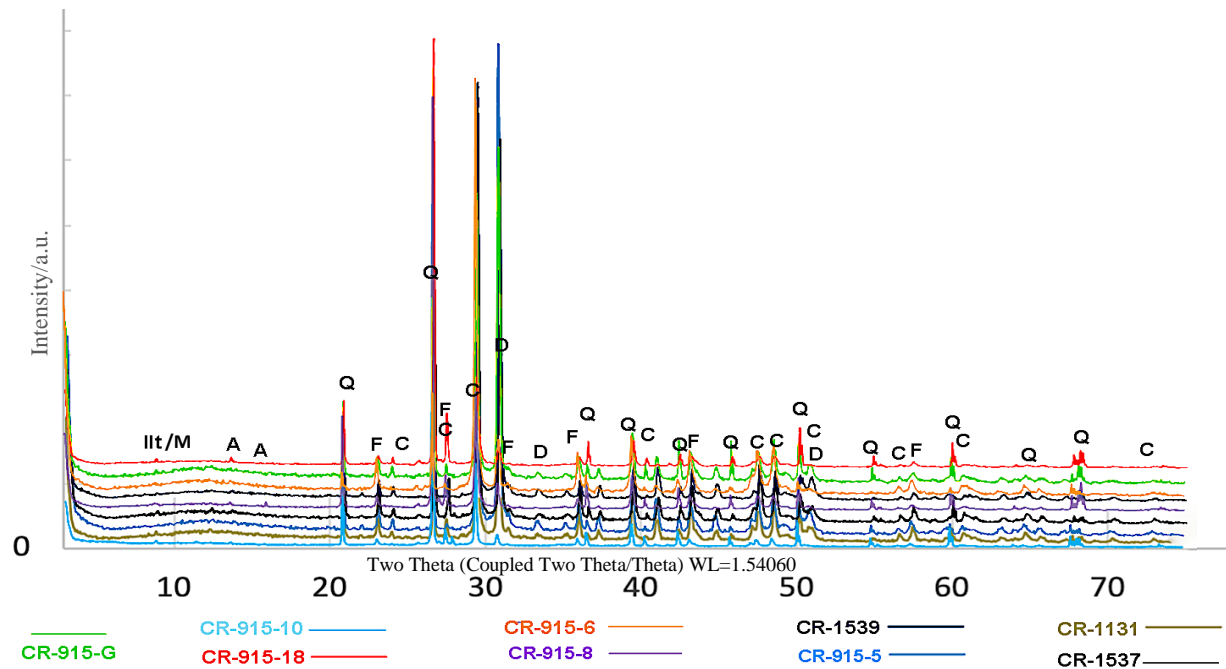


Figure 4.12 Representative XRD pattern of GF from group 4 samples, (Q: quartz, C: calcite, F: feldspar, Ilt: illite, A: amphibole, D: dolomite).

Samples of group 3 demonstrated high proportions of quartz followed by calcite and feldspars. Hematite was also present as trace mineral (Fig. 4-13).

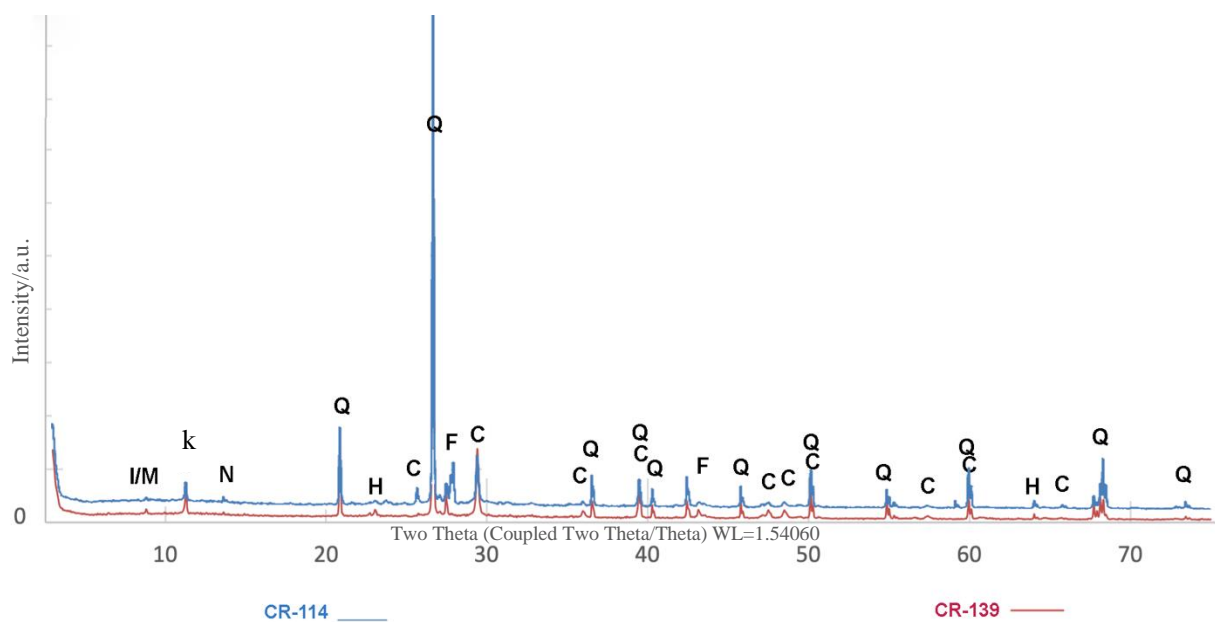


Figure 4.13 Representative XRD pattern of GF from group 5 samples, (Q: quartz, C: calcite, F: feldspar, Ilt/M: illite or muscovite, H: hematite, k: kaolinite).

Samples of group 6 demonstrated high presence of quartz, followed by calcite and feldspars. Muscovite and kaolinite were also present as trace minerals (Fig. 4-14).

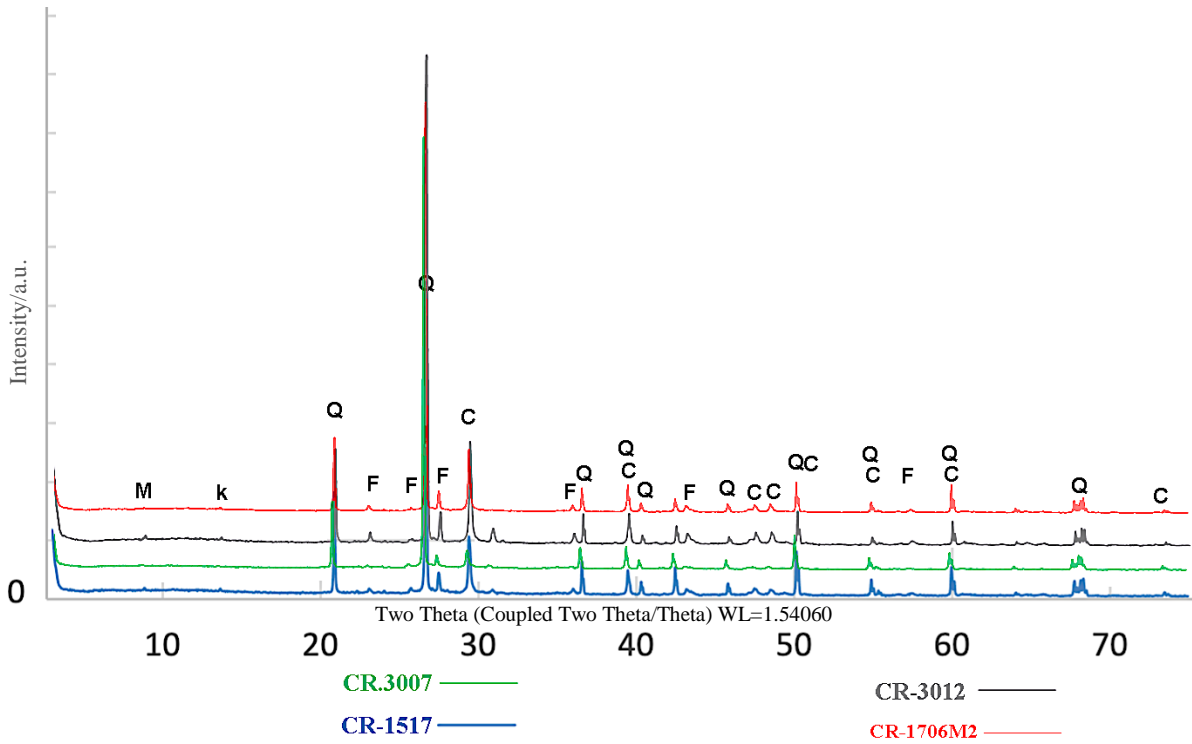


Figure 4.14 Representative XRD pattern of GF from group 6 samples, (Q: quartz, C: calcite, F: feldspar, M: muscovite).

Table 4.10 The mineralogical composition and predominance of the mortars (XRD analysis)

Groups	Name	Fraction	Quartz	Calcite	Dolomite	Feldspars		Mica	Kaolinite	Amphibolite	Hematite	Illite
						Plagioclase	K					
1	CR-1638CLO	GF	++++	+	-	+	++	-	-	-	-	TR
	CR-1638ESC	GF	++++	+	-	-	++	-	-	-	-	TR
	CR-1638-9	GF	++++	+	-	-	++	+	-	-	-	TR
2	CR-1129A	GF	++++	++	-	-	++	-	-	-	-	-
	CR-1129B	GF	++++	++	-	-	++	-	-	-	-	-
3	CR-1706-M4	GF	++++	+++	-	++	+	+++	-	TR	TR	TR
	CR-1706-M6	GF	+++	+++	-	+	++	++	-	TR	TR	TR
	CR-2204	GF	++++	+++	-	-	+	++	-	TR	-	TR
4	CR-915G	GF	+++	++	++	-	+	-	TR	-	-	TR
	CR-915-5	GF	++	+++	++	-	+	-	TR	-	-	TR
	CR-915-6	GF	++	++++	++	-	+	-	-	-	-	TR
	CR-915-8	GF	++++	++	+	-	++	-	-	-	TR	TR
	CR-915-10	GF	++++	++	+	+	++	+	-	-	-	TR
	CR-915-18	GF	+++	++	+	-	++++	+	-	-	-	TR
	CR-1131	GF	++	+++	++	+	++	+	+	-	-	TR
	CR-1537	GF	++	+++	+++	+	+	+	TR	-	-	TR
	CR-1539 "Gato"	GF	++	+++	+++	-	++	-	-	-	-	TR
5	CR-114	GF	++++	+	-	++	++	-	-	+	TR	TR
	CR-139	GF	++++	++	-	-	++	+	-	+	TR	TR
6	CR-1517-4	GF	++++	+	-	-	+	-	-	-	-	-
	CR-1706-M2	GF	++++	++	-	-	++	-	-	-	-	-
	CR-3007	GF	++++	+	-	-	+	-	-	-	-	-
	CR-3012'	GF	++++	++	+	-	++	+	-	-	-	-

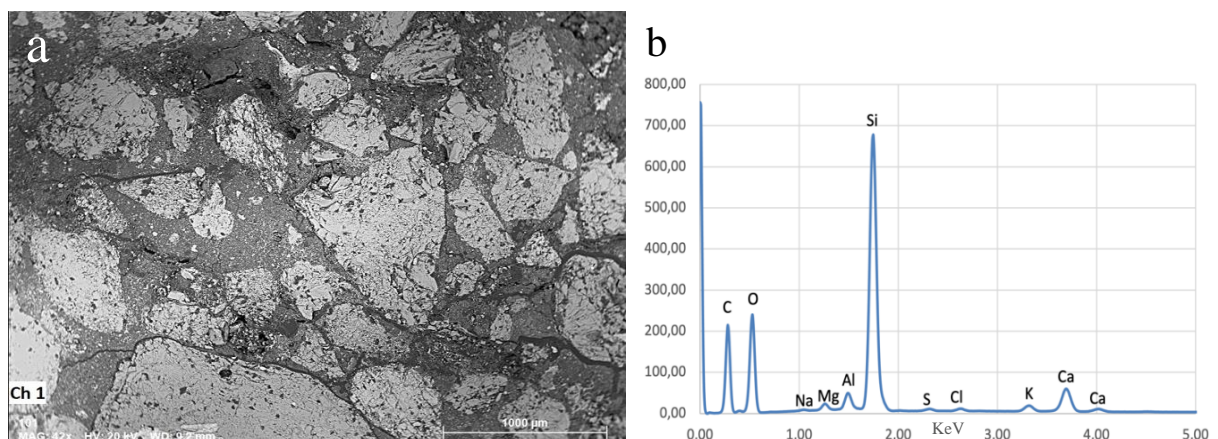
++++ Predominant, +++ abundant, ++ major, + minor, TR- trace

#### 4.5 VARIABLE PRESSURE SCANNING ELECTRON MICROSCOPY COUPLED WITH ENERGY DISPERSIVE X-RAY SPECTROSCOPY (VP-SEM-EDS)

Scanning electron microscopy with an energy-dispersive X-ray spectroscopy was used to provide chemical data that allow the determination of the chemical compositions and textural characteristics regarding both aggregates and binder on mortars from the roman Cryptoporticus of Lisbon. Both, polished surfaces and thin sections were used for the analysis to obtain the elemental mappings and the point analysis.

Eight samples have been analyzed: CR-1638-9 (group 1), CR-1129B (group 2), CR-1706-M4 (group 3), CR-1131 and CR-915-5 (group 4), CR-139 (group 5), CR-1706-M2 (group 6), and CR-1628-MP-123 (IND). In all samples, the mineralogy of the binder and the aggregates differs significantly. The presence of quartz, feldspars and micas as aggregates, was confirmed in all samples in different amounts corroborating the result obtained by XRD and the observations carried out by optical microscopy.

The elemental maps of sample CR-1638-9 (group 1) are shown in fig. 4-15. The presence of quartz aggregates has been confirmed by the high predominance of silicon (Si). From micas, muscovite was detected from the association of silicon, aluminum (Al) and potassium (K), biotite was also detected with the addition of iron (Fe). Feldspars were identified from the association of silicon and aluminum together with either potassium forming potassium feldspars or sodium (Na) forming plagioclases. The morphology of the aggregates as previously determined by optical microscopy, is sub-angular to angular.



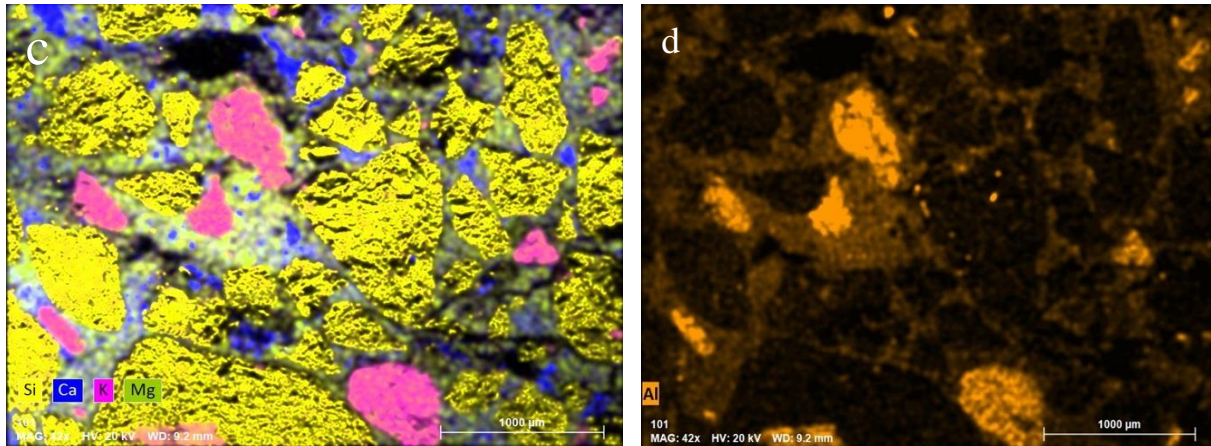


Figure 4.15 Elemental maps of sample CR-1638-9; a) BSE image of the general composition, b) EDS spectra of the map c) Si, Ca, K, Mg elemental map, K related to feldspars d) Al elemental map, Al related to micas and feldspars.

In the binder, calcium has been detected as the main element, its content predominates over all other elements content. It concentrates around the aggregates and fills the interstices (in the form of calcite recrystallization), while incorporation of magnesium, aluminum and silicon was also detected in the binder matrix. (Fig. 4-16).

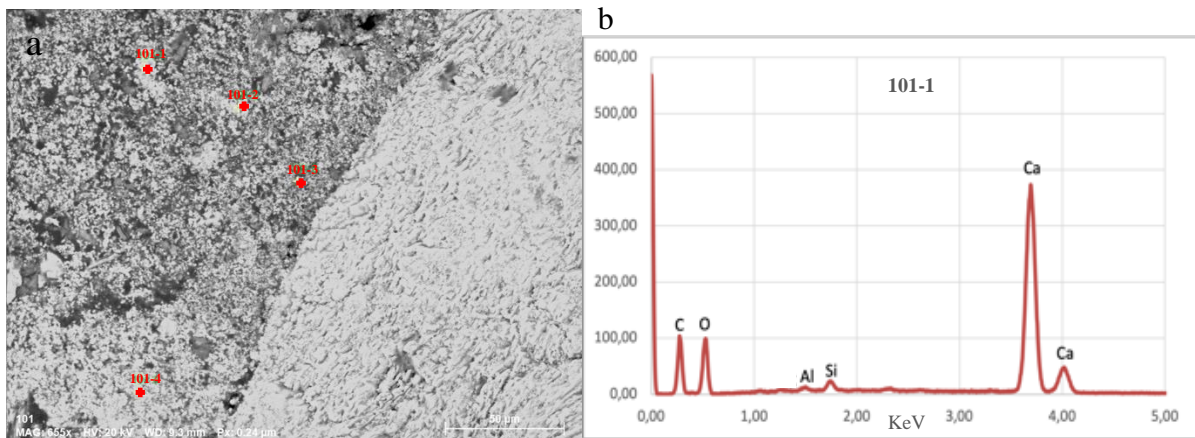


Figure 4.16 a) Point analysis of the binder of CR-1638-9, b) EDS spectrum of the point analysis marked in (a).

Group 2, sample CR-1129-B, with a chromatic layer was observed to analyze the mortar, the preparatory layer between the paint and mortar surface as well as the pigment composition. The samples have a greenish blue chromatic layer with a thick preparatory layer beneath the chromatic layer ranges from 3 to 5 mm, with high amount of calcium, either as binder or as aggregates, as shown in figure 4-17.

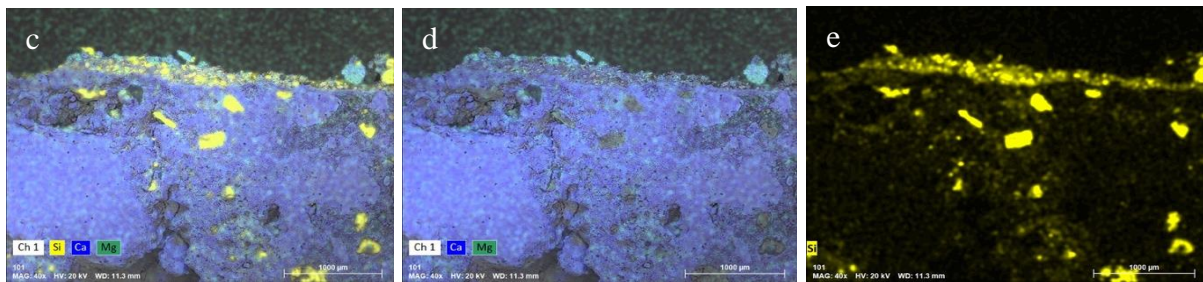
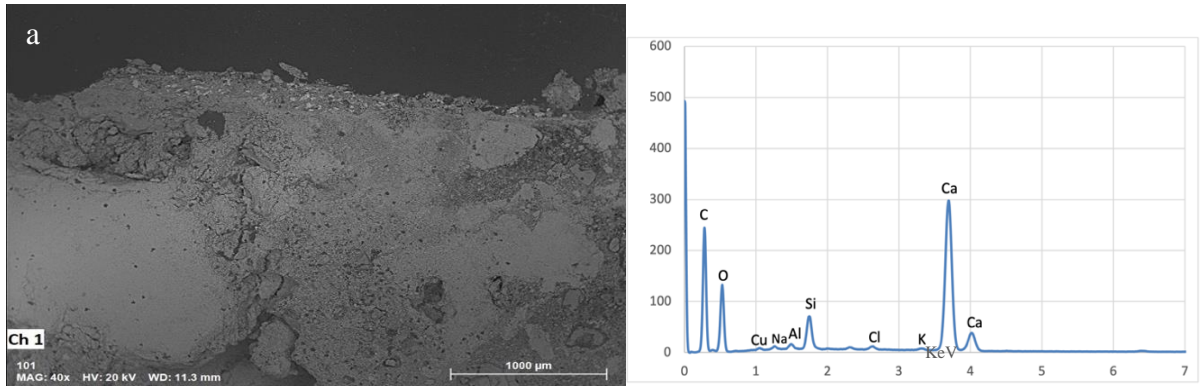


Figure 4.17 a) BSE image on a preparatory and pigment layer of sample CR-1129B, b) EDS spectra of the map c) Si related to Ca and Mg, d) relation between Ca and Mg, e) Si elemental map. yellow=Si, blue=Ca, green=Mg.

The area analysis of the greenish blue chromatic layer (Fig-4.18) showed presence of Cu in association with other elements such as Si, Al, Ca, O, C, Na, K, Mg, Cl and Fe as trace element. The elemental map of Cu overlaps with Si and O without any other element, suggesting a copper silicate.

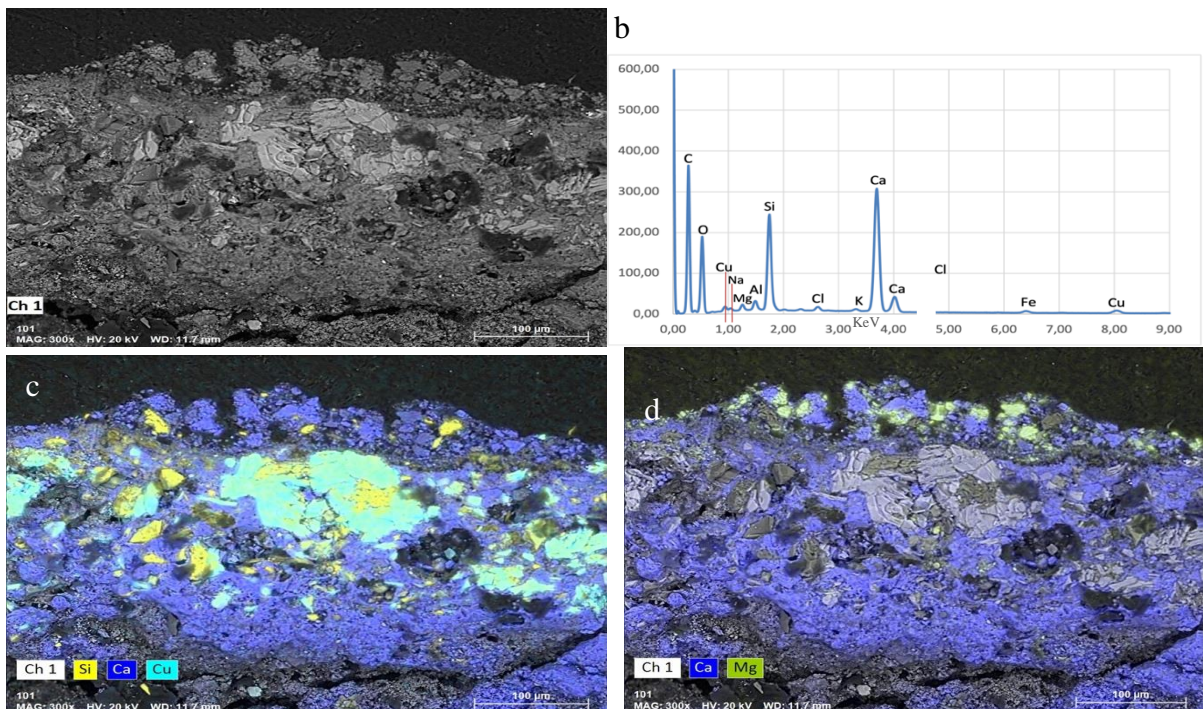


Figure 4.18 a) BSE image on the pigment layer of sample CR-1129B, b) EDS spectra of the map c) Si related to Ca and Cu, d) relation between Ca and Mg. yellow=Si, blue=Ca, cyan=Cu.

The aggregates in the mortar layer are corresponding mainly to quartz and occasionally to lithics and feldspars. Abundance of calcium in the binder region suggest the use of lime binder (Fig 4-19,20)

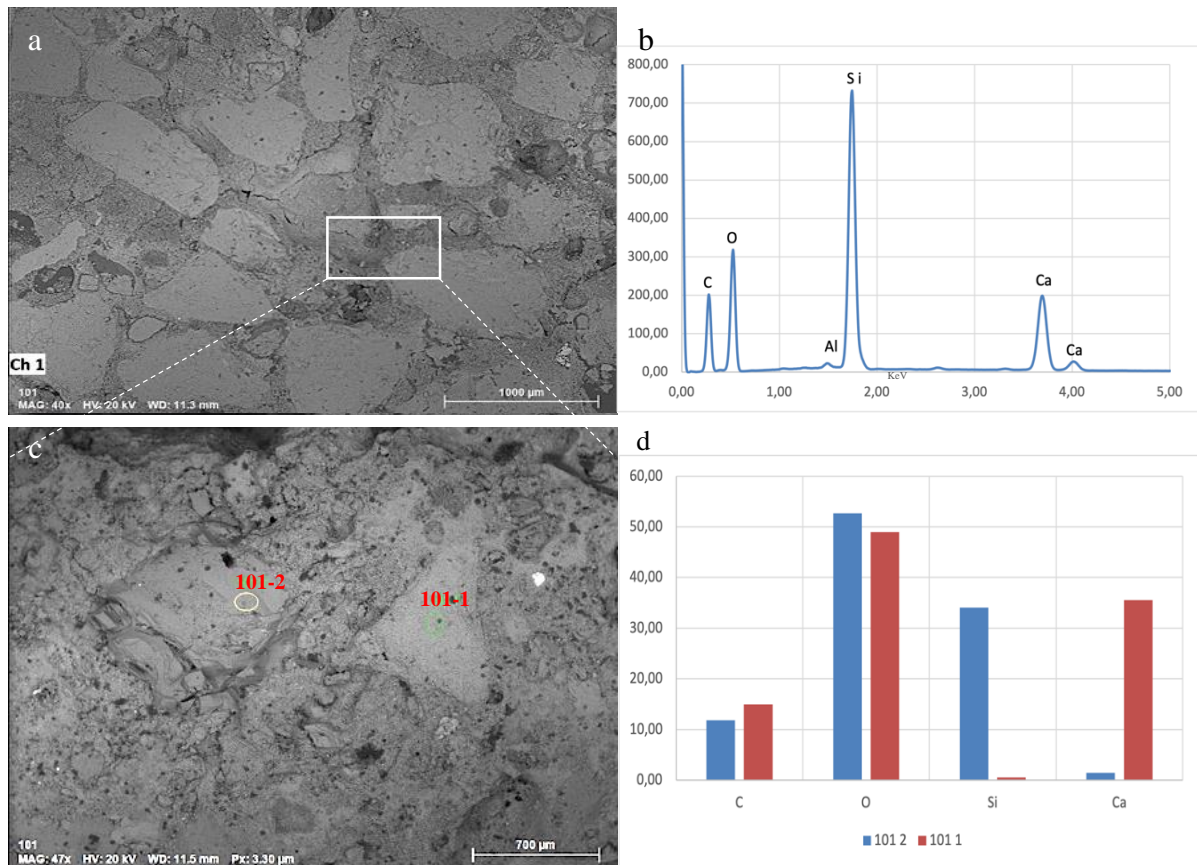


Figure 4.19 a) BSE image on the mortar layer of sample CR-1129B, b) EDS spectra of the map c) point analysis of different aggregates.

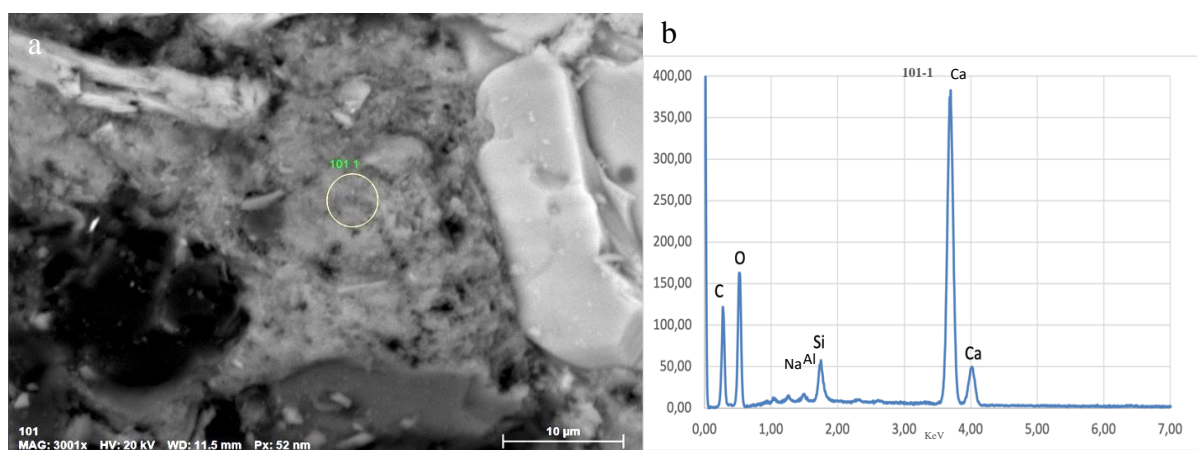


Figure 4.20 a) BSE image on the binder of sample CR-1129B, b) EDS spectra of the binder.

All samples from group 3 (presence of ceramic fragments), have a compact microstructure. The samples show evidence of cracks alongside the ceramic fragments and within the binder matrix.

Besides that, the sample show predominance of Si with high amount of Ca and Al. Mg and Fe have been also found in minor quantities (Fig. 4-21).

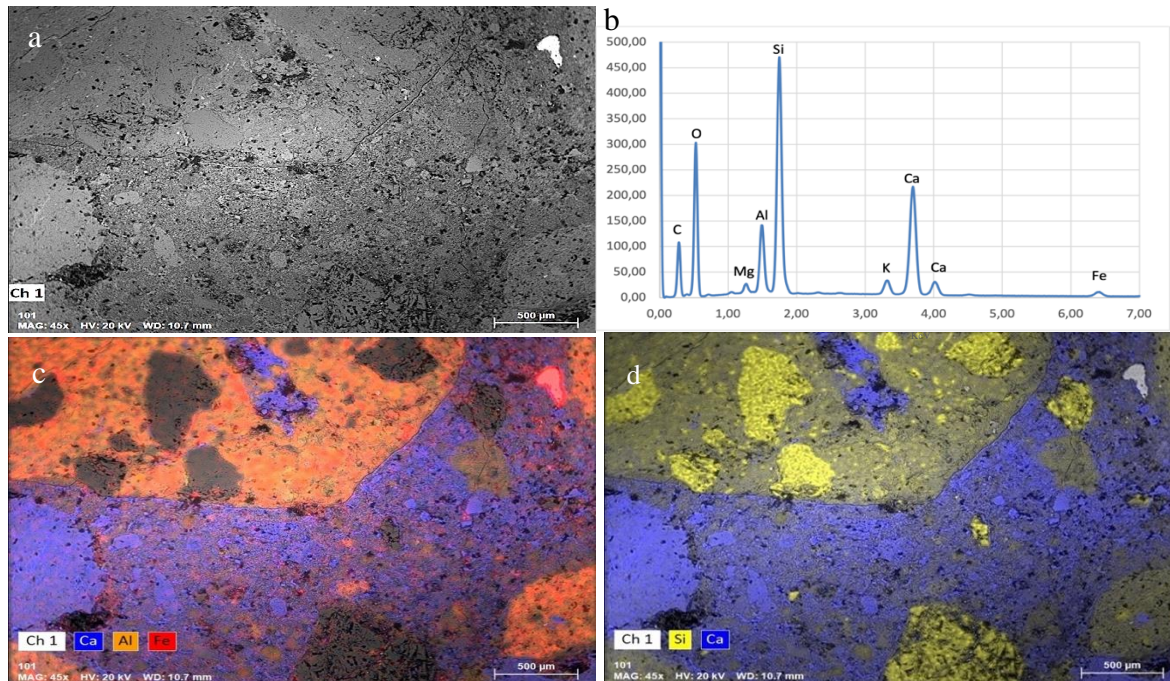


Figure 4.21 a) BSE image on the general composition of sample CR-1706M4, b) EDS spectra of the sample, c) Fe related to Ca and Al, d) relation between Ca and Si. yellow=Si, blue=Ca, orange=Al, red=Fe.

MultiPoint analysis were performed to assess the chemical composition of the binder. The results indicated a fairly homogeneous composition throughout the sample analyzed, in which Ca was the dominant element present associated with Si, Al, Mg, K and Fe was found in minor quantities (Fig. 4-22). A comparative analysis in different parts within the same sample was carried out. Reddish and brownish ceramic fragments were identified, composed of Si, Al, Mg, Fe, K, Na and Ca.

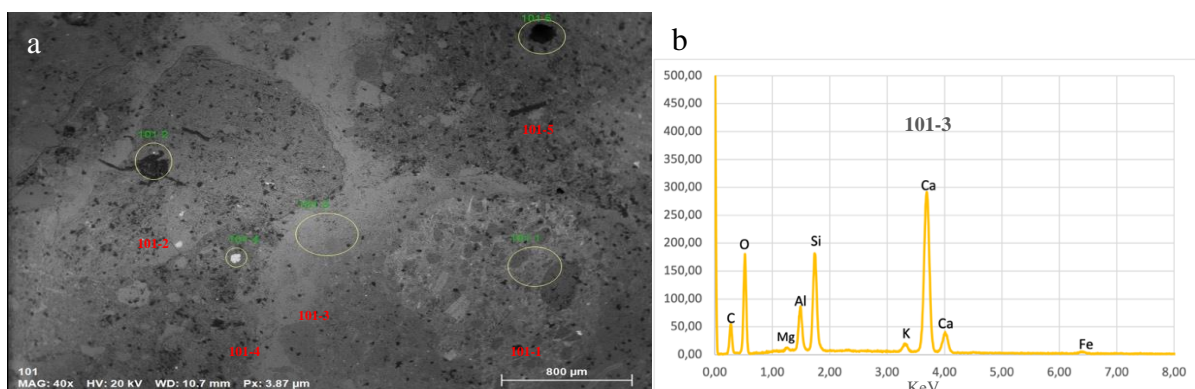


Figure 4.22 a) BSE image on the binder of sample CR-1706M4, b) EDS spectra of point analysis marked in (a).

In samples from Group 4 (CR-915-5 and CR-1131), besides Ca and C, the association of magnesium, aluminum and silicon was detected in the binder matrix and the aggregates. It was

difficult to differentiate the binder from the aggregates, as both binder and aggregate are carbonated. With the objective of understanding the participation of dolostone by calcination for the production of lime, it is verified in all point analyzes (binder/aggregate) that the Ca/Mg ratio is always higher than 1. Point analysis was carried out on both samples and revealed the predominance of Ca over Mg content even in magnesium-rich zones (Fig. 4-23 and 4-24). The elemental maps demonstrate that calcium and magnesium are in opposition to silicon, the main constituent of the silicate aggregates. In some areas of the binder matrix, the preferential association of aluminum with silicon was detected, possibly due to the presence of anorthite, illite and kaolinite, as identified in the XRD analysis

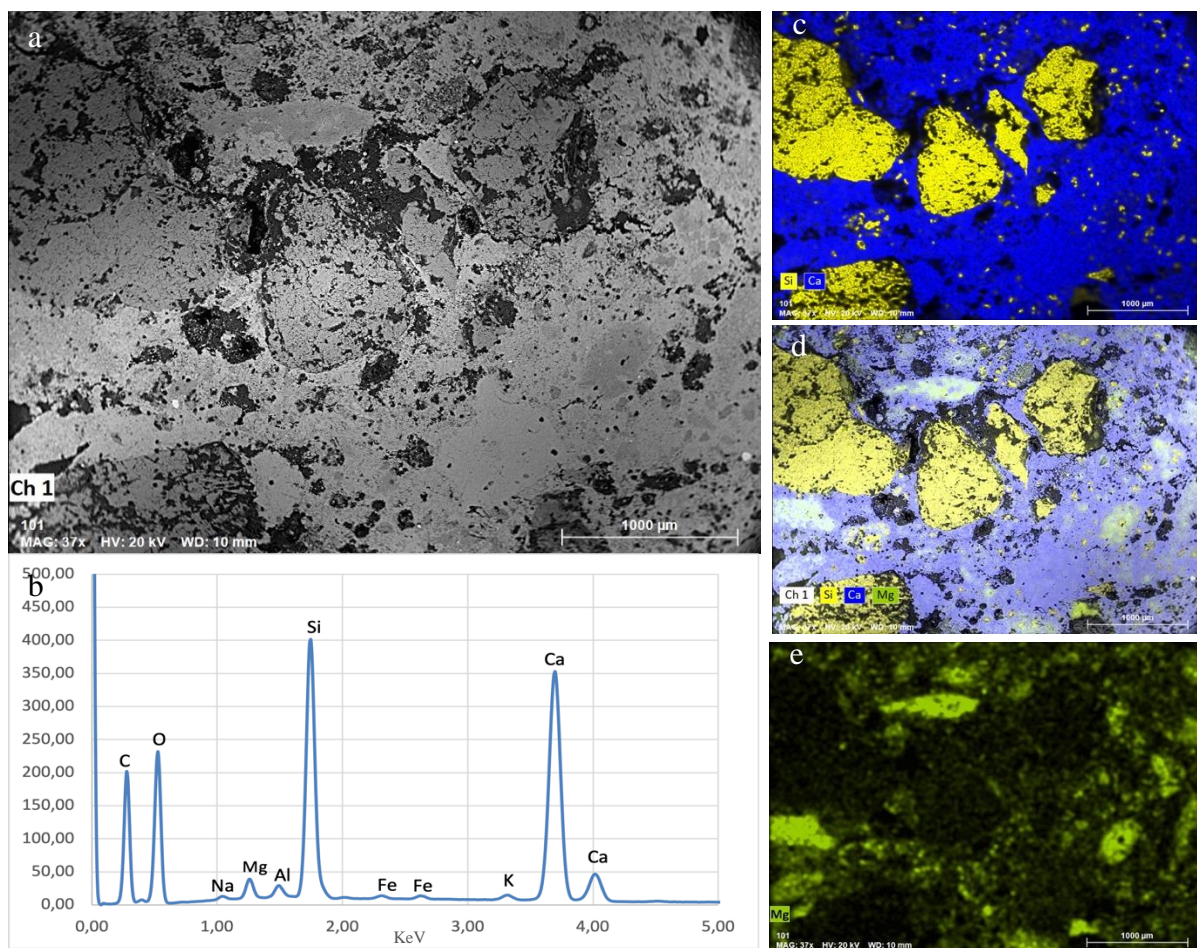


Figure 4.23 a) BSE image on the general composition of sample CR-915-5, b) EDS spectra of the sample, c) relation between Si and Ca, d) Mg related to Ca and Si, e) elemental map of Mg within the composition. yellow=Si, blue=Ca, green=Mg.

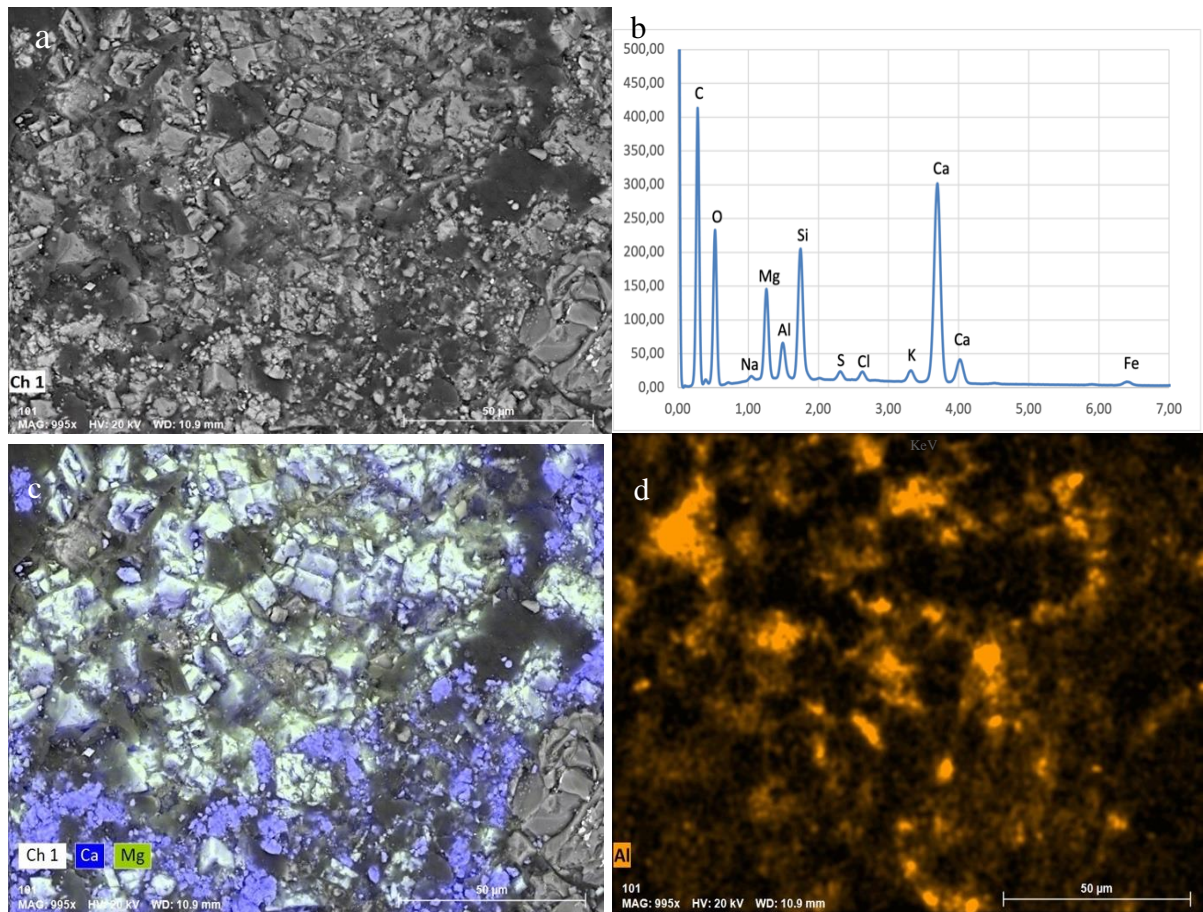


Figure 4.24 a) BSE image on the binder of mortar CR-1131, b) EDS spectra of the sample, c) elemental map of Mg and Ca, d) elemental map of Al. orange=Al, blue=Ca, green=Mg.

Regarding the contemporary samples from Group 5, CR-139 from the nineteenth century has been analyzed under SEM-EDS. As for aggregates, in the general range of the analyzed samples, data obtained by SEM-EDS corroborate the XRD results and the stereoscopic observations, and particles with a strong predominance of silicon were identified (Fig. 4-25 c, d). Micaceous minerals have also been identified from the association of silicon, aluminum, and potassium. Moreover, it was possible to detect coal fragments within the binder from the high concentration of C in association with O (Fig. 4-25 b). The lime lumps, considered as an indicator of the lime used during the mortar preparation, were also identified. The composition is prevalently carbonated, which in conjunction with the microscopic observations leads us to consider that these lumps were probably in the mixture in calcium hydroxide form (slaked lime). As demonstrated in optical analyses, the sub-angular and poorly rounded shape of the aggregates was confirmed (Fig. 4-25 a).

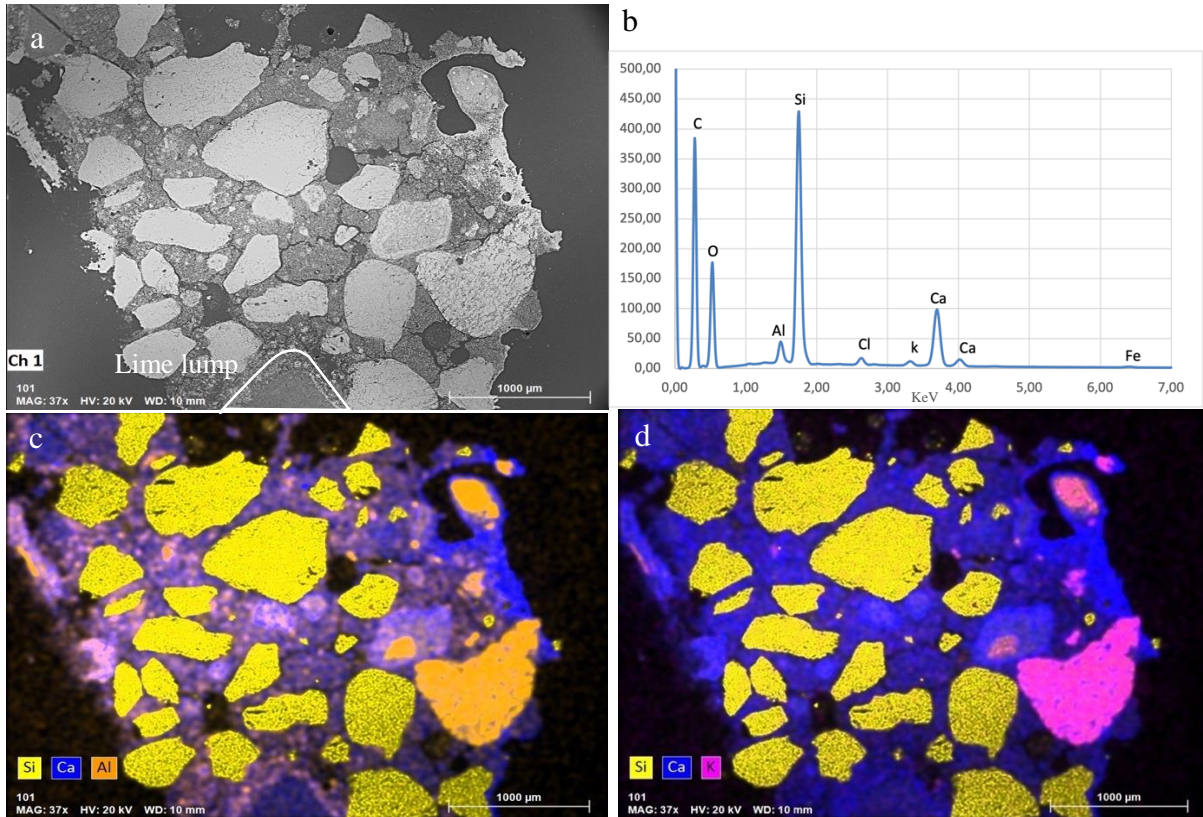


Figure 4.25 a) BSE image on the general composition of sample CR-139, b) EDS spectra of the sample, c) Al related to Ca and Si, d) K related to Ca and Si. orange=Al, blue=Ca, yellow=Si and magenta=K.

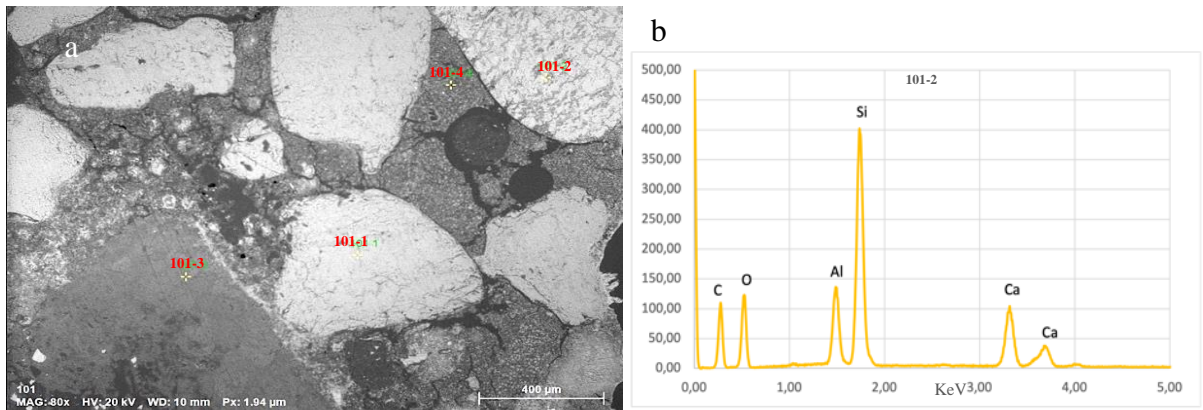


Figure 4.26 a) BSE image on the general composition of sample CR-1131, b) are EDS spectra of point analysis marked in (a)

Sample CR-1628-MP-123 demonstrates different characteristics from the rest of the samples in terms of binder and aggregates, shape and color. From the elemental maps Ca, Si, Al, Ti and Fe have been detected as major elements and Mg as trace element (Fig. 4-27). Point analysis was carried out and revealed the predominance of aluminosilicates (Fig. 4-27g, Fig. 4-27e). Ti and Fe suggests the presence of ilmenite grains (Fig. 4-27c). The binder matrix shows predominance of Ca over all other elements. As demonstrated in optical analyses, the rounded shape of the aggregates was confirmed (Fig. 4-28a).

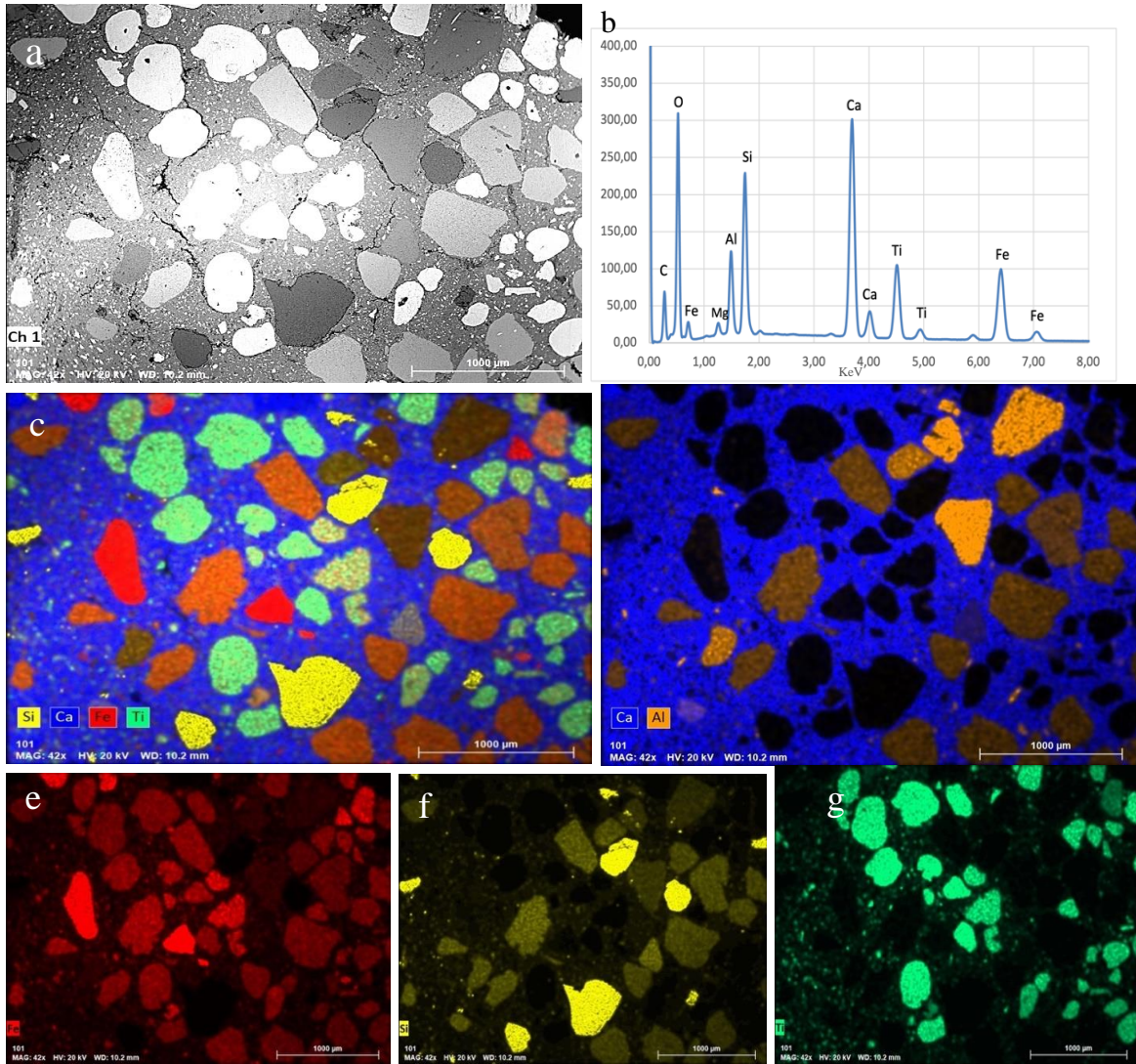


Figure 4.27 a) BSE image on the general composition of sample CR-1131, b-e) are EDS spectrum of point analysis marked in (a), c) Ti related to Fe, Ca and Si, d) relation between Ca and Al, e) elemental map of Fe, f) elemental map of Si, g) elemental map of Ti. Green=Ti, orange=Al, blue=Ca, yellow=Si and red=Fe.

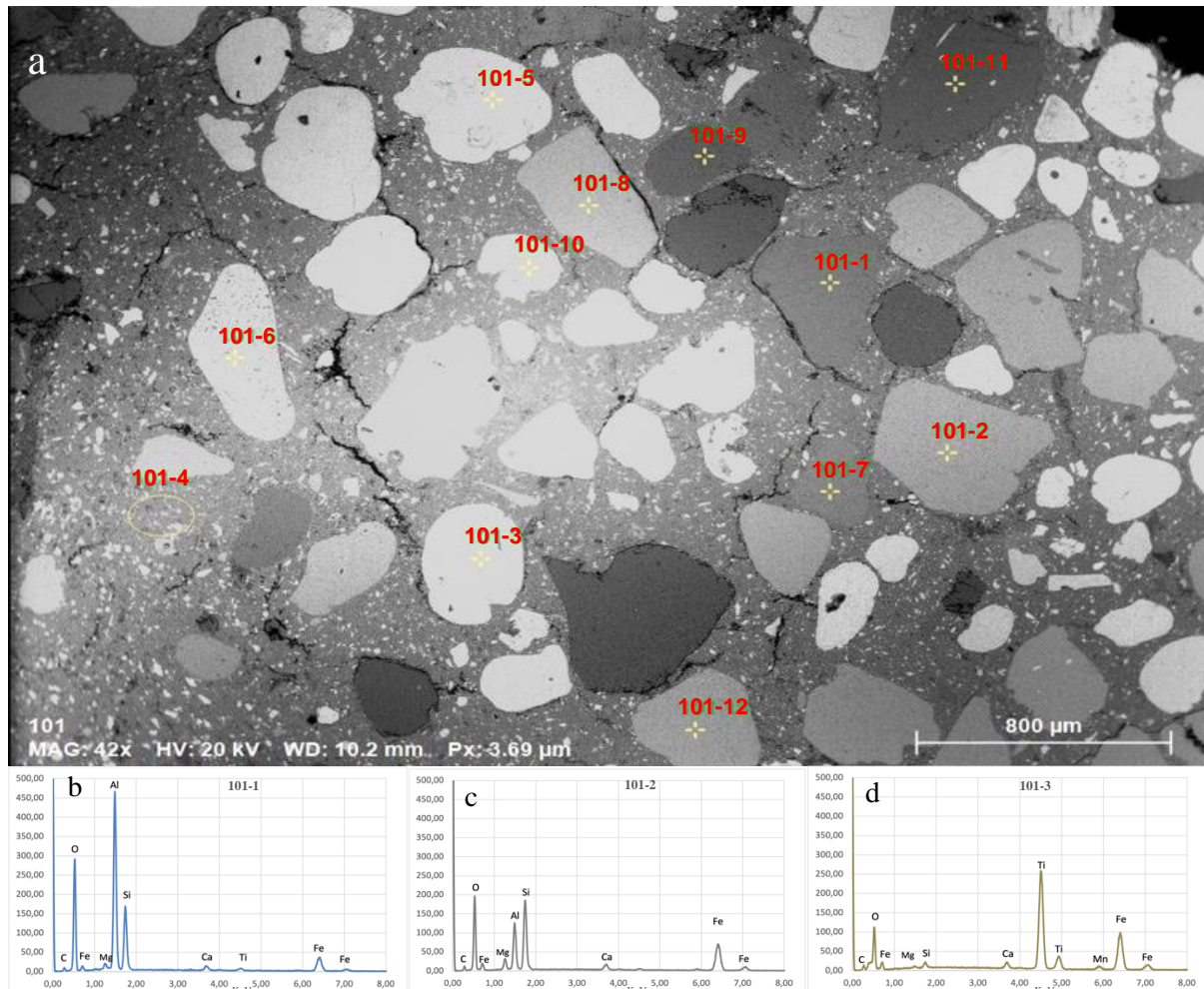


Figure 4.28 a) BSE image on the general composition of sample CR-1628-MP-123, b-d) are EDS spectrum of some point analysis marked in (a).

#### 4.6 ACID ATTACK AND GRANULOMETRIC ANALYSIS

Determination of the ratio between soluble fraction and insoluble residue (Tab. 4-12) has been performed using the results obtained by acid attack. After the attack with hydrochloric acid aqueous solution morphological and mineralogical characterization of the insoluble residue was carried out by observation under the stereo microscope. The soluble fraction represents the binder content, soluble salts, organic matter, and carbonated aggregates while the insoluble residue constitutes of the silicious aggregates within the samples (Silva *et al.*, 2006). The ratio between the soluble fraction and insoluble residue has been obtained for each sample. The percentages of the insoluble residue varied between 12% and 81% whereas the soluble fractions ranged from 19% to 88% (Fig. 4-29).

The analysis was conducted in duplicate, and the mean values were calculated. The results from the two sets in most of the samples were very precise which indicate the homogeneity of the

samples as described in Appendix. 8. Regarding sample CR-915-10 and CR-1638-CLO, there was not enough material, and the analysis could be performed only once. Regarding sample CR-1628MP-123, the analysis was not performed, as sample size was small, and it has undergone only non-distractive analysis (SEM-EDS).

The mortar samples from Group 1 (CR-1638-CLO, CR-1638-ESC and CR-1638-9) presented the highest percentage of insoluble residues ranging from 75 % up to 81 % (Fig. 4-29). The soluble fraction: insoluble residue ratio was 1:6 and 1:9 respectively. Regarding sample CR-1638-9, the ratio between binder to aggregate couldn't have been calculated due to the high presence of shells.

Samples from Group 2, CR-1129A and CR-1129B, showed high percentage of insoluble residues, respectively, 66 % and 72%.

Regarding the samples of group 3, sample CR- 1706M4 and CR- 1706-M6 showed almost similar proportions of insoluble residues 57%, whilst sample CR-2204 showed higher ratio (72%).

Group 4 (CR-915G, CR-915-5, CR-915-6, CR-915-8, CR-915-10, CR-915-18, CR-1131, CR-1537 and CR-1539), displayed the lowest percentages of the insoluble residues which are below 40% in all samples of the group except for CR-915-10 that shows 59% of insoluble residues (Fig. 4-29). They were the only samples that showed a very high amount of soluble fraction against the insoluble residues attributed to the presence of carbonate aggregates, such as limestone or dolomite and organic fragments. The ratio of binder: aggregate could not be determined because the soluble fraction of these samples did not only represent the binder.

Samples from Group 5 showed similar amount of insoluble residue, at 68% and 69% respectively.

The insoluble residues from samples from Group 6 (CR-1706M2, CR-1517, CR-3007 and CR, 3012) varied between 60% and 75%. The percentage of binder to aggregate will not be calculated for samples from Group 6 as they have high presence of lime lumps.

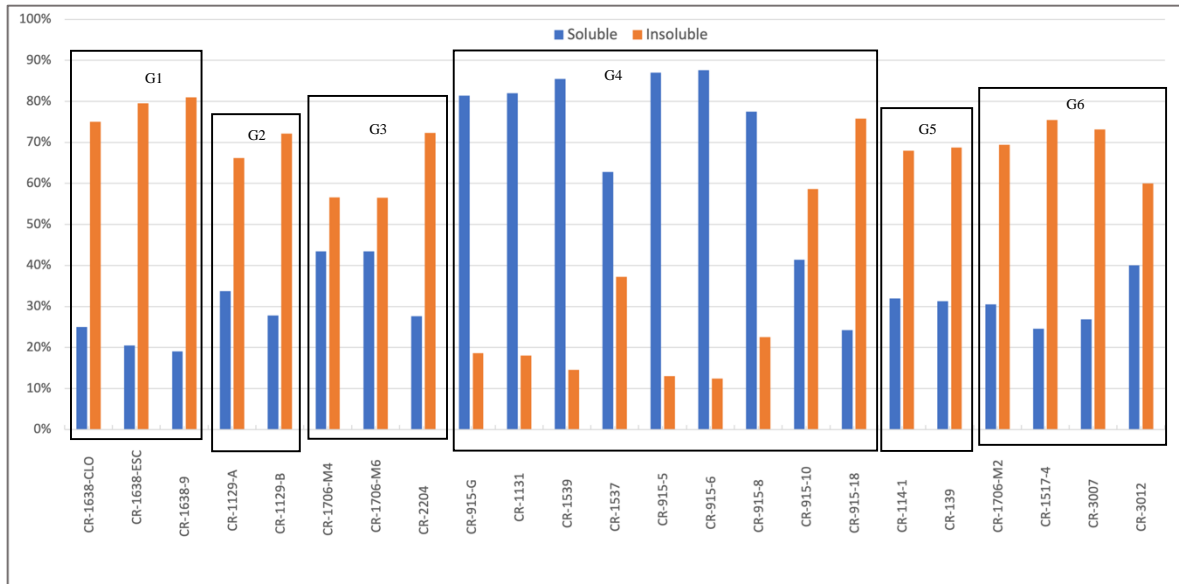


Figure 4.29 Mean values obtained from the soluble fractions and insoluble residues after acid attack.

After the acid attack, granulometric analysis and the observations of the insoluble residue have been done by means of stereo microscope. The sieving of the insoluble residues allowed to determine the grain size distributions of the aggregates and to identify the predominant fraction for each sample by their distribution patterns. The mean values of the particles size from the two sets were calculated (Appx. 9), and the resultant grains have been analysed by means of stereo microscopy and photographed after the sieving process (Appx. 10).

Mortars from Group 1 had its highest amount of the fraction between 0.5 and 01.0 mm (35-40%) which is categorized as coarse sand by Wentworth (1922). The three samples showed relatively similar grain size distribution (Fig. 4-30).

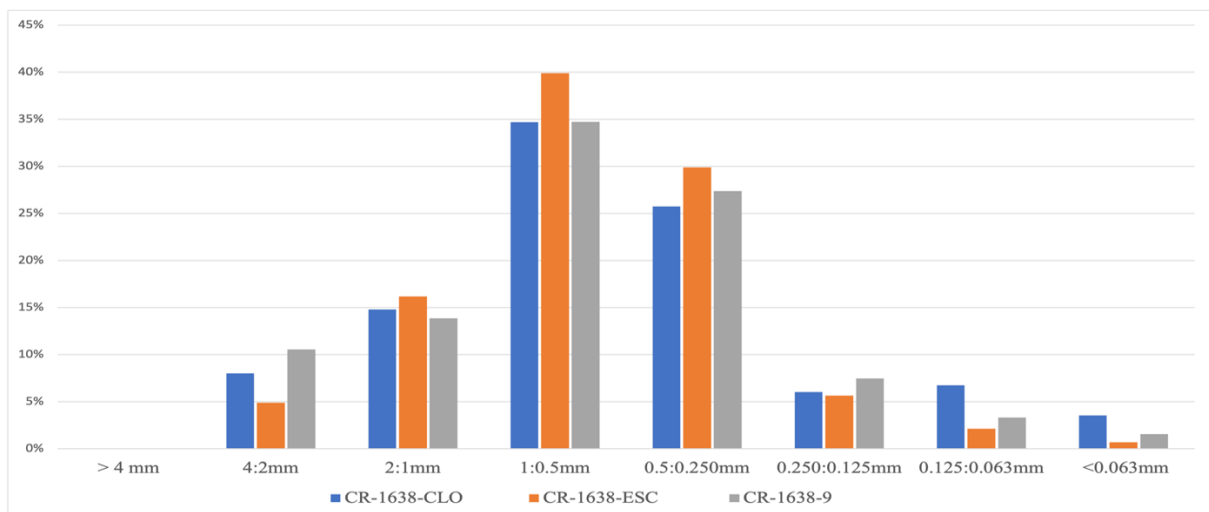


Figure 4.30 Grain size distribution of mortar samples from group 1.

Mortars from Group 2 demonstrate the highest amount of fraction between 1.0 and 2.0 mm (~50%) which is categorized as very coarse sand by Wentworth (1922) (Fig. 4-31), and both samples show very similar grain size distribution.

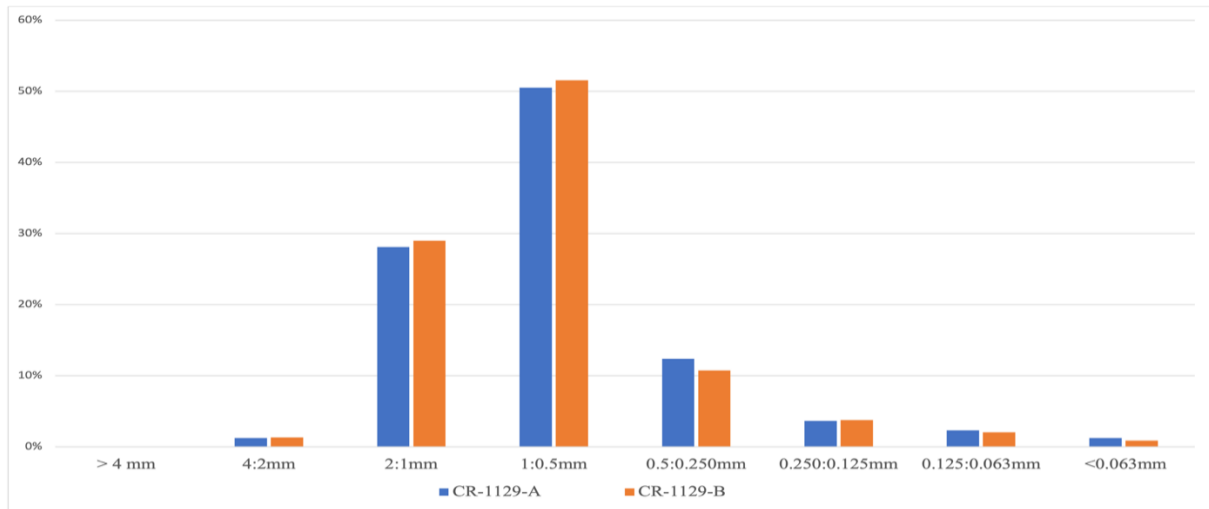


Figure 4.31 Grain size distribution of mortar samples from group 2.

Mortars from Group 3 were the main group showing the highest percentage of coarser fraction (> 4,0 mm) (Fig. 4-32).

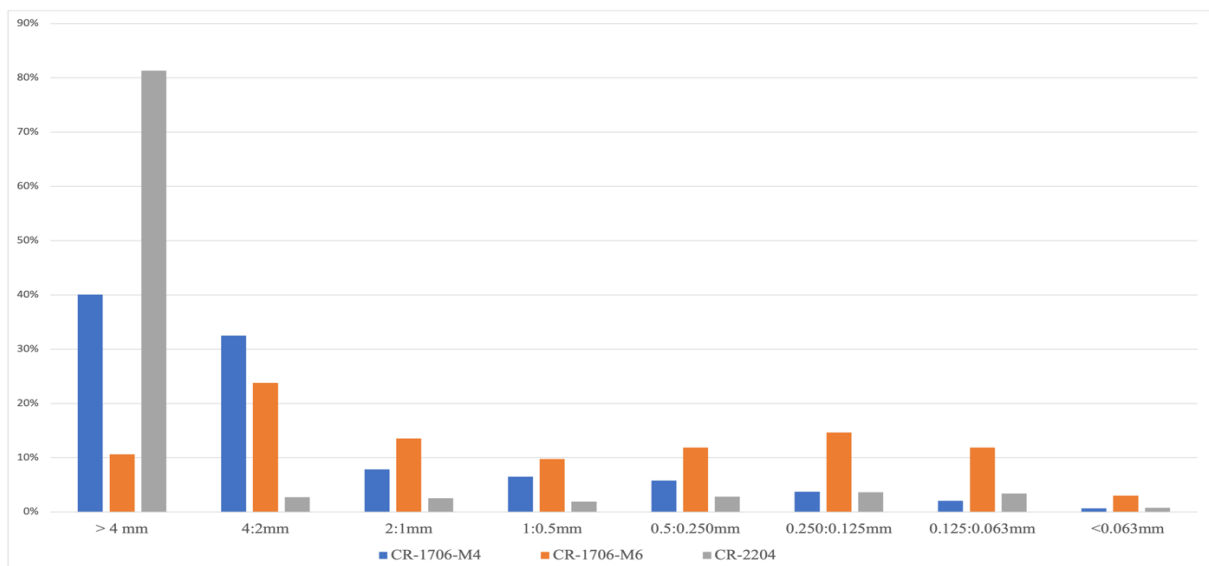


Figure 4.32 Grain size distribution of mortar samples from group 3.

Group 4 displayed a finer grain pattern compared to the other groups by having the highest fraction between 0.063 and 0.250 mm, categorized as very fine sand (Wentworth 1922). However, the lack of greater size fractions may be due to the dissolution of the carbonated aggregates during the acid attack (Fig. 4- 33).

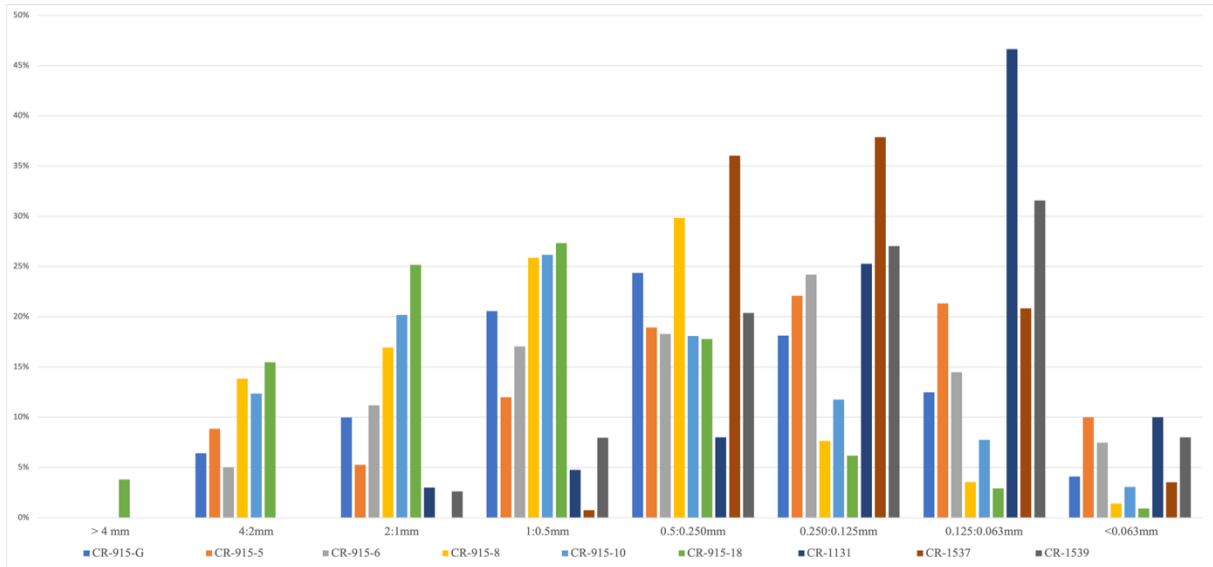


Figure 4.33 Grain size distribution of mortar samples from group 4.

Contemporary mortars (Group 5) show similarity of their grain size distribution (Fig. 4-34). The similar size distribution among the samples of group 5 could be indicative of the templates used for the manufacturing of the recent mortars.

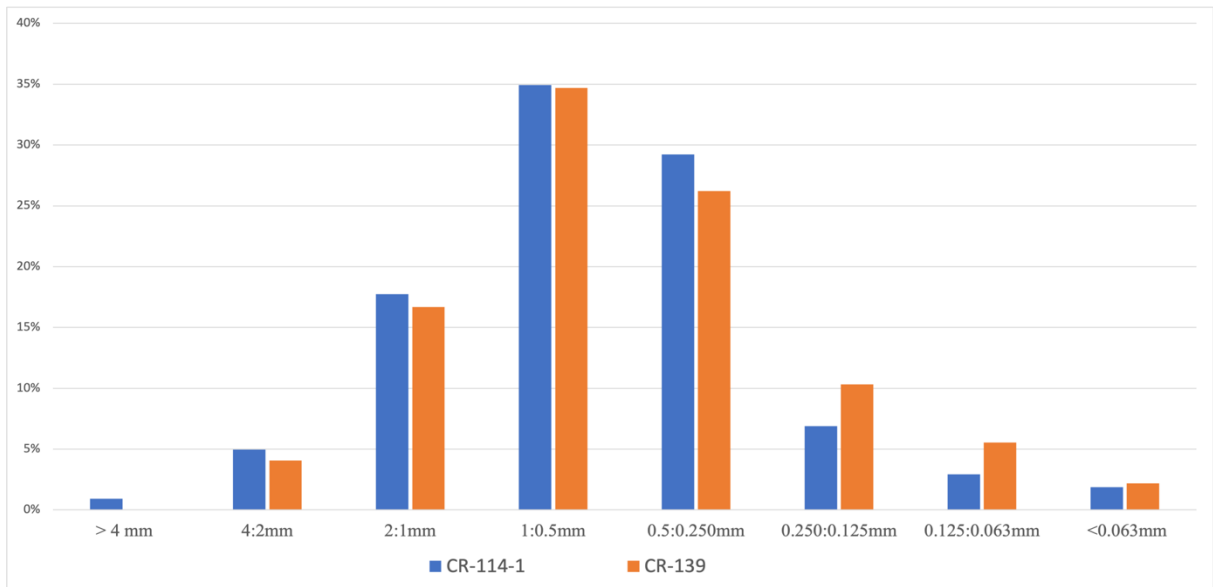


Figure 4.34 Grain size distribution of mortar samples from group 5.

The mortar samples from Group 6 had the highest amount of fraction between 0.5 and 1.0 mm (25-35%) which is categorized as coarse sand by Wentworth (1922) and the four samples showed relatively similar grain size distribution (Fig. 4-35).

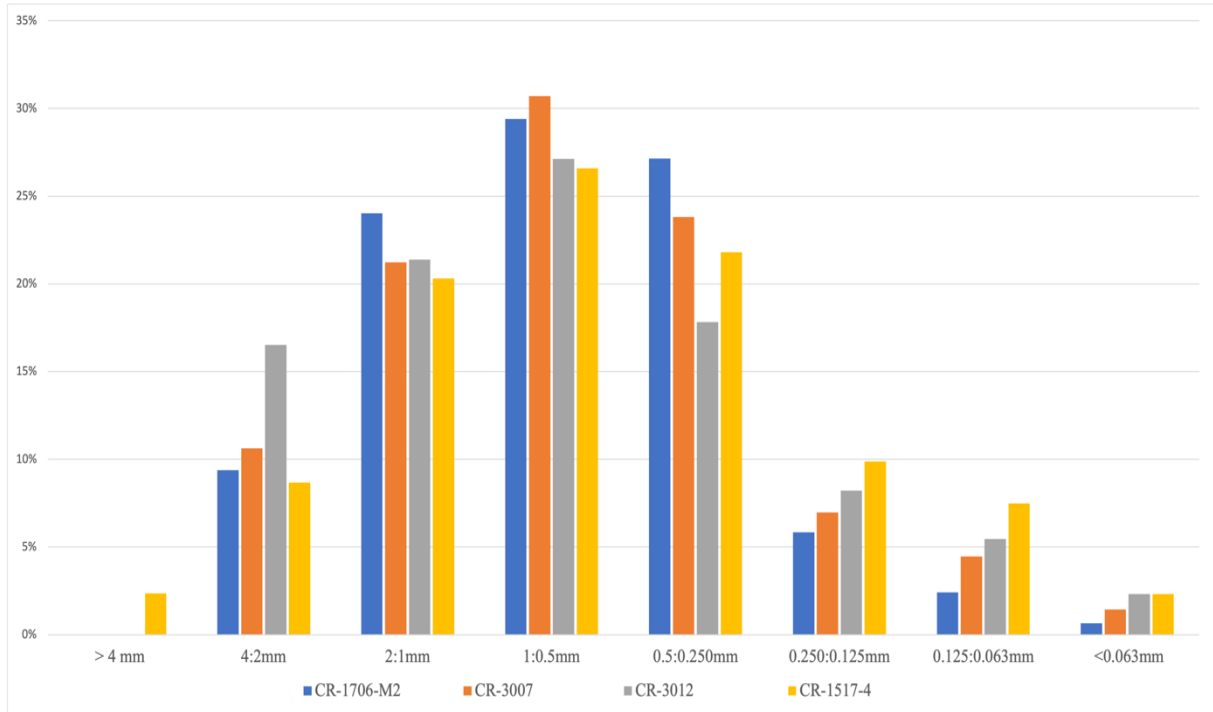


Figure 4.35 Grain size distribution of mortar samples from group 6.

The mean values of the insoluble residues were analyzed using GRADISTAT statistics software. Particle size and textural group description been determined as well as the fractions modality, sorting and the sieving error, which provided a triangular gravel:mud:sand diagram that helped identifying the samples within their correspondent textural group. The results are presented in Table 4.11.

Table 4.11 Results from GRADISTAT based on Udden (1914) and Wentworth's (1922) classifications.

GROUPS	SAMPLE NAME:	SIEVING ERROR (%)	SAMPLE MODE	MAJOR FRACTION		SORTING	TEXTURAL GROUP	MEAN OF THE AGG.
				Size (mm)	W/ (%)			
1	CR-1638-ESC	1.0	Unimodal	1.0:0.5	40	Poorly Sorted	Slightly Gravelly Sand	Coarse Sand
	CR-1638-9	0.6	Unimodal	1.0:0.5	35	Poorly Sorted	Gravelly Sand	Coarse Sand
	CR-1638-CLO	0.7	Bimodal	1.0:0.5	35	Poorly Sorted	Gravelly Sand	Coarse Sand
2	CR-1129-A	0.1	Unimodal	1.0:0.5	51	Moderately Sorted	Sand	Coarse Sand
	CR-1129-B	1.2	Unimodal	1.0:0.5	52	Moderately Sorted	Slightly Gravelly Sand	Coarse Sand
3	CR-2204	0.5	Bimodal	>4.0	81	Very Well Sorted	Gravel	Very Coarse Sand
	CR-1706-M6	0.9	Trimodal	>4.0	40	Poorly Sorted	Sandy Gravel	Very Coarse Sand
	CR-1706-M4	0.5	Unimodal	4.0:2.0	24	Moderately Sorted	Sandy Gravel	Very Coarse Sand

4	CR-915-G	0.4	Unimodal	0.5:0.250	24	Poorly Sorted	Gravelly Sand	Medium Sand
	CR-915-5	0.9	Bimodal	0.250:0.125	22	Very Poorly Sorted	Gravelly Muddy Sand	Medium Sand
	CR-915-6	0.4	Unimodal	0.250:0.125	24	Poorly Sorted	Gravelly Sand	Medium Sand
	CR-915-8	0.4	Unimodal	0.5:0.250	30	Poorly Sorted	Gravelly Sand	Coarse Sand
	CR-915-10	1.1	Unimodal	1.0:0.5	26	Poorly Sorted	Gravelly Sand	Coarse Sand
	CR-915-18	1.3	Unimodal	1.0:0.5	27	Poorly Sorted	Gravelly Sand	Coarse Sand
	CR-1537	1.0	Unimodal	0.250:0.125	38	Moderately Sorted	Sand	Fine Sand
	CR-1131	1.4	Unimodal	0.125:0.063	47	Poorly Sorted	Sand	Fine Sand
	CR-1539	0.1	Unimodal	0.125:0.063	32	Poorly Sorted	Muddy Sand	Fine Sand
5	CR-139	0.8	Unimodal	1.0:0.5	35	Poorly Sorted	Slightly Gravelly Sand	Coarse Sand
	CR-114-1	1.0	Unimodal	1.0:0.5	35	Poorly Sorted	Slightly Gravelly Sand	Coarse Sand
6	CR-3007	1.0	Unimodal	1.0:0.5	31	Poorly Sorted	Gravelly Sand	Coarse Sand
	CR-1706-M2	1.0	Unimodal	1.0:0.5	29	Poorly Sorted	Gravelly Sand	Coarse Sand
	CR-1517-4	0.5	Unimodal	1.0:0.5	27	Poorly Sorted	Gravelly Sand	Coarse Sand
	CR-3012	0.8	Unimodal	1.0:0.5	27	Poorly Sorted	Gravelly Sand	Coarse Sand

The gravel:mud:sand triangular diagram (Fig.4-36) has been built using GRADISTAT statistics software and the results determined that the samples can be represented by seven different textural groups as following; muddy sand, gravelly muddy sand, sand, slightly gravelly sand, gravelly sand, sandy gravel and gravel. Almost all samples are poorly sorted apart from CR-1129-A, CR-1129-B, CR-1537 and CR-1706-M4 that are moderately sorted. Sample CR-915-5 (Group 4) is located in the poorly sorted region whilst sample CR-2204 (Group 3) is located in the well sorted region. The results from GRADISTAT for all samples displayed a unimodal fraction trend except for the samples CR-1638-CLO, CR-915-5 and CR-2204 that they showed a bimodal fraction trend and the sample CR-1706-M6, which was the only sample showing trimodal trend (Tab. 4-12). The mortars from group 1 were located in sand, slightly gravelly sand and gravelly sand textural groups, samples from Group 2 were located in sand, muddy sand, gravelly muddy sand, gravelly sand. whilst samples from group 3 with ceramic fragments were located in the sandy gravel and gravel textural group (Fig. 4-36). Samples from Group 4 have been sorted between gravelly sand and muddy sand. They showed mostly small

grain particles comparing with the rest of samples and the presence of micras has been confirmed by means of stereo microscope as well (Fig. 4-36). All samples from Group 5 have been sorted as slightly gravelly sand, whilst samples from Group 6 have been sorted as gravelly sand. Moreover, it was also indicated that the sorting type ranges between very poorly sorted and very well sorted (Tab. 4-12).

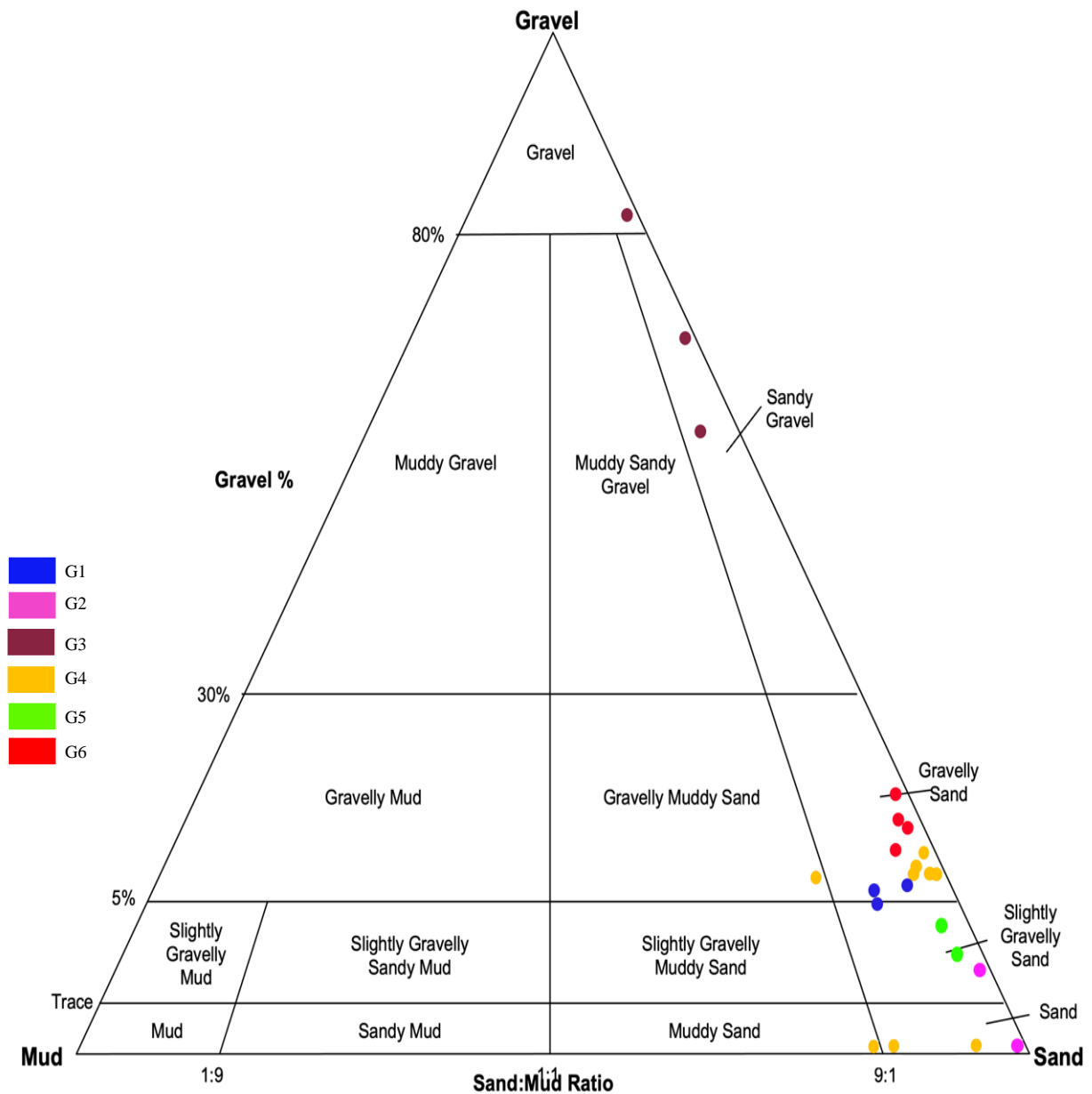


Figure 4.36 Gravel:mud:sand diagram from GRADISTAT.

For sample CR-1628-MP-123, it was not possible to treat this sample with acid, so it was not possible to apply the granulometric analysis using GRADISTAT, therefore the granulometric study was done using IMEJEJ as shown in figure 4-37, and it displayed a unimodal fraction trend, and the grains size varied between 0.063 and 1.00 mm with a high degree of roundness and homogeneity. To ensure the accuracy of the results, a comparison of the data between GRADISTAT and IMAGEJ was carried out by analyzing sample CR-1706-M6 with the two softwares, which demonstrated an accuracy of 90%

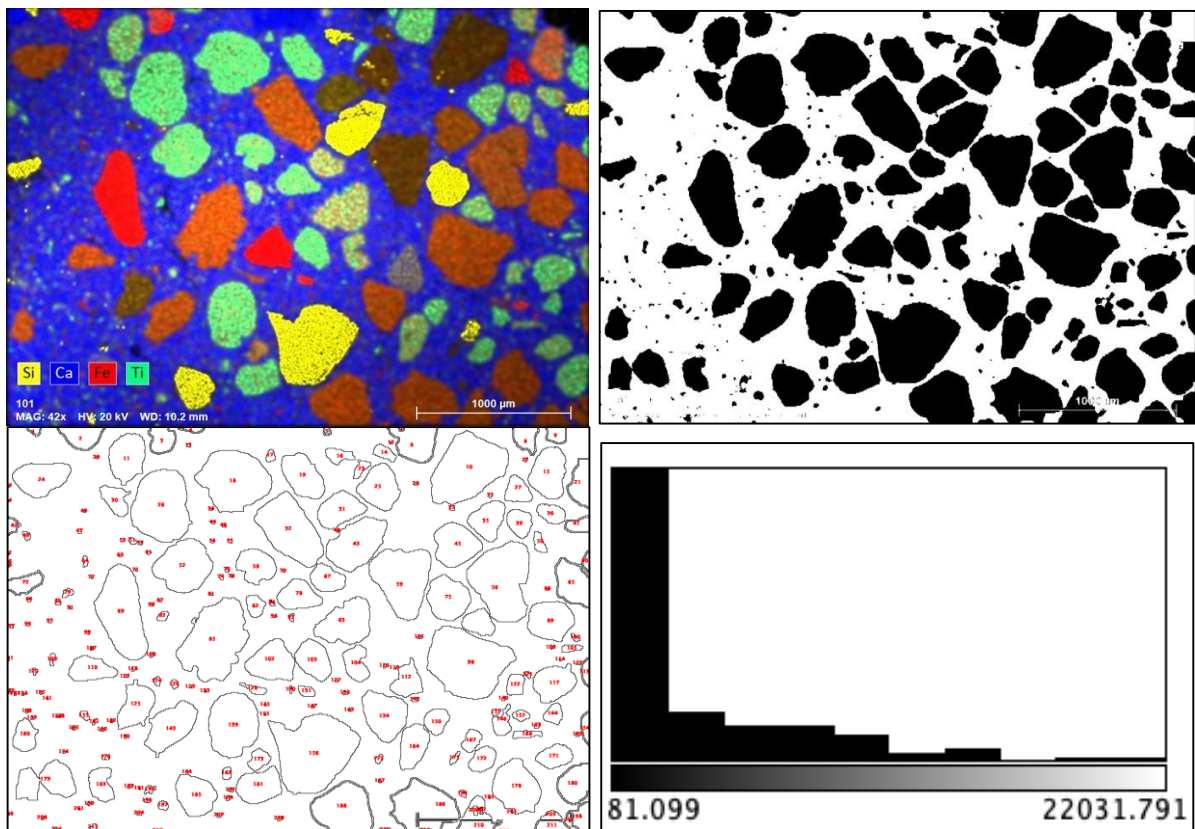


Figure 4.37 Representative grain distribution images sample CR-1628-MP-132 using IMAGEJ software.

## 5 DISCUSSION

---

The mortar samples from the Roman Cryptoporticus of Lisbon were analyzed through a multianalytical archaeometric approach.

The samples were divided into six groups, according to the initial visual examination (Tab. 4-1). The division is based on the most abundant type of aggregates or on remarkable differences; 1) quartz rich; 2) with chromatic layer; 3) with ceramic fragments; 4) with carbonate lithics aggregates; 5) interventions from 19<sup>th</sup> and 21<sup>st</sup> century, and 6) quartz rich with noticeable presence of lime lumps. The grouping has been confirmed with their functions; filling, render and bonding in order to assess the possible provenance to understand whether ancient recipes from old roman treatises were followed, or if they were changed due to the availability of resources or to adapt a specific need.

According to the macro characteristics, after studying the six groups, it can be concluded that group 1, 2, 5 and 6 are similar in terms of mineralogical characteristics as they have quartz as a main aggregate with mainly sub-rounded morphology, although there are some distinguishing characteristics of each group. The sub-rounded quartz aggregate, dominant in almost all samples, is likely have been sourced from the river deposits from the surrounding Tagus River.

In group 2, the presence of Cu with Si in the pigmentation indicates that the composition might be made up of copper silicium, which might be the pigment chrysocolla based on the previous literature (Jorge 2021).

Group 3 is characterized by the presence of huge fragments of ceramic as the main aggregate, and the mortars from this group were used as render mortars from walls.

For group 4, it is characterized by containing predominance of carbonates as binder and as the main aggregate with also high presence of dolomite.

### 5.1 RAW MATERIALS

#### 5.1.1 Binder

On the basis of the results obtained by OM, XRD, TGA-DTG and SEM-EDS it was possible to determine that the use of lime, as the binding media in mortar manufacture and more

specifically of a calcitic nature. Predominant composition of calcite mineralogical phase was identified in all groups. Accordingly, all samples can be categorised under one group regarding to the binder.

Binder of the samples from group 4 as confirmed by SEM-EDS analysis, the binders possess a high content of Ca with high amount of Mg and Si. Angular calcitic grains of recrystallized limestone and dolomite were visible in by SEM, and the binder wasn't easily distinguishable from the aggregates, which confirm the results from OM assuming that the main aggregates are carbonate stones with a small amount of binder.

Additional point analysis resulted that the high amount of Mg corresponding to the aggregate composition and the binder is mainly calcitic binder. The results from XRD and TGA of the samples are also very similar allowing them to be correlated together in the same historical structure.

The samples from group 2 and 6, on the basis of the elemental maps obtained by SEM-EDS analysis present that samples have only Ca-rich zones in the binder. The point analysis revealed again the predominance of Ca. Although samples from the two groups are mortars from different places and with different functions, the similarities in their binders allow them to be grouped with the same manufacturing techniques.

The percentage of Ca regarding the samples of group 1 and group 5 refers to mortars with high hydraulic properties, probably as a result of the pozzolanic aggregates or additives used. As observed by SEM-EDS analysis, the binder is heterogeneous, with areas enriched in Ca together with Si and Al. Both group 1 and group 5 presented low carbonate composition, nevertheless, the carbonated areas prevail Ca enrichment. Samples from group 3 showed moderate predominance of Ca confirming that binder is lime binder

Lime lumps were observed in all samples and with different proportions except on the ones from group 4. Point analysis of the lime lumps by VP-SEM-EDS was performed to obtain a better signature of limestone used as raw material (Bakolas *et al.*, 1995; Elsen, 2006). Results indicate the generalized and abundant presence of Ca, interpreted as calcium carbonate ( $\text{CaCO}_3$ ), with trace amount of Si and Al probably related with siliceous phase, such as clay. Cl and S related to the presence of salts, such as halite ( $\text{NaCl}$ ) and gypsum ( $\text{CaSO}_4 \cdot 2\text{H}_2\text{O}$ ), respectively. The results on binder composition in accordance with the composition of calcitic aerial lime. The lime lumps from the 19<sup>th</sup> and 21<sup>st</sup> century samples showed higher presence of Si than the ones from the roman samples, so probably a different limestone, which suggests the use of a different limestone as raw material for the mortar manufacture.

### 5.1.2 Aggregates

The mortars present several aggregate compositions, they are mostly siliceous (quartz, feldspar, ceramic fragments) or carbonated as for the aggregates from group 4.

In samples from group 1, the presence of shells and lime lumps as aggregate is detected. The results are confirmed using complementary techniques, such as OM, SEM-EDS. Feldspars are detected in all samples by OM XRD and SEM-EDS analysis. Micas are also detected in most of the samples. Presence of amphiboles has also been verified by XRD analysis in group 3 samples (with ceramic fragments).

Group 4 samples (CR-915-5, CR-915-6, CR-915-8, CR-915-G, CR-1539, CR, 1537 and CR-1131) showed the highest percentage of weight loss between 60-80% of their initial weights due to the dissolution of the carbonate fragments within their composition.

The samples of group 5 (CR-114 and CR-139) that correspond to mortars used during interventions in the 19<sup>th</sup> and 20<sup>th</sup> century, show calcite decomposition at around 730°C, as observed in their DTG curves, which is slightly lower in comparison to the Roman samples (Appx. 6). The presence of lime lumps, under burned lime and limestone fragments indicate the mortar used was produced by dry slaking.

In terms of the angular morphology, in group 1, 2, 5 and 6, aggregates are found mostly in sub-angular and angular forms indicating a short distance of transportation of the sediments from the geological source, except for sample CR-1628MP-132, that presents sub-angular and/or well rounded. Group 3 has mainly angular ceramic fragments, whilst the samples from group 4 have angular and sub-angular lithic aggregates, observed using optical microscopy.

In TGA analysis the thermograms of group 4 samples (Fig.4-7), the calcite decomposition occurred at around a temperature of 800°C as observed in their DTG curves slightly higher than the rest of the samples (Appx. 6), possibly due to the higher levels of crystallinity or bigger aggregate sizes of the calcium carbonates (Földvári, 2011). The two different decomposition peaks observed in some of the samples of group 4 there were found within the range of 600-900 are attributed to the decomposition of MgO and of CaO, respectively. Dolomite is present as aggregate, and calcite is present in the form of binder and of aggregate.

The carbonate aggregates from group 4 exemplified by the shells and the carbonated lithoclasts, are the second most presented aggregates right after the siliceous aggregates. The predominant granulometric class in most samples corresponds to the fraction between 0.5 and 1.0 mm, but

samples with ceramic fragments (Group 3) present predominantly coarser classes, greater than 4 mm. Micaceous minerals and other minerals from the phyllosilicates occur in small proportions, or trace amounts. The presence of kaolinite, an expansive clay mineral, stands out in three samples (CR-915G, CR-915-5 and CR-1537). Other reduced or trace occurrences make up the set of compounds identified and should be associated with other constituents, such as pyroxenes, probably associated with lithoclasts of volcanic origin. In general, the presence of chlorides is compatible with the use of aggregates (sands) of marine origin or transition environments whose salinity is intermediate. It should be noted also that samples from group 4 were different from a granulometric point of view, whose granulometric characteristics for the insoluble aggregates reveal smaller aggregates in a very small proportions comparing with rest of the samples.

## **5.2 PROVENANCE**

Considering the local geological framework, the origin of the aggregates is in the marginal fluvio-estuarine sediments. The deficient degree of calibration and the variable degree of roundness, reveal a textural immaturity compatible with that type of sediments. Allied to the frequent presence of carbonate bioclasts and the relatively low levels of soluble salts present, the possibility that they are sediments exposed to brackish environments, of intermediate salinity, is quite plausible for this type of sedimentary environment, in which the deposits are located in the sediments (alluvium) of the Tagus estuary.

The mineralogical composition of the aggregates is mainly quartz, feldspars and micas. Single mineral grains are found mostly in sub-angular and poorly rounded shape in association with each other as rock fragments. Such morphology is indicative of a long distance of transportation of the aggregates that can be collected at the margin of Tagus River, aggregating also with the study done on mortars from the city of Lisbon by Luis Almeida (Almeida, 2015).

In terms of the binder, the analysis indicates the use of calcitic lime binder for the mortar production and some impurities were detected in the 19<sup>th</sup> and 21<sup>st</sup> centuries render mortars (CR-319 and CR-114).

Although the correlation of the lime properties of the binder with the geological data is often challenging as the carbonates in the binder are no longer representing the exact original composition (Lammel and Lehrberger, 2007) it is assumed that the local sources may have been

preferred. It is likely that the lime was obtained from different units of limestones (Fig. 5-1). The abundance of limestone lithologies with small number of detrital fractions, clayey (limestones and clayey limestones), is compatible with the chemical composition of the binder of the lime mortars studied and the impurities are associated with it.

Finally, it is reasonable to conclude that during the Roman Era, raw materials were sourced from a location within a close proximity to the site of construction due to transport limitations.

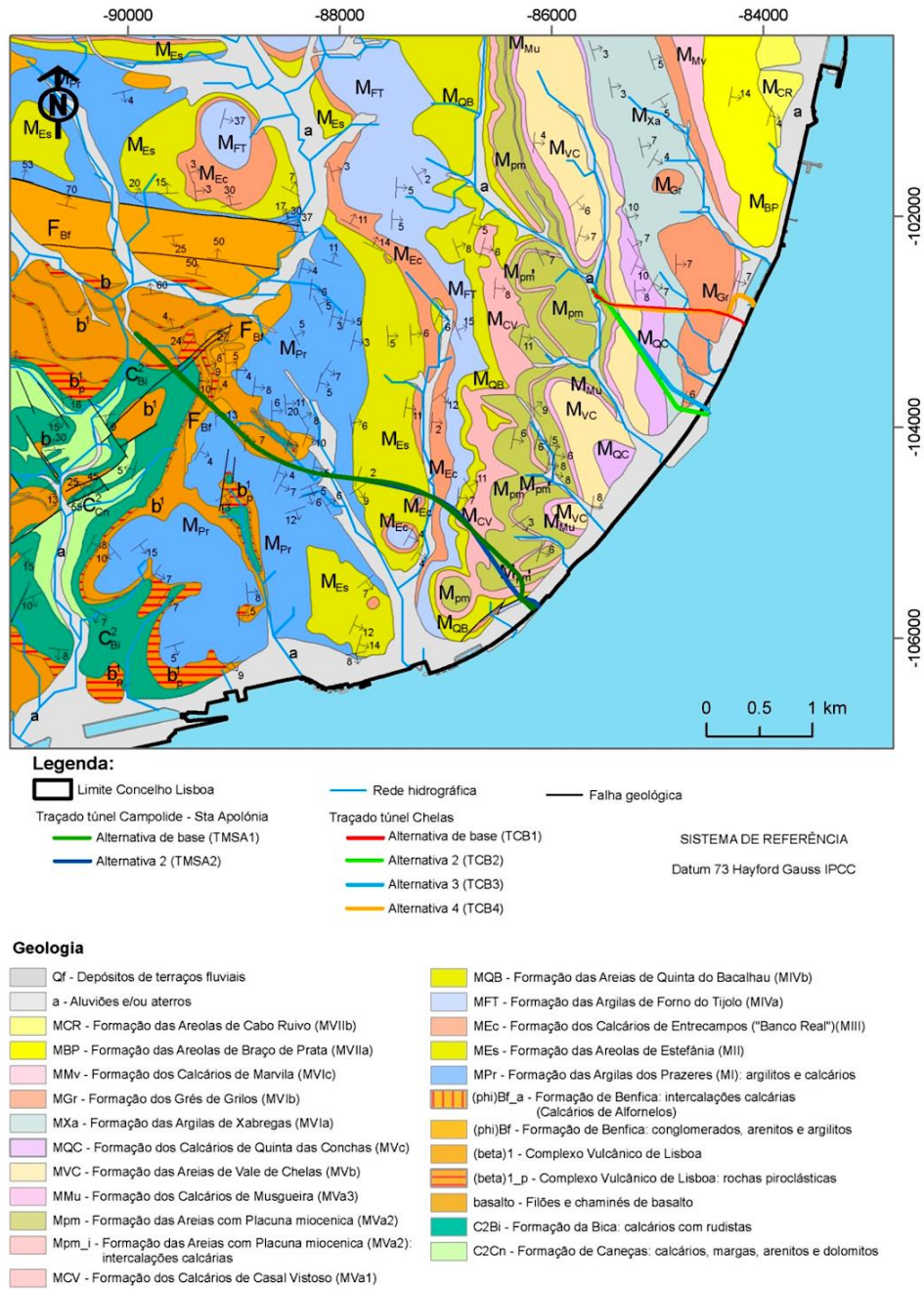


Figure 5.1 Extract from the Geological Chart of the municipality of Lisbon at a scale of 1: 10 000 (MOITINHO DE ALMEIDA, 1986).

### 5.3 PRODUCTION TECHNOLOGY

The study of mortars reveals crucial information about the constructor's technological knowledge and how they applied it to achieve the required construction needs. Moreover, contributes to understand the production technology applied and to compare the distinctions and similarities of the diverse building practices.

Based on the results of the analytical techniques, some compositional differences of the mortars seem to be associated to different location or structural requirements. The simplified compositions are calculated through Jedrzejewska method using the estimated percentages of carbonates by the TGA data together with insoluble residue analysis (Jedrzejewska, 1960).

The groups 1, 2, 5 and 6 showed similarities according to the technological choices applied. The manufacturing techniques depend on sand and silicious materials mainly as an aggregate, which was confirmed by the results of acid attack and granulometric analysis, as all samples contain more than 50% of insoluble residues. Despite the aggregates variations, functions and location of these samples, they display similar binder: aggregate ratios ranging between 1:3 and 1:4. Such proportion correlates with the ancient practices as suggested by Vitruvius in *De Architectura*. The ideal proportion advised in his treatise, in the case of using pit sand is 1:3 (Book II, Chapter V, Vitruvius).

Group 3 with ceramic fragments remained as a separate group based on their manufacturing as described in table 5-1. The particularity in the manufacturing technique for this group is the use of ceramic fragments as aggregates in the mortar used as a wall render. The samples of this group are collected from an outer layer mortar which is deduced to protect the walls that were highly exposed to water. Despite the fact that all walls of the building were exposed to the water in one way or another, ceramic wall render was used only in certain places and not in all parts. A possible interpretation of this could be that these sites may have been used to store water and ceramic wall render was applied to avoid the effects of a direct contact with the water.

Samples from the group 4 also constitute as a separate group considering their production technology distinguished due to the use of a high proportion of lithic aggregates. The use of lithic carbonates as the main aggregate was also confirmed by means of acid attack and granulometric analysis (Tab 5-). Samples from this group belong to filling mortars used in floor construction, except for one sample from a wall filling mortar, the reason for that is not clear if it was intended by the builders for a specific purpose or not.

The production recipe in the 19<sup>th</sup> and 21<sup>st</sup> century is similar to the ones used in roman structures, more precisely with samples from group 1.

Table 5.1 Subdivision of samples by groups used for discussing the manufacturing techniques.

Quartz				Limestone and dolomite		Ceramic fragments	
A (Filling)		B (Render)		Sample	Function	Sample	Function
Sample	Function	Sample	Function				
CR-114	Filling (wall)	CR-1129-A	Render (wall)	CR-1537	Filling (Floor)	CR-2204	Render (wall)
CR-139	Filling (wall)	CR-1129-B	Render (wall)	CR-915-5	Filling (Floor)	CR-1706-M4	Render (wall)
CR-1706-M2	Filling (wall)	CR-1638-ESC	Render (floor)	CR-915-6	Filling (Floor)	CR-1706-M6	Render (wall)
CR-915-10	Filling (floor)	CR-1638-9	Render (floor)	CR-1539	Binding (floor)		
CR-915-18	Filling (floor)			CR-1131	Filling (Floor)		
CR-3007	Filling (floor)			CR-915-G	Filling (wall)		
CR-3012	Filling (floor)						
CR-1517-4	Filling (Floor)						
CR-915-8	Filling (Floor)						
CR-1638-CLO	Filling (floor)						

Table 5.2 Simplified compositions of the mortars (%) using Jedrzejewska method (Jedrzejewska, 1960).

Group	Sample	Aggregates		Total aggregates	“Binder”	Binder: aggregate
		Soluble fraction (%) <sup>1</sup>	Insoluble residue (%) <sup>2</sup>		Carbonates (%) <sup>3</sup>	
1	CR-1638-CLO	10.0	75.0	85.0	15.0	1:6
	CR-1638-ESC	10.7	80.2	90.9	9.1	1:9
	CR-1638-9	8.4	81.3	89.7	10.3	-
2	CR-1129-A	8.1	66.0	74.1	25.9	1:3
	CR-1129-B	4.3	72.1	76.4	23.6	1:3
3	CR-1706-M4	7.6	57.4	65.0	35.0	1:2
	CR-1706-M6	17.4	57.2	74.6	25.4	1:3
	CR-2204	7.4	62.1	69.5	30.5	1:3
4	CR-915-G	18.5	19.1	37.6	62.4	-
	CR-915-5	5.1	13.0	18.1	81.9	-
	CR-915-6	14.1	12.0	26.1	73.9	-
	CR-915-8	35.6	23.2	58.8	41.2	-
	CR-915-10	15.3	59.1	74.4	25.6	-
	CR-915-18	5.2	66.0	71.2	28.8	-
	CR-1131	5.2	18.1	23.3	76.7	-
	CR-1537	4.6	17.4	22.0	78.0	-
CR-1539	7.6	15.0	22.6	77.4	-	

5	CR-114	25.2	68.4	93.6	6.4	1:14
	CR-139	18.4	69.2	87.6	12.4	-
6	CR-1517-4	11.1	75.0	86.1	13.9	-
	CR-1706-M2	16.2	69.2	85.4	14.6	-
	CR-3007	19.6	73.3	92.9	7.1	-
	CR-3012	13.2	60.1	73.3	26.7	-

<sup>1</sup> Soluble fraction = 100 -  $\Sigma$  (insoluble residue + carbonates)

<sup>2</sup> Insoluble residue hydrochloric acid

<sup>3</sup> Calculated from CaCO<sub>3</sub> content (by TGA analysis)

<sup>4</sup> Binder (considered to be the carbonate fraction) and aggregate (sand + soluble fraction)

Samples were also studied in terms of their level of hydraulicity. Based on the results obtained by TGA analysis, the ratio between carbon dioxide (CO<sub>2</sub>) to structurally bound water (H<sub>2</sub>O) in relation to carbon dioxide (CO<sub>2</sub>) can be calculated to relate it to the hydraulic degree of the mortars (Moropoulou *et al.*, 2005). The hydraulicity of different types of mortars has been studied and it was determined that the lower the CO<sub>2</sub> ratio is, the higher the hydraulicity.

Results suggest that there are three discernable assemblages of clusters according to their hydraulicity index (HI) and the relationship between CO<sub>2</sub> to structurally bound water ratio *versus* the CO<sub>2</sub> mass losses (Fig. 5-.2).

The samples were classified based on table 5-1. Samples with the lowest CO<sub>2</sub>% mass losses and a lower HI index (Fig. 5.1, blue), correspond to samples from group 1, with high percentage of insoluble residues and quartz as main aggregate with the presence of very small fragments of ceramics in the composition. They are samples functioning as floor filling except for sample CR-114 and CR-139 they are wall filling. They display the highest binder to aggregate ratios ranging from 1:6 to 1:9 and have a similar particle size distribution dominated by quartz particles greater than 1mm. This set of samples hold the highest hydraulicity character, which is compatible with their function. Hydraulicity is an intrinsic characteristic for mortars that are employed for flooring purposes and walls in a hydraulic structure.

The second cluster with medium hydraulicity (Fig. 5-2, red), which contain group 3 samples with ceramic fragments plus the samples from group 1 with high proportion of quartz aggregates. They display a binder to aggregate ratios ranging from 1:2 to 1:3. The third identified cluster (Fig. 5.2, green) includes all samples from the group 2 with carbonate lithic aggregates. These samples have the highest HI index and therefore, the lowest hydraulicity. Their high CO<sub>2</sub>% and their low percentage of structurally bound water, locate them far away

from the other samples in the chart, discarding a direct correlation with the samples related to the hydraulic structures of the first two clusters with lower CO<sub>2</sub>/H<sub>2</sub>O ratios.

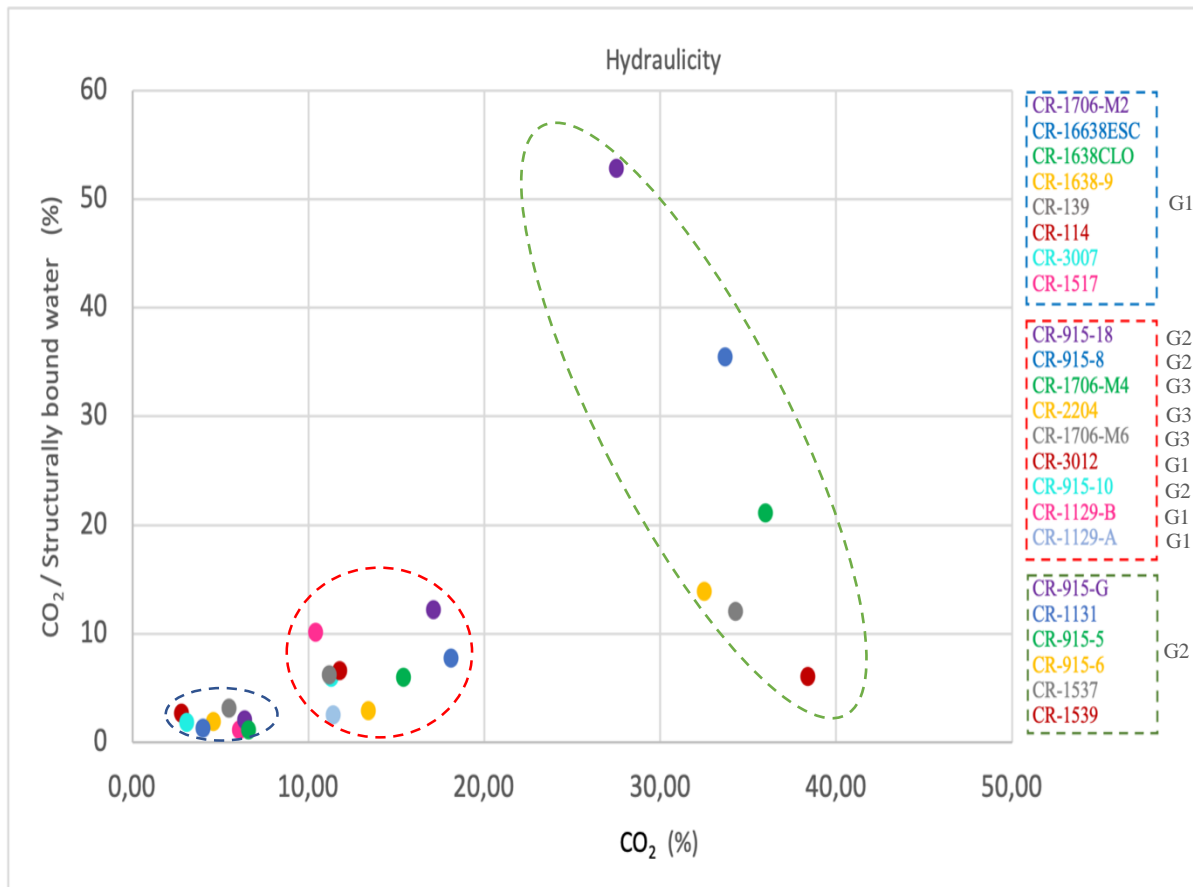


Figure 5.2 CO<sub>2</sub> to structurally bound water ratio in relation to CO<sub>2</sub>%.

It can be concluded that most of the samples related to the with hydraulic characteristics demonstrate very similar characteristics in terms of aggregates composition, particle size distribution, binder to aggregate ratios and hydraulicity, although with some exceptions. The same is applied to the samples with a non-hydraulic character. These confirms the fact that Roman constructors had deep knowledge concerning the construction technologies, selection and combination of raw materials to obtain mortars with specific properties.

As part of the discussion, a comparison between the Roman Cryptoporticus of Lisbon, 1<sup>st</sup> AD AD, and the Roman Cryptoporticus of Mertola V-VI AC. has been performed. The Roman Cryptoporticus of Mertola has been hypothesized by the archaeologists that was an artificial platform which supported an important religious complex from the Byzantine period, which is also the most agreed hypothesis by the archaeologists for the Roman Cryptoporticus of Lisbon.

By means of XRD, the results show that the binding material of the mortars from both sites is essentially calcite and quartz, identified in both groups by XRD, possibly corresponds to the use of a calcitic binder with quartz aggregate component.

By means of chemical analysis of the soluble fraction, the high calcium content, identified in both groups by chemical analysis suggest the use of a calcitic lime as binder, which is the same for both sites.

The granulometric study demonstrated the majority of the aggregates of the sample from both cryptoporticus have dimensions between 0.63 and 2.5 mm (more than 25%) which is categorized as coarse sand by Wentworth. Samples from both Cryptoporticus showed rounded sand, roundness is consistent with river sand for both sites.

Analysis of the mortars by SEM/EDS showed that both samples have a compact microstructure with aggregates well embedded in the matrix.

MultiPoint analyses from the Roman Cryptoporticus of Lisbon and Mertola Cryptoporticus indicated a fairly homogeneous composition throughout the samples analyzed, in which Si is the dominant element present followed by Al, and Mg, K, Ca and Fe found in minor quantities.

TGA curves for the calcium carbonate content have been calculated within different temperature ranges. The thermograms are compatible with the ones of typical roman mortars. with the general absence of important weight loss before the calcite decarbonation at 600-900°C.

## 6 CONCLUSION

The main objective of the study was to bring a clear understanding of the roman mortars regarding their composition to obtain and to provide information about the production technology to characterize the materials in terms of their binder and aggregates as well as the provenance of raw materials used. Such information is necessary to create compatible repair mortars as part of a conservation methodology to implement a sustainable conservation and restoration plan.

To achieve this, a total of 24 samples representing the excavated part from the Roman Cryptoporticus of Lisbon were examined through a multianalytical approach by means of Optical Microscopy (OM, stereo zoom and petrographic microscope), X-ray Diffraction (XRD), Scanning Electron Microscopy coupled with Energy Dispersive X-ray Spectroscopy (SEM-EDS), Thermogravimetric Analysis (TGA-DTG). Acid Attack and Granulometric Analysis were also performed to determine the binder to aggregate ratios of the mortars, as well as the grain size distribution of the insoluble residues. Their chemical and mineralogical compositions were determined for the assessment of the raw materials and their provenance. The manufacturing receipts of the historical mortars and their production techniques were also assessed.

The studied samples were divided into six main groups; i) Quartz rich; ii) with chromatic layer; iii) with ceramic fragments; iv) with carbonate lithics aggregates; v) interventions from 19<sup>th</sup> and 21<sup>st</sup> century, and vi) quartz rich with noticeable presence of lime lumps. The characterization of the materials demonstrates an evident similarity among the samples of the same groups. Furthermore, the groups showed some similarity based on the production technology of the mortars and the binder to aggregate ratio (Tab. 5-1). In terms of aggregate composition all samples shared a uniform mineralogical pattern composing of mainly quartz, feldspars and micas together with Mg and Fe rich minerals like amphiboles in some samples.

Group 1 samples (CR-1638CLO, CR-1638ESC and CR-1638-9), which are floor filler and render mortars collected from the filling of the cloaca structure, which is a narrow vault with 4 holes in its ceiling that had been hypothesized as wells or indented to be wells. It has been used built after the construction of the Cryptoporticus during late roman period and later during the midlevel period it has been clogged with mortars. The mortar revealed a binder matrix composed of Ca, Si, Al, Mg, Na, Cl, S and K. Such composition of the binder provides

hydraulic properties to the mortars without the addition of ceramic fragments or pozzolanic additives. This characteristic feature is directly connected with the expected performance of the mortars since they were prepared to block a water drainage system, which is in a moist environment and needed to have a high level of resistance against humidity.

Group 2 consisted of two samples with a greenish-blue layer (CR-1129-A and 1129-B). The preparatory layer showed the presence of carbonated material as aggregates. For the chromatic layer, by means of SEM the presence of Cu was confirmed. The presence of Cu with Si in the pigmentation indicates that the composition might be made up of copper, which might be Chrysocolla based on the previous literature. As for the preparatory layer, based on the microscopic study and the SEM analysis, it also became clear that it consists mainly of carbonated materials, in addition to the presence of shells. The mortar layer consists mainly of homogeneous, cohesive and sub angular grains of quartz in addition to feldspars, and the binder is a lime binder.

Group 3 (CR-1706M4, CR-1706M6 and CR-2204) is consisting of samples that contain ceramic fragments. Group 3 aggregate's composition demonstrates a uniform mineralogical pattern, presenting predominance of quartz, additionally, to the presence of illite and/or mica (Muscovite or biotite) and amphibole and hematite as trace minerals. The hydraulicity level of this group is calculated as a medium degree. This characteristic feature can be correlated with the expected performance of the mortars since they were prepared to be used as render mortars for walls in different places of the Cryptoporticus that is in naturally in contact with water and needed to have a certain level of resistance against the water.

Group 4 samples (CR-915G, CR-915-5, CR-915-6, CR-915-8, CR-915-10, CR-915-18, CR-1131, CR-1537 and CR-1539) correspond to filler mortars used in floors, except for sample CR-915-G is a filling sample from walls. They demonstrated similar characteristics among each other in terms of binder composition using calcitic lime with some impurities, which suggest the same source of raw materials. Their binder:aggregate ratios could not be determined for most of the samples within this group as they have mainly carbonated lithic aggregates (limestone, dolostone and sandstone) together with lime binder. Accordingly, the results by TGA and acid attack indicated the presence of a high percentage of the soluble component, which reached more than 80% in some sample.

Group 5 of samples correspond to the mortars used for the interventions from 19<sup>th</sup> and 21<sup>st</sup> centuries. Analysis demonstrated the use of calcitic binder for this group of samples. Compared to the rest of the Roman samples, this group shows a higher degree of hydraulicity, similar to

the samples of group 1. Which reflects the understanding and the knowledge of the builders during the 19<sup>th</sup> century. The formation of hydraulic products and recrystallized calcium carbonate processes can explain the good cohesion and mechanical strength of the studied mortars

The mortar of Group 6 (CR-1517-4, CR-1706-M2, CR-3007 and CR-3012), samples collected from 3 different rooms of the same building, consist of a binder that corresponds to calcitic lime. In all samples, the binder is calcitic lime. The presence of lime lumps indicates that the lime was dry-slaked. The samples in this group represented hydraulic properties. The use of the same type of aggregates and binder in the formulation of all the mortars is consistent with the archaeological evidence that these parts were built in the same period.

In all samples, the binder used was calcitic lime. Thin section and polished surface microscopy observations along with XRD analysis showed that two types of natural aggregate sources were used. One type consisting of river sand mainly composed of quartz with smaller amounts of mica, feldspars and amphiboles from the surroundings of Lisbon. The most possible provenance for this type of aggregates corresponds to sand deposits along the Tagus River. The grouping of the mortars according to their aggregate characteristics allowed to correlate the different constructive purposes with the selection of filling material as the distinctive feature.

The archaeometric study carried out on the historical mortars allowed to obtain crucial information regarding provenance and selection of raw materials used for the production of the mortars. Such characterization is necessary to create compatible repair mortars as an important part of the conservation methodology which is planned to be made in the future.

## 7 BIBLIOGRAPHY

---

- Adam, J. P. (2005). *Roman building: materials and techniques*. Routledge.
- Adriano, P., & Santos Silva, A. (2006). Caracterização de argamassas do período romano e árabe da Vila de Mértola. *Portugal, LNEC, Proc. 0204/11/16163, Relatório, 1*, 06-51.
- Almeida, I. M. (1991). Características geotécnicas dos solos de Lisboa. Geologia, Universidade de Lisboa, Lisboa. PHD Thesis.
- Almeida, L. F. D. S. D. (2015). *Caracterização das argamassas da muralha tardo-romana de olisipo* (Doctoral dissertation).
- Andrade, Francisco Martins de., (1859). – Memória à cerca d' uns restos de Thermas Romanas existentes em Lisboa, acompanhada de nove desenhos coloridos tirados escrupulosamente sobre os próprios sítios, com a medição correspondente. (Ms. nos 7299, 7619 e 8468 do *Fundo da Biblioteca Nacional de Lisboa*).
- Artioli, G. (2010). *Scientific methods and cultural heritage: an introduction to the application of materials science to archaeometry and conservation science*. OUP Oxford.
- Artioli, G., Secco, M., & Addis, A. (2019). The Vitruvian legacy: Mortars and binders before and after the Roman world.
- ARTIOLI, G., & OBERTI, R. (2019). Introduction: The role of modern mineralogy in cultural heritage studies.
- Bairrão Oleiro, J. M., & De Alarcão, J. (1973). Le cryptoportique d'Aeminium (Portugal). *Publications de l'École Française de Rome*, 14(1), 349-369.
- Bartos, P., Groot, C., & Hughes, J. (1999, May). International RILEM workshop on historic mortars: Characteristics and Tests. In *Proceedings of the International RILEM Workshop, Paisley, Scotland*.
- Bakolas, A., Biscontin, G., Contardi, V., Franceschi, E., Moropoulou, A., Palazzi, D., & Zendri, E. (1995). Thermoanalytical research on traditional mortars in Venice. *Thermochimica Acta*, 269, 817-828.
- Bakolas, A., Biscontin, G., Moropoulou, A., & Zendri, E. (1998). Characterization of structural byzantine mortars by thermogravimetric analysis. *Thermochimica Acta*, 321(1-2), 151-160.
- Barker, A. J. (2014). *A key for identification of rock-forming minerals in thin section*. CRC Press.
- Berkeley-Cotter, J. C. (1956). “O” Miocénico marinho de Lisboa:(publicação póstuma). Serv. geol. de Portugal.
- Borgwardt, R. H., & Bruce, K. R. (1986). Effect of specific surface area on the reactivity of CaO with SO<sub>2</sub>. *AIChE journal*, 32(2), 239-246.

- Borsoi, G., Silva, A. S., Menezes, P., Candeias, A., & Mirão, J. (2019). Analytical characterization of ancient mortars from the archaeological roman site of Pisões (Beja, Portugal). *Construction and Building Materials*, 204, 597-608.
- Caessa, A., Nozes, C., & Mota, N. (2016). Novas descobertas no criptopórtico romano de Lisboa-Rua da Conceição, 75-77 (primeira fase). *Al madan*, 220-221.
- Callebaut, K. (2000). Characterisation of historical lime mortars in Belgium: implications for restoration mortars. *Unpublished PhD-thesis, KU Leuven*.
- Chauhan, A., & Chauhan, P. (2014). Powder XRD technique and its applications in science and technology. *J Anal Bioanal Tech*, 5(5), 1-5.
- Chen, Y., Huang, B., Huang, M., Lu, Q., & Huang, B. (2018). Sticky rice lime mortar-inspired in situ sustainable design of novel calcium-rich activated carbon monoliths for efficient SO<sub>2</sub> capture. *Journal of Cleaner Production*, 183, 449-457.
- Corti, C., Rampazzi, L., Bugini, R., Sansonetti, A., Biraghi, M., Castelletti, L., ... & Orsenigo, C. (2013). Thermal analysis and archaeological chronology: the ancient mortars of the site of Baradello (Como, Italy). *Thermochimica Acta*, 572, 71-84.
- Dang, T. A., Kamali-Bernard, S., & Prince, W. A. (2013). Design of new blended cement based on marine dredged sediment. *Construction and Building Materials*, 41, 602-611.
- De Alarcão, J., & Etienne, R. (1973). L'architecture des cryptoportiques de Conimbriga (Portugal). *Publications de l'École Française de Rome*, 14(1), 371-405.
- Do Rosário Veiga, M., Aguiar, J., Silva, A. S., & Carvalho, F. (2004). *Conservação e renovação de revestimentos de paredes de edifícios antigos*
- Duarte, I. M. R., Ladeira, F. L., & Gomes, C. F. (2000). Características geológico-geotécnicas do solo residual do granito de Marvão (Portalegre). In *Actas do VII Congresso Nacional de Geotecnia* (Vol. 1, pp. 151-60).
- Elsen, J. (2006). Microscopy of historic mortars—a review. *Cement and concrete research*, 36(8), 1416-1424.
- Elsen, J., Balen, K. V., & Mertens, G. (2012). Hydraulicity in historic lime mortars: a review. *Historic mortars*, 125-139.
- Fabião, C. (1994). O monumento romano da Rua da Prata. *Lisboa Subterrânea. Lisboa: MNA*.
- Földvári, M. (2011). *Handbook of thermogravimetric system of minerals and its use in geological practice* (Vol. 213, pp. 1-180). Budapest: Geological Institute of Hungary.
- Genestar, C., Pons, C., & Más, A. (2006). Analytical characterisation of ancient mortars from the archaeological Roman city of Pollentia (Balearic Islands, Spain). *Analytica Chimica Acta*, 557(1-2), 373-379.

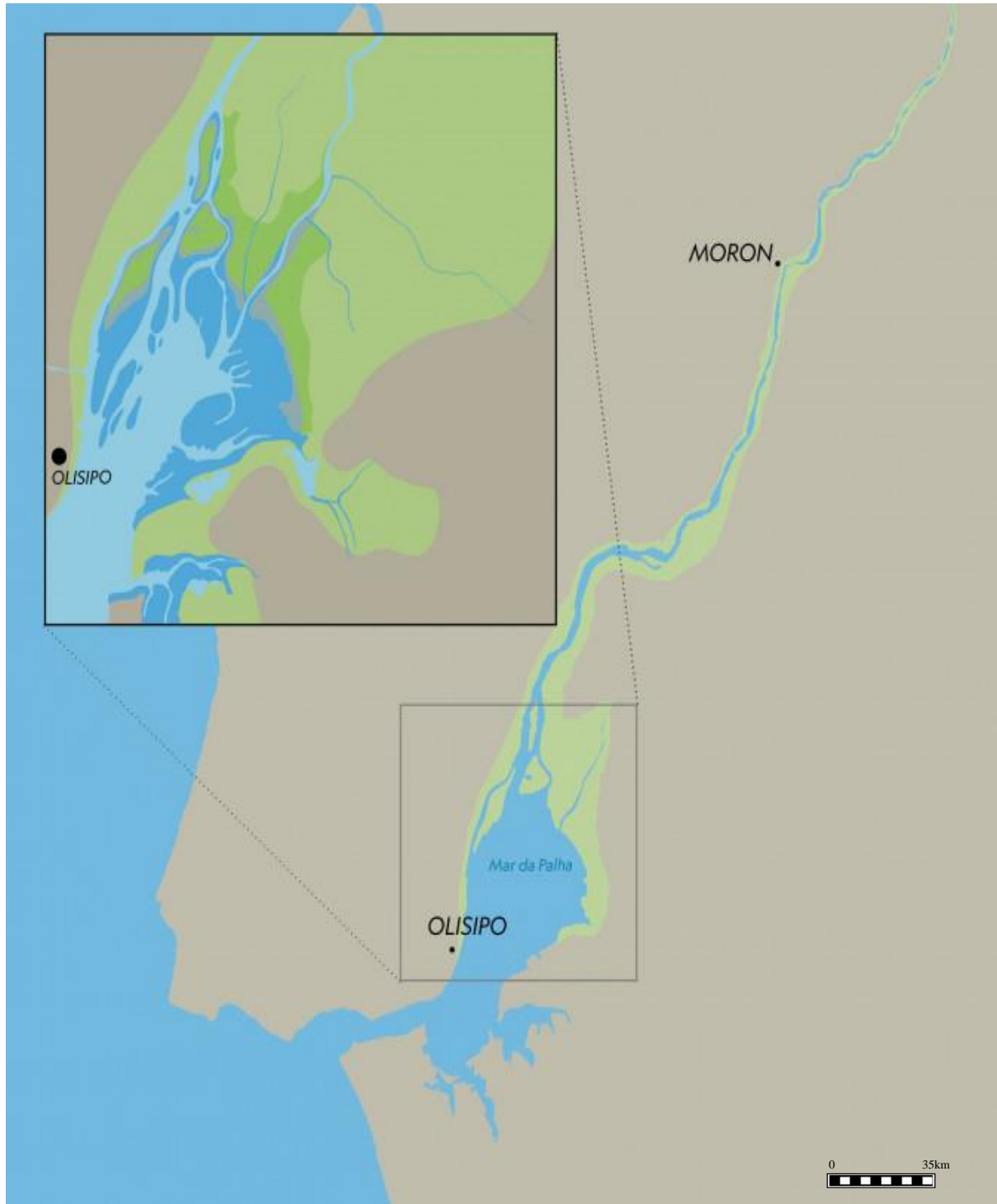
- Gopher, A., Barkai, R., Shimelmitz, R., Khalaily, M., Lemorini, C., Heshkovitz, I., & Stiner, M. (2005). Qesem Cave: Amudian site in central Israel. *Mitekufat Haeven: Journal of the Israel Prehistoric Society/מתקופת האבן*, 69-92.
- Jedrzejewska, H. (1960). Old mortars in Poland: a new method of investigation. *Studies in Conservation*, 5(4), 132-138.
- Jorge-Villar, S. E., & Edwards, H. G. (2021). Green and blue pigments in Roman wall paintings: A challenge for Raman spectroscopy. *Journal of Raman Spectroscopy*, 52(12), 2190-2203.
- Karkanias, P. (2007). Identification of lime plaster in prehistory using petrographic methods: a review and reconsideration of the data on the basis of experimental and case studies. *Geoarchaeology: An international journal*, 22(7), 775-796.
- Lanas, J., Sirera, R., & Alvarez, J. I. (2006). Study of the mechanical behavior of masonry repair lime-based mortars cured and exposed under different conditions. *Cement and Concrete Research*, 36(5), 961-970.
- Lopes, A., & Vieira, H. (2001). Heat fluxes from Landsat images: a contribution to Lisbon urban planning. *Regensburger Geogr. Schriften*, 35, 169-176.
- Margalha, M. G. (2010). *Ligantes aéreos minerais. Processos de extinção e o facto tempo na sua qualidade* (Doctoral dissertation, Tese de doutoramento. Lisboa: Universidade Técnica de Lisboa).
- Margalha, G., Veiga, R., Silva, A. S., & De Brito, J. (2011). Traditional methods of mortar preparation: The hot lime mix method. *Cement and concrete composites*, 33(8), 796-804.
- Moita, I. (1977). As termas romanas da Rua da Prata. *Lisboa: Câmara Municipal de Lisboa*.
- Middendorf, B., Hughes, J. J., Callebaut, K., Baronio, G., & Papayianni, I. (2005). Investigative methods for the characterisation of historic mortars—part 2: chemical characterisation. *Materials and Structures*, 38(8), 771-780.
- Moropoulou, A., Bakolas, A., & Bisbikou, K. (1995). Characterization of ancient, byzantine and later historic mortars by thermal and X-ray diffraction techniques. *thermochimica acta*, 269, 779-795.
- Mota, N., & Martins, P. V. (2018). Criptopórtico Romano de Lisboa: Arqueologia e arquitetura de uma estrutura portuária (um esboço preliminar). *Senna-Martinez, JC; Martins, AC; Caessa, A.; Marques, A*, 78-101.
- Ouhadi, V. R., & Yong, R. N. (2003). The role of clay fractions of marly soils on their post stabilization failure. *Engineering geology*, 70(3-4), 365-375.
- Paama, L., Pitkänen, I., Rönkkömäki, H., & Perämäki, P. (1998). Thermal and infrared spectroscopic characterization of historical mortars. *Thermochimica Acta*, 320(1-2), 127-133.

- Pais, J., Moniz, C., Cabral, J., Cardoso, J., Legoinha, P., Machado, S., ... & Falé, P. (2006). Notícia Explicativa da Carta geológica 1: 50.000, no. 34-D, Lisboa. *Instituto Nacional de Engenharia, Tecnologia e Inovação*.
- Raith, M. M., Raase, P. R., & Reinhardt, J. R. (2011). *Guide to thin section microscopy*. University of Bonn.
- Rato, V. N. D. P. M. (2006). Influência da microestrutura morfológica no comportamento de argamassas.
- Rayment, D. L., & Pettifer, K. (1987). Examination of durable mortar from Hadrian's Wall. *Materials science and technology*, 3(12), 997-1004.
- Ribeiro, J. C. (1994). Breve nota acerca do criptopórtico de Olisipo e da possível localização do «forum corporativo». *Encontro de Arqueologia Urbana. Braga, 1994. Bracara Augusta*, 191-200.
- Rodriguez-Navarro, C., Cazalla, O., Elert, K., & Sebastian, E. (2002). Liesegang pattern development in carbonating traditional lime mortars. *Proceedings of the Royal Society of London. Series A: Mathematical, Physical and Engineering Sciences*, 458(2025), 2261-2273.
- Rodríguez-Navarro, C. (2012). Binders in historical buildings: Traditional lime in conservation. *Semin. SEM*, 9, 91-112. Rome, ICROOM. Mortars, cements and grouts used in the conservation of historic buildings. Symposium, rome, 3-6 nov. 1981. Mortiers, ciments et coulis utilisés dans la conservation des bâtiments historiques. 3-6 nov. 1981.
- Schnabel, L. (2008). Mortar analysis: Part 1: mortar-making materials. *APT bulletin*, 39(1), 1-4.
- Silva, A. D. (1934). As Termas Romanas da Rua da Prata. Lisboa. *In Anais das Bibliotecas, Museus e Arquivo Histórico Municipais. Lisboa*, 13, 19-29.
- Silva, A. S., Ricardo, J. M., Salta, M., Adriano, P., Mirão, J., Candeias, A. E., & Macías, S. (2006). Characterization of Roman mortars from the historical town of Mértola. *Heritage Weathering and Conservation*, 1, 85-90.
- Silva, A. S., Cruz, T., Paiva, M. J., Candeias, A., Adriano, P., Schiavon, N., & Mirão, J. A. P. (2011). Mineralogical and chemical characterization of historical mortars from military fortifications in Lisbon harbour (Portugal). *Environmental Earth Sciences*, 63(7), 1641-1650.
- Stefanidou, M., Anastasiou, E., & Filikas, K. G. (2014). Recycled sand in lime-based mortars. *Waste management*, 34(12), 2595-2602.
- Stefanidou, M., & Papayianni, I. (2005). The role of aggregates on the structure and properties of lime mortars. *Cement and Concrete Composites*, 27(9-10), 914-919.
- Stuart, B. H. (2007). *Analytical techniques in materials conservation*. John Wiley & Sons.
- Vitruvius, M. P. (1960). The ten books on architecture, translated by Morris Hicky Morgan.

Wentworth, C. K. (1922). A scale of grade and class terms for clastic sediments. *The journal of geology*, 30(5), 377

## 8 APPENDICES

Appendix 1 Tagus River estuary with its fertile islets and the area of *Roman Felicitas Iulia Olisipo* CML | DMC | DPC | CAL | Mafalda Paiva 2019.



Appendix 2 The Roman Cryptoporticus of Lisbon (Roman galleries of *Rua da Prata*) (taken by the author in sept. 2022).



Appendix 3 The current situation of the Roman Cryptoporticus of Lisbon with applied drainage system (taken by the author in sept. 2022).



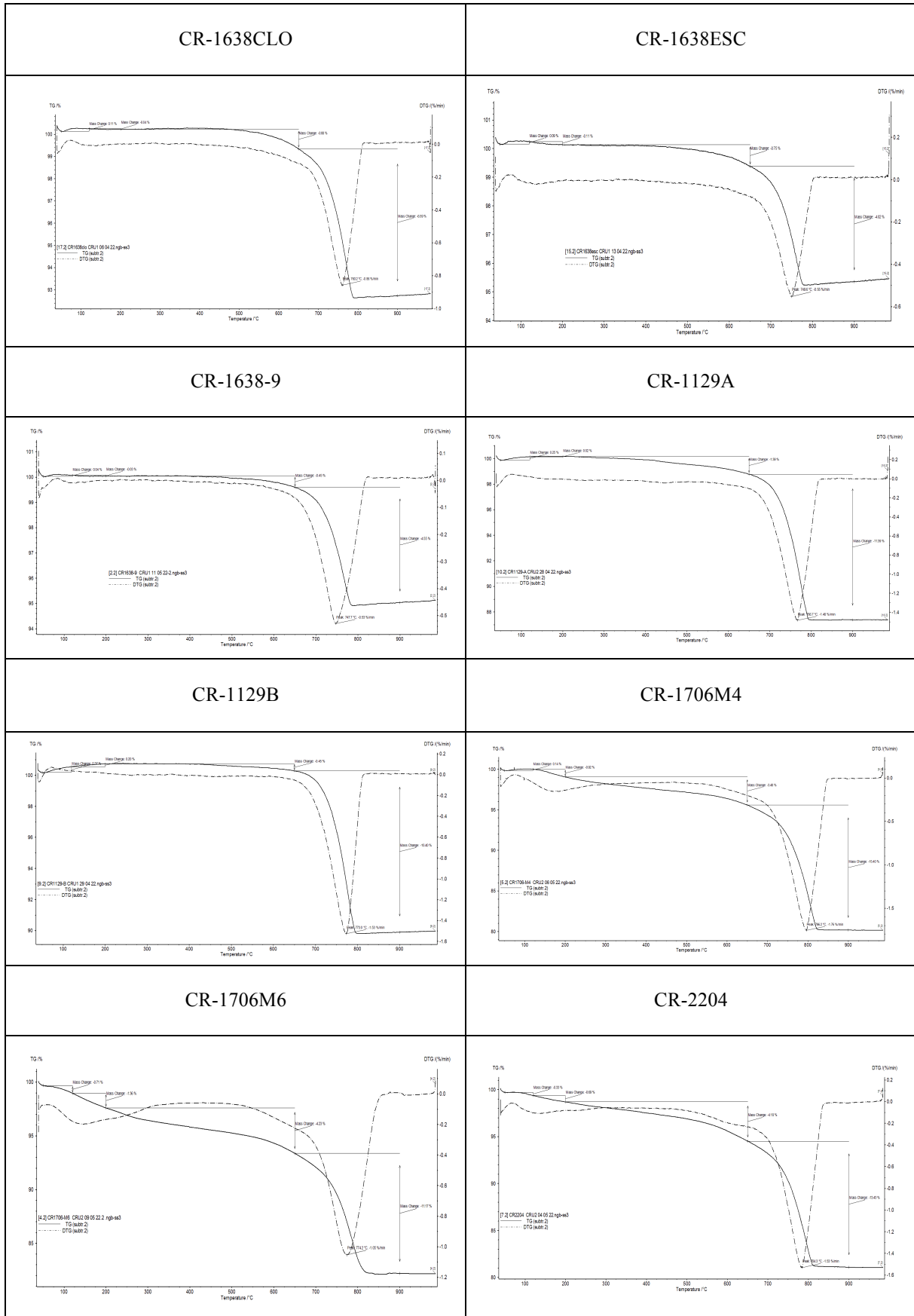
Appendix 4 The current entrance to the galleries, located at the intersection of *Rua da Prata* and *Rua da Conceição*, (Taken by Ehsan RahmtAllah sept.2022)



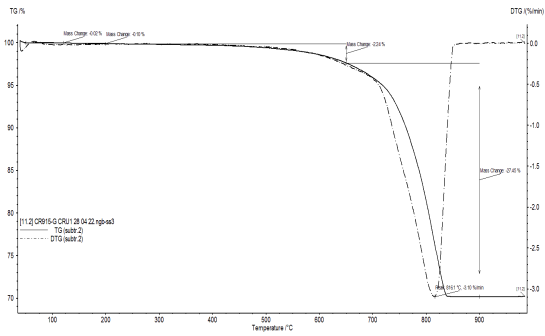
Appendix 5 3D-Model with reconstitution of Cryptoporticus and building that lay above it. CML | DMC | DPC | CAL | Mafalda Paiva 2019



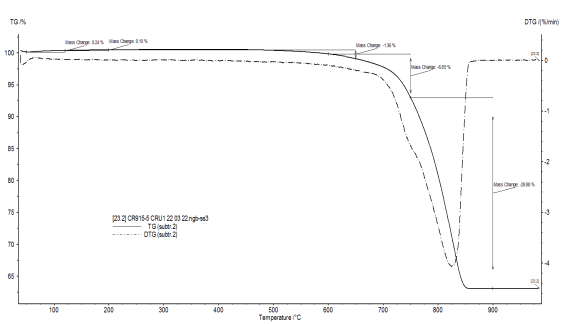
Appendix 6 Thermograms of the powdered samples from the Roman Cryptoporticus of Lisbon.



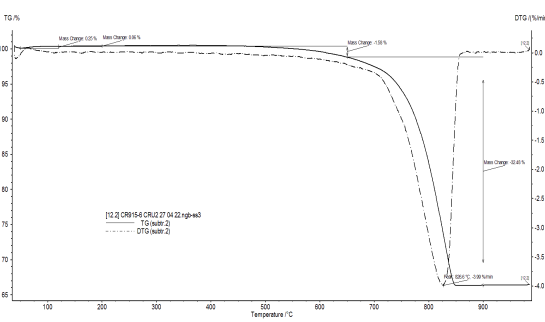
CR-915G



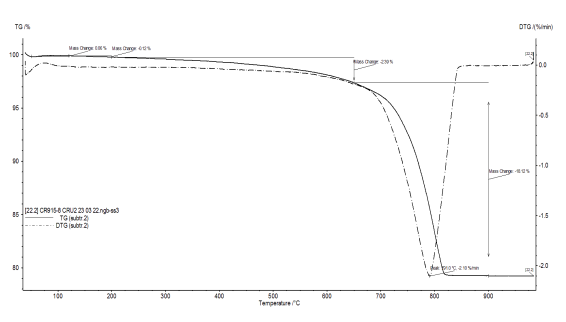
CR-915-5



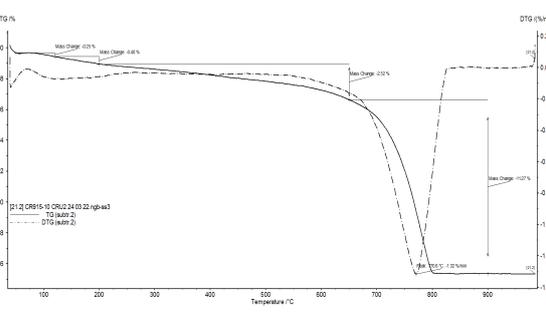
CR-915-6



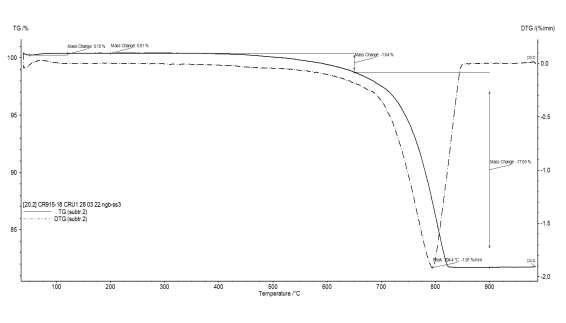
CR-915-8



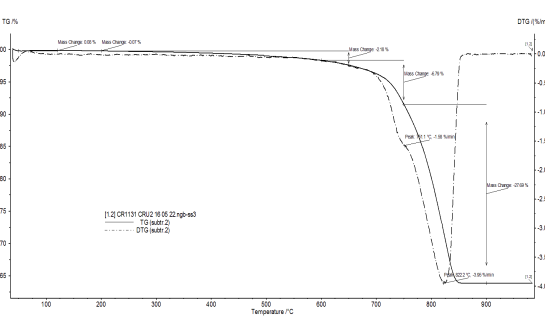
CR-915-10



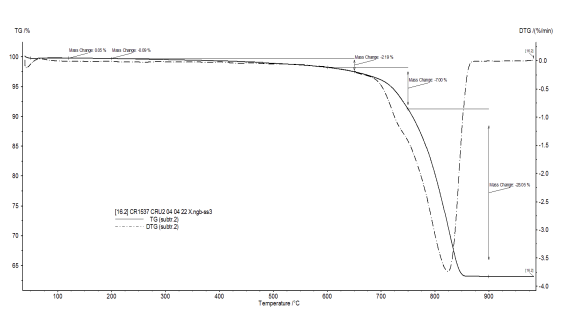
CR-915-18



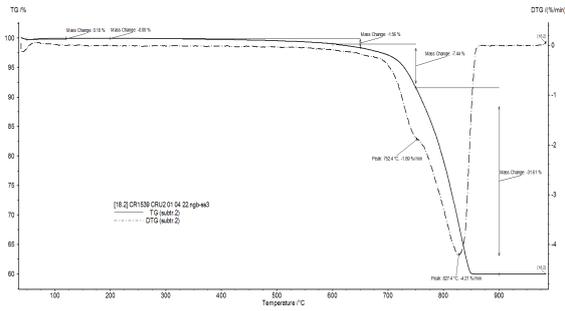
CR-1131



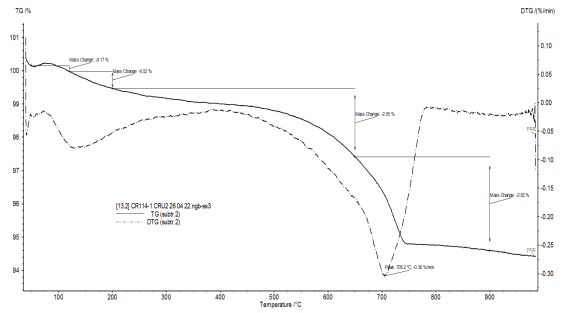
CR-1537



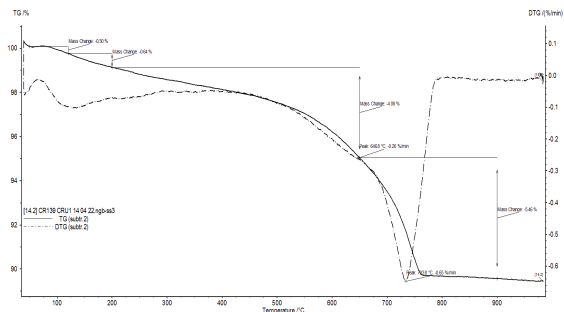
CR-1539



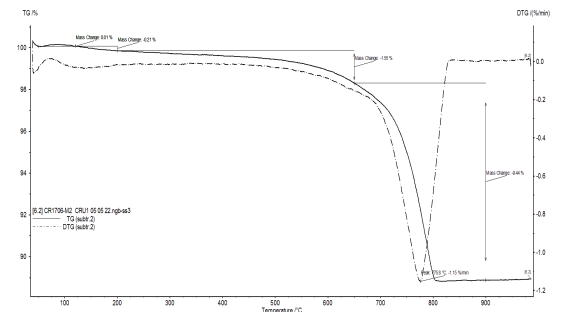
CR-114



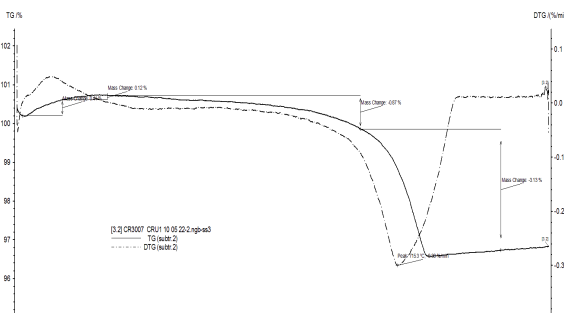
CR-139



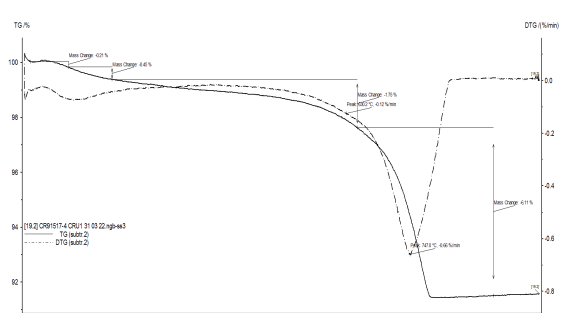
CR-1706M2



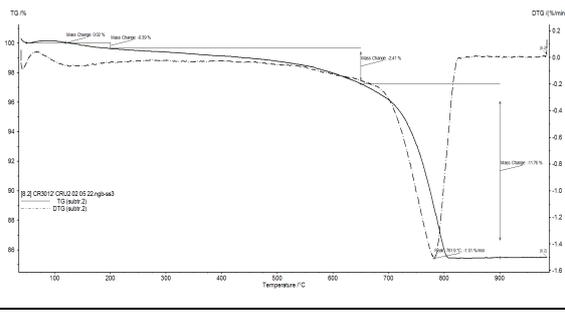
CR-3007



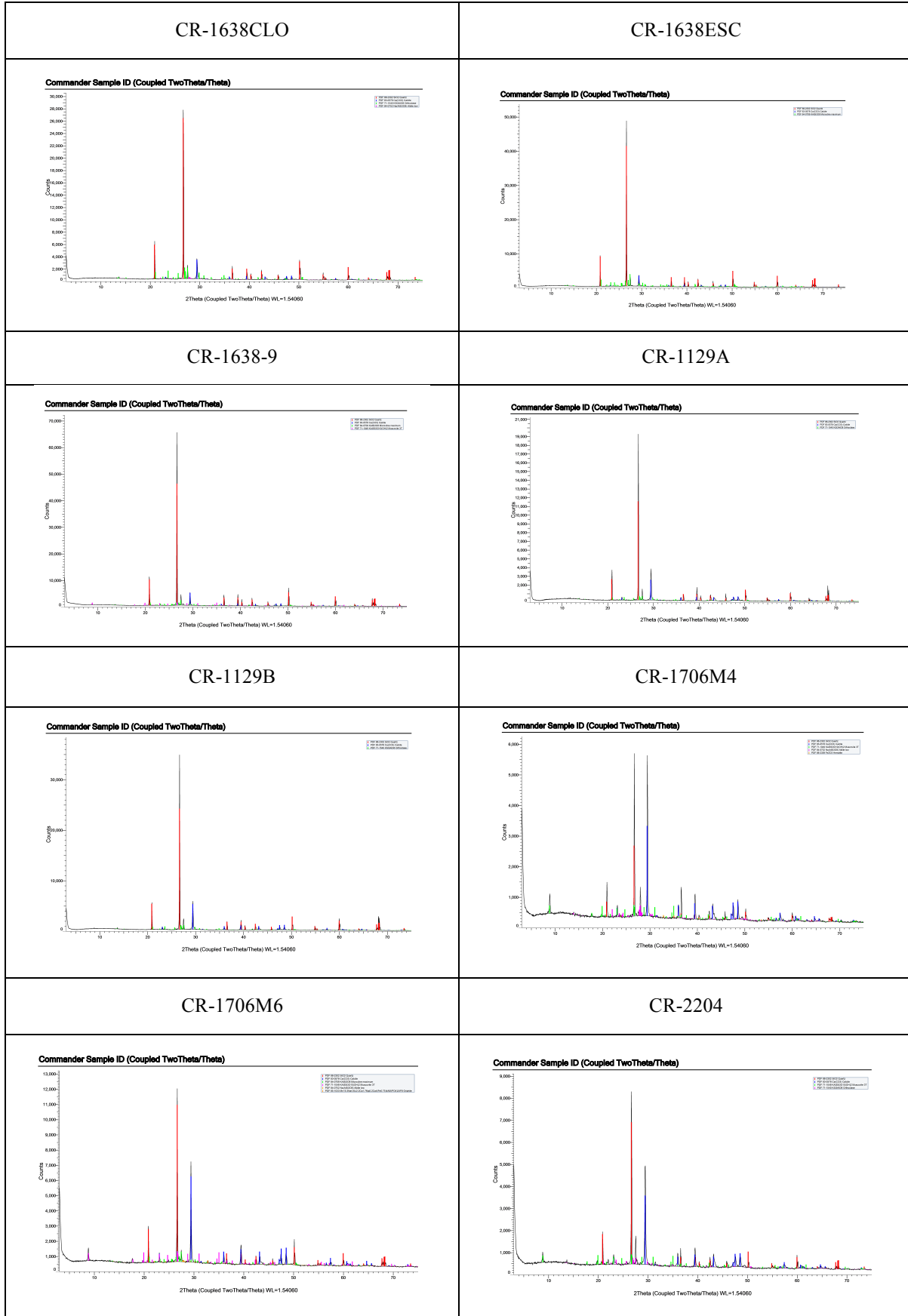
CR-1517-04

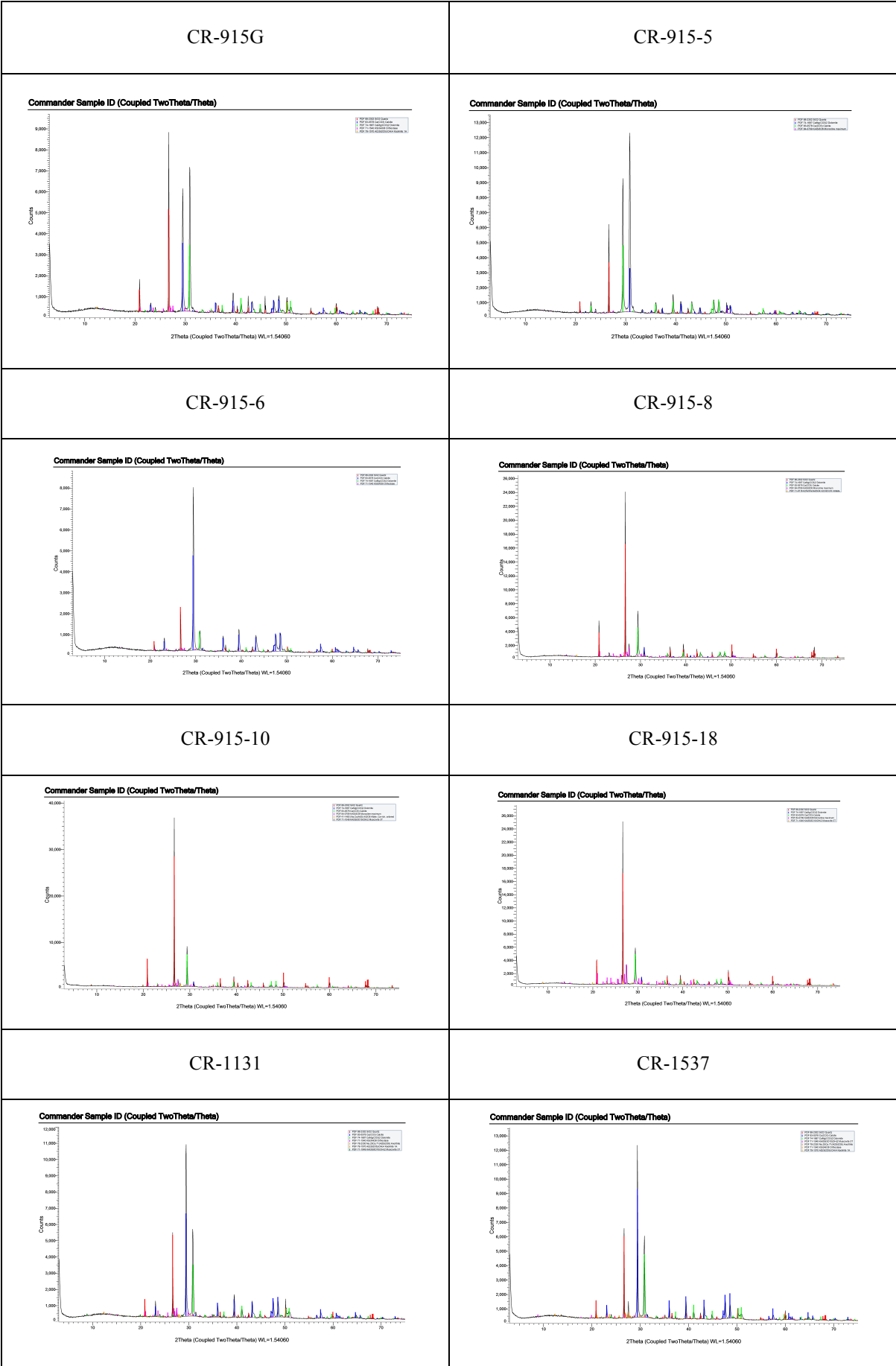


CR-3012



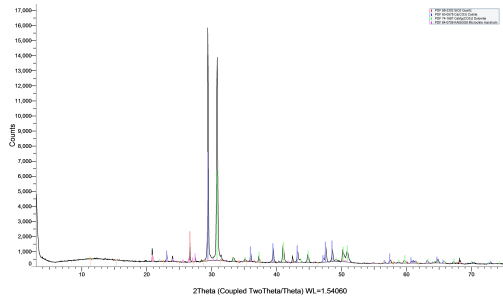
Appendix 7 X-ray diffractograms of the powdered samples from the Roman Cryptoporticus of Lisbon.





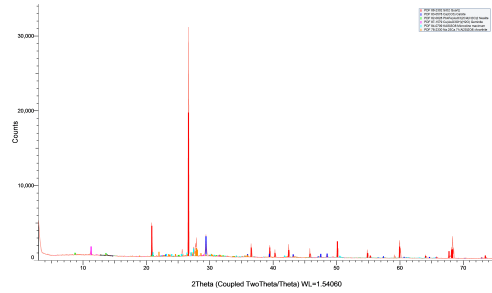
CR-1539

Commander Sample ID (Coupled TwoTheta/Theta)



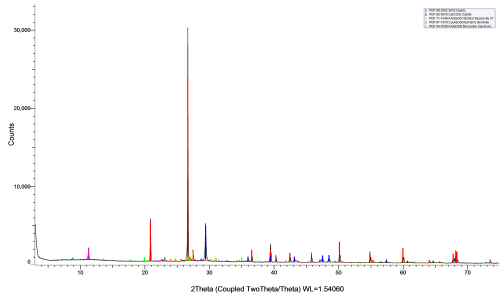
CR-114

Commander Sample ID (Coupled TwoTheta/Theta)



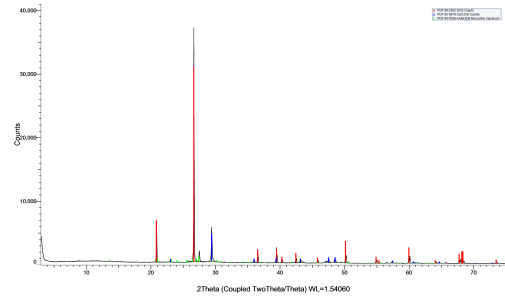
CR-139

Commander Sample ID (Coupled TwoTheta/Theta)



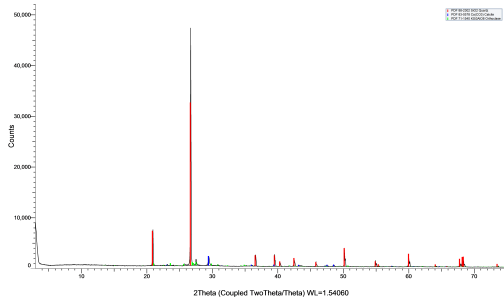
CR-1706M2

Commander Sample ID (Coupled TwoTheta/Theta)



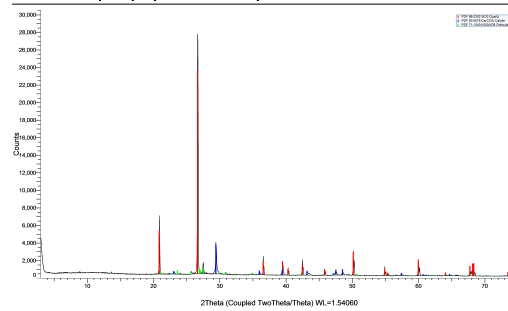
CR-3007

Commander Sample ID (Coupled TwoTheta/Theta)



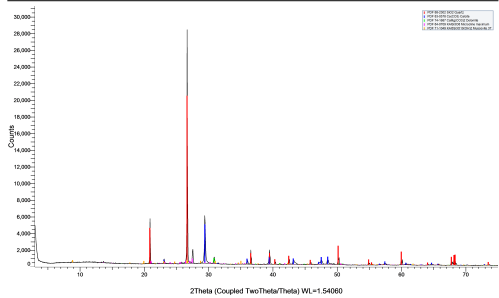
CR-1517-04

Commander Sample ID (Coupled TwoTheta/Theta)



CR-3012

Commander Sample ID (Coupled TwoTheta/Theta)



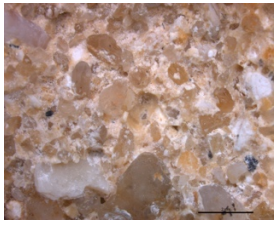
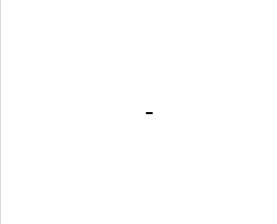
Appendix 8 Results of the acid attack analysis of the samples from the Roman Cryptoporticus of Lisbon.

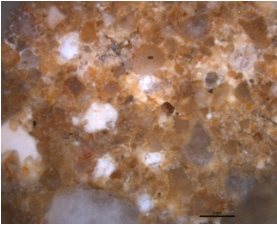
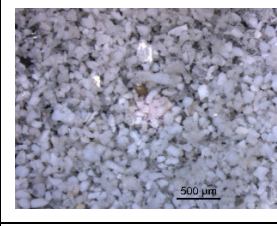
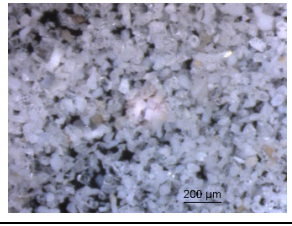
Sample Name		Weight (g)		Fraction (%)	
Sample	Test	Initial	Final	Soluble	Insoluble
CR-915-5	A	8.68	1.17	87	13
CR-915-5	B	9.06	1.09	87	13
CR-1638-ESC	A	10.02	7.91	21	79
CR-1638-ESC	B	10.07	8.00	20	80
CR-1706-M2	A	10.05	6.96	30	70
CR-1706-M2	B	10.05	6.94	31	69
CR-1517-4	A	10.03	7.55	25	76
CR-1517-4	B	10.03	7.55	25	75
CR-915-6	A	9.22	1.12	88	12
CR-915-6	B	9.05	1.15	87	13
CR-139	A	10.55	7.27	31	69
CR-139	B	10.56	7.24	31	69
CR-3012	A	11.00	6.39	42	58
CR-3012	B	11.00	6.8	38	62
CR-1129-A	A	8.41	5.66	33	67
CR-1129-A	B	8.48	5.27	35	65
CR-1129-B	A	10.09	7.01	29	71
CR-1129-B	B	10.9	7.43	27	73
CR-915-G	A	10.26	1.97	81	19
CR-915-G	B	10.37	1.81	82	18
CR-2204	A	10.83	7.76	28	72
CR-2204	B	10.92	7.86	27	73
CR-114-1	A	10.61	7.21	32	68
CR-114-1	B	10.66	7.22	32	68
CR-1539	A	10.02	1.48	85	15
CR-1539	B	10.02	1.43	86	14
CR-1706-M6	A	9.48	5.34	44	56
CR-1706-M6	B	9.50	5.39	43	57
CR-915-8	A	9.02	2.03	77	23
CR-915-8	B	8.80	2.03	77	23
CR-1706-M4	A	10.32	5.73	45	55
CR-1706-M4	B	10.35	5.96	42	58
CR-3007	A	10.7	7.76	27	73
CR-3007	B	10.71	7.89	26	74
CR-1638-9	A	8.00	6.54	18	82
CR-1638-9	B	8.00	6.21	20	80
CR-1537	A	10.32	3.86	63	37
CR-1537	B	10.28	3.8	63	37
CR-915-18	A	10.00	7.65	23	77
CR-915-18	B	10.00	7.5	25	75
CR-1131	A	10.23	1.87	82	18
CR-1131	B	10.10	1.81	82	18
CR-915-10	A	10.03	5.86	41	59
CR-1638-CLO	A	10.00	7.50	25	75

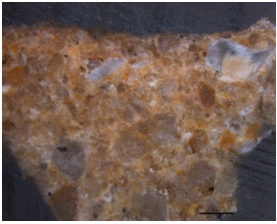
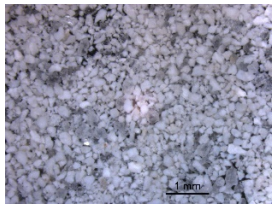
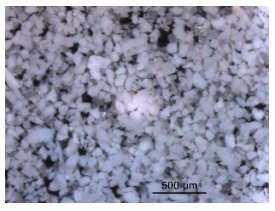
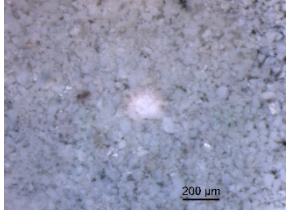
Appendix 9 Results of the granulometric analysis, grain size distribution of the insoluble residue.

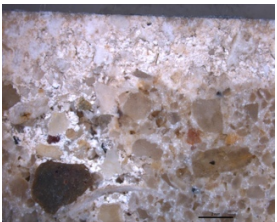
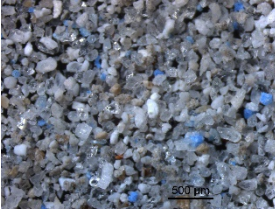
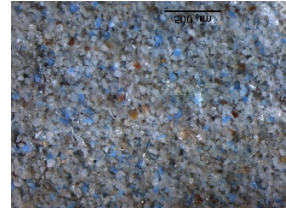
Sample Name		Grain size (g)							
		> 4	4-2	2-1	1-0.5	0.5-0.250	0.250-0.125	0.125-0.063	<0.063
CR-915-5	A	0.00	0.11	0.07	0.11	0.3	0.22	0.22	0.1
CR-915-5	B	0.00	0.09	0.05	0.13	0.14	0.27	0.26	0.1
CR-1638-ESC	A	0.00	0.16	1.19	3.17	2.47	0.54	0.21	0.07
CR-1638-ESC	B	0.00	0.62	1.38	3.17	2.29	0.36	0.13	0.04
CR-1706-M2	A	0.00	0.65	1.69	2.04	1.89	0.4	0.17	0.05
CR-1706-M2	B	0.00	0.65	1.65	2.04	1.88	0.41	0.17	0.04
CR-1517-4	A	0.00	0.71	1.59	2.01	1.66	0.77	0.58	0.19
CR-1517-4	B	0.36	0.6	1.48	2.00	1.64	0.73	0.55	0.16
CR-915-6	A	0.00	0.06	0.13	0.21	0.22	0.21	0.16	0.07
CR-915-6	B	0.00	0.05	0.12	0.18	0.19	0.3	0.17	0.1
CR-139	A	0.00	0.22	1.23	2.52	1.95	0.77	0.38	0.14
CR-139	B	0.00	0.36	1.19	2.51	1.86	0.73	0.38	0.17
CR-3012	A	0.00	1.03	1.44	1.82	1.14	0.48	0.3	0.11
CR-3012	B	0.00	1.16	1.37	1.76	1.21	0.6	0.42	0.2
CR-1129-A	A	0.00	0.00	1.65	2.88	0.67	0.21	0.12	0.07
CR-1129-A	B	0.00	0.13	1.48	2.54	0.71	0.19	0.14	0.07
CR-1129-B	A	0.00	0.16	1.97	3.59	0.75	0.28	0.17	0.06
CR-1129-B	B	0.00	0.03	2.18	3.96	0.79	0.26	0.12	0.06
CR-915-G	A	0.00	0.15	0.22	0.35	0.54	0.37	0.21	0.08
CR-915-G	B	0.00	0.1	0.17	0.43	0.4	0.33	0.27	0.08
CR-2204	A	6.33	0.15	0.18	0.16	0.26	0.31	0.27	0.06
CR-2204	B	6.40	0.28	0.22	0.14	0.18	0.26	0.26	0.06
CR-114-1	A	0.00	0.31	1.29	2.52	2.17	0.51	0.22	0.16
CR-114-1	B	0.13	0.41	1.27	2.52	2.05	0.48	0.2	0.11
CR-1539	A	0.00	0.00	0.04	0.13	0.39	0.38	0.38	0.1
CR-1539	B	0.00	0.00	0.03	0.1	0.21	0.41	0.54	0.12
CR-1706-M6	A	0.61	1.27	0.67	0.53	0.63	0.83	0.6	0.15
CR-1706-M6	B	0.53	1.28	0.78	0.52	0.65	0.74	0.67	0.17
CR-915-8	A	0.00	0.31	0.34	0.5	0.61	0.17	0.07	0.03
CR-915-8	B	0.00	0.26	0.35	0.55	0.6	0.14	0.08	0.03
CR-1706-M4	A	2.08	1.97	0.46	0.41	0.37	0.24	0.14	0.05
CR-1706-M4	B	2.61	1.82	0.46	0.35	0.31	0.2	0.1	0.03
CR-3007	A	0.00	0.8	1.53	2.37	1.88	0.6	0.39	0.16
CR-3007	B	0.00	0.87	1.8	2.44	1.85	0.49	0.31	0.06
CR-1638-9	A	0.00	0.61	0.96	2.26	1.87	0.47	0.14	0.08
CR-1638-9	B	0.00	0.75	0.84	2.04	1.67	0.5	0.29	0.12
CR-1537	A	0.00	0.00	0.00	0.04	1.24	1.49	0.9	0.15
CR-1537	B	0.00	0.00	0.00	0.02	1.53	1.42	0.7	0.12
CR-915-18	A	0.25	1.23	0.00	2.12	1.39	0.51	0.25	0.08
CR-915-18	B	0.32	1.12	2.00	2.02	1.3	0.42	0.19	0.07
CR-1131	A	0.00	0.00	0.04	0.09	0.14	0.46	0.87	0.18
CR-1131	B	0.00	0.00	0.04	0.09	0.13	0.46	0.85	0.17
CR-915-10	A	0.00	0.72	1.18	1.53	1.06	0.69	0.45	0.18
CR-1638-CLO	A	0.00	0.60	1.11	2.60	1.93	0.45	0.51	0.26

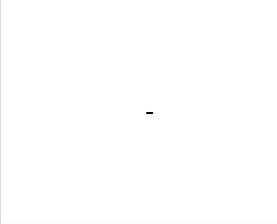
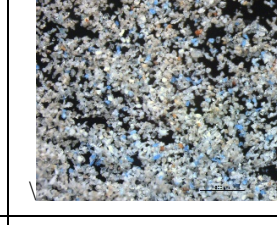
Appendix 10 Insoluble residues obtained after acid attack, observations under Stereozoom microscope

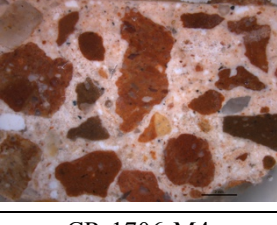
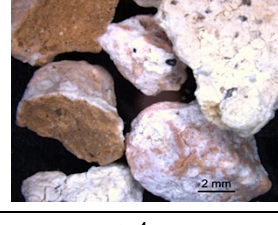
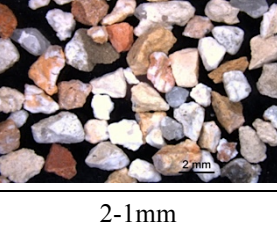
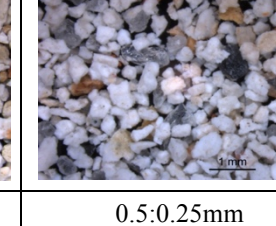
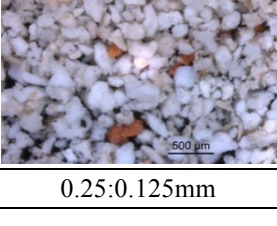
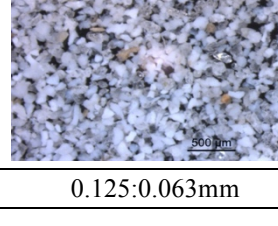
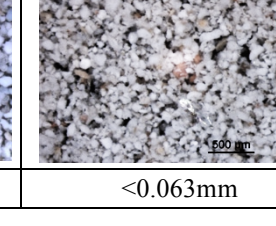
		
CR-1638CLO	>4mm	4-2mm
		
2-1mm	1-0.5mm	0.5:0.25mm
		
0.25:0.125mm	0.125:0.063mm	<0.063mm

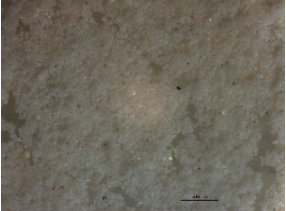
		
CR-1638ESC	>4mm	4-2mm
		
2-1mm	1-0.5mm	0.5:0.25mm
		
0.25:0.125mm	0.125:0.063mm	<0.063mm

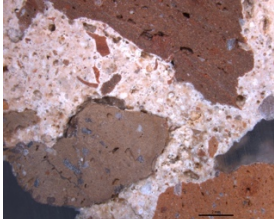
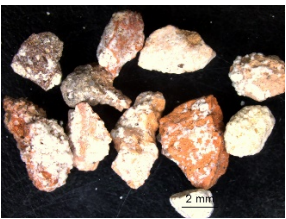
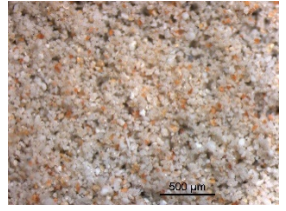
	-	
CR-1638-9	>4mm	4-2mm
		
2-1mm	1-0.5mm	0.5:0.25mm
		
0.25:0.125mm	0.125:0.063mm	<0.063mm

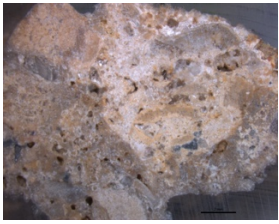
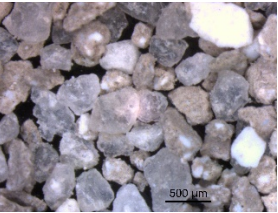
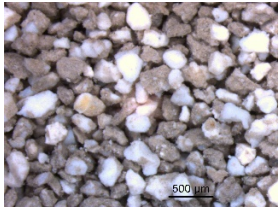
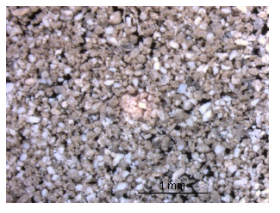
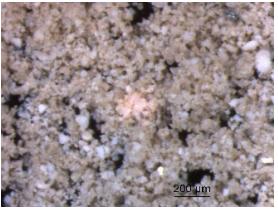
	-	-
CR-1129A	>4mm	4-2mm
		
2-1mm	1-0.5mm	0.5:0.25mm
		
0.25:0.125mm	0.125:0.063mm	<0.063mm

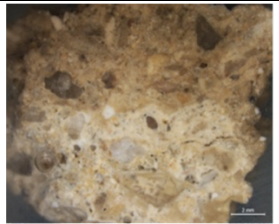
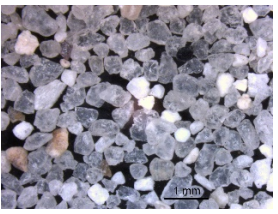
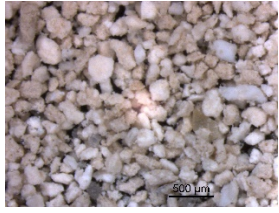
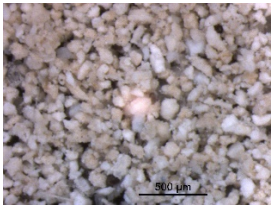
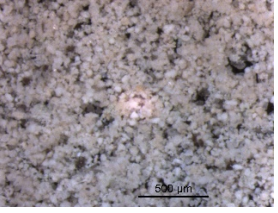
		
CR-1129B	>4mm	4-2mm
		
2-1mm	1-0.5mm	0.5:0.25mm
		
0.25:0.125mm	0.125:0.063mm	<0.063mm

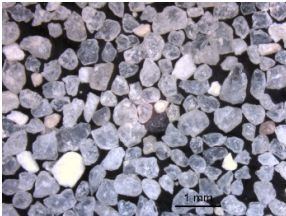
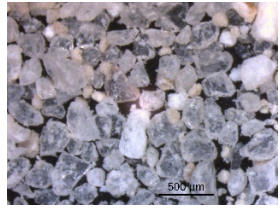
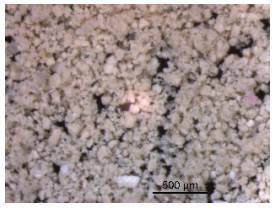
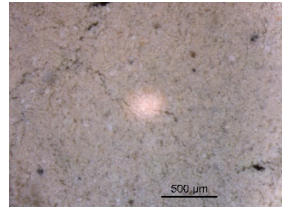
		
CR-1706-M4	>4mm	4-2mm
		
2-1mm	1-0.5mm	0.5:0.25mm
		
0.25:0.125mm	0.125:0.063mm	<0.063mm

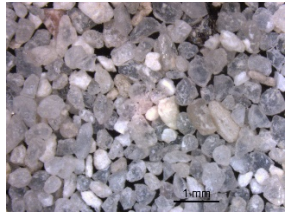
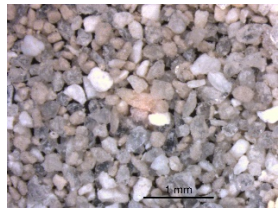
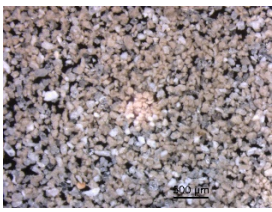
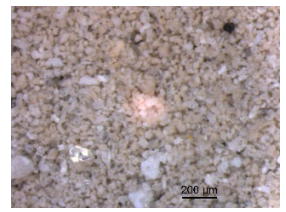
		
CR-1706M6	>4mm	4-2mm
		
2-1mm	1-0.5mm	0.5:0.25mm
		
0.25:0.125mm	0.125:0.063mm	<0.063mm

		
CR-2204	>4mm	4-2mm
		
2-1mm	1-0.5mm	0.5:0.25mm
		
0.25:0.125mm	0.125:0.063mm	<0.063mm

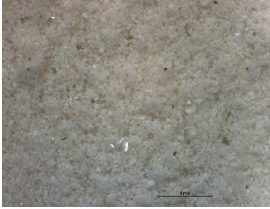
	-	
CR-915G	>4mm	4-2mm
		
2-1mm	1-0.5mm	0.5:0.25mm
		
0.25:0.125mm	0.125:0.063mm	<0.063mm

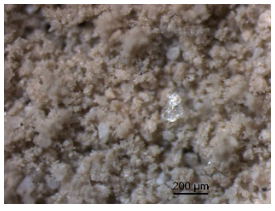
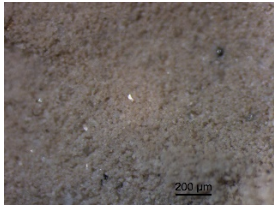
	-	
CR-915-5	>4mm	4-2mm
		
2-1mm	1-0.5mm	0.5:0.25mm
		
0.25:0.125mm	0.125:0.063mm	<0.063mm

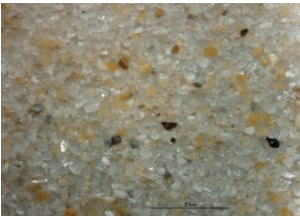
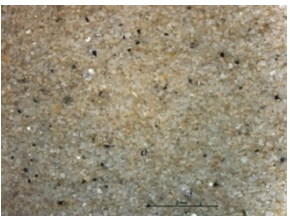
	-	
CR-915-6	>4mm	4-2mm
	-	
2-1mm	1-0.5mm	0.5:0.25mm
		
0.25:0.125mm	0.125:0.063mm	<0.063mm

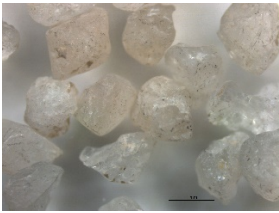
	-	
CR-915-8	>4mm	4-2mm
		
2-1mm	1-0.5mm	0.5:0.25mm
		
0.25:0.125mm	0.125:0.063mm	<0.063mm

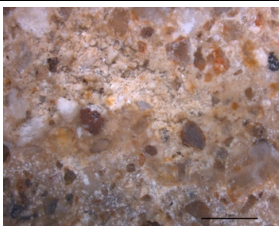
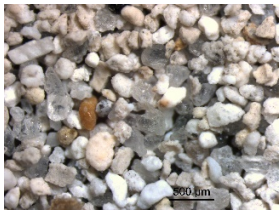
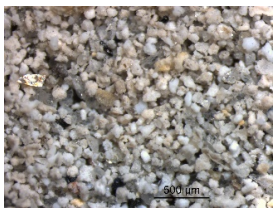
	-	
CR-915-10	>4mm	4-2mm
		
2-1mm	1-0.5mm	0.5:0.25mm
		
0.25:0.125mm	0.125:0.063mm	<0.063mm

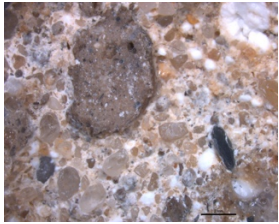
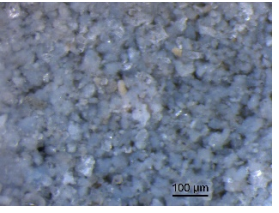
		
CR-915-18	>4mm	4-2mm
		
2-1mm	1-0.5mm	0.5:0.25mm
		
0.25:0.125mm	0.125:0.063mm	<0.063mm

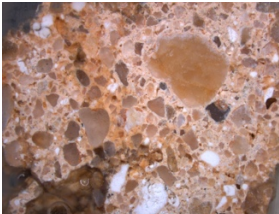
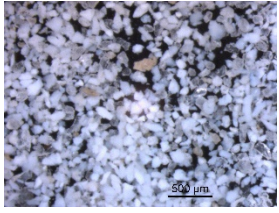
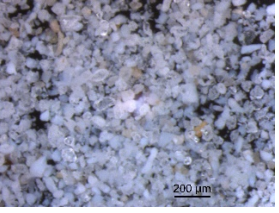
	-	-
CR-1131	>4mm	4-2mm
		
2-1mm	1-0.5mm	0.5:0.25mm
		
0.25:0.125mm	0.125:0.063mm	<0.063mm

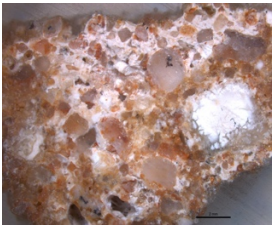
	-	-
CR-1537	>4mm	4-2mm
-		
2-1mm	1-0.5mm	0.5:0.25mm
		
0.25:0.125mm	0.125:0.063mm	<0.063mm

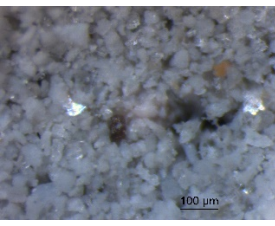
	-	-
CR-1539	>4mm	4-2mm
		
2-1mm	1-0.5mm	0.5:0.25mm
		
0.25:0.125mm	0.125:0.063mm	<0.063mm

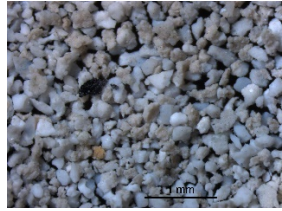
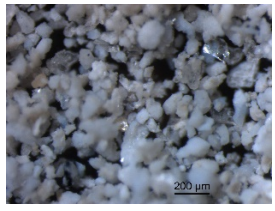
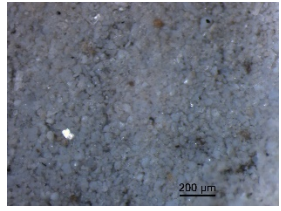
	-	
CR-114	>4mm	4-2mm
		
2-1mm	1-0.5mm	0.5:0.25mm
		-
0.25:0.125mm	0.125:0.063mm	<0.063mm

	-	
CR-139	>4mm	4-2mm
		
2-1mm	1-0.5mm	0.5:0.25mm
		
0.25:0.125mm	0.125:0.063mm	<0.063mm

	-	
CR-1706M2	>4mm	4-2mm
		
2-1mm	1-0.5mm	0.5:0.25mm
		
0.25:0.125mm	0.125:0.063mm	<0.063mm

	-	
CR-1517-04	>4mm	4-2mm
		
2-1mm	1-0.5mm	0.5:0.25mm
		
0.25:0.125mm	0.125:0.063mm	<0.063mm

	-	
CR-3007	>4mm	4-2mm
		
2-1mm	1-0.5mm	0.5:0.25mm
		
0.25:0.125mm	0.125:0.063mm	<0.063mm

		
CR-3012	>4mm	4-2mm
		
2-1mm	1-0.5mm	0.5:0.25mm
		
0.25:0.125mm	0.125:0.063mm	<0.063mm